DIFFERENT APPROACHES FOR ENHANCING DIELECTRIC RESPONSE OF POLYMER AND CERAMIC MATERIALS

Vida Jurečič

Doctoral Dissertation
Jožef Stefan International Postgraduate School
Ljubljana, Slovenia

Supervisor: Prof. Dr. Vid Bobnar, Jožef Stefan Institute, Ljubljana, Slovenia
Co-Supervisor: Dr. Nikola Novak, Jožef Stefan Institute, Ljubljana, Slovenia

Evaluation Board:
Prof. Dr. Hana Uršič Nemevšek, Chair, Jožef Stefan Institute, Ljubljana, Slovenia
Assoc. Prof. Dr. Jurij Koruza, Member, Institute for Chemistry and Technology of Materials, Graz University of Technology, Graz, Austria
Prof. Dr. Juras Banys, Member, Faculty of Physics, Vilnius University, Vilnius, Lithuania

MEDNARODNA PODIPLOMSKA ŠOLA JOŽEFA STEFANA
JOŽEF STEFAN INTERNATIONAL POSTGRADUATE SCHOOL

Vida Jurečič

DIFFERENT APPROACHES FOR ENHANCING DIELECTRIC RESPONSE OF POLYMER AND CERAMIC MATERIALS

Doctoral Dissertation

RAZLIČNI PRISTOPI ZA OJAČENJE DIELEKTRIČNEGA ODZIVA POLIMERNIH IN KERAMIČNIH MATERIALOV

Doktorska disertacija

Supervisor: Prof. Dr. Vid Bobnar

Co-Supervisor: Dr. Nikola Novak

Ljubljana, Slovenia, June 2025

Acknowledgments

I would like to express my sincere gratitude to my supervisor, Dr. Vid Bobnar, and co-supervisor, Dr. Nikola Novak, for their invaluable guidance, encouragement, and constructive feedback throughout my work as a young researcher.

I am also grateful to all the colleagues and technical staff who assisted with the experiments and sample preparation, and whose contributions significantly enhanced the quality of this work.

My heartfelt thanks go to my family, as well as to all my friends and acquaintances, for their unwavering support and understanding.

Finally, I would like to acknowledge the financial support provided by the Slovenian Research and Innovation Agency through the Young Researcher Program.

Abstract

Dielectric materials are essential components of electronic devices and electric power systems. Consequently, the design and development of new materials with enhanced dielectric response remain of great importance. This dissertation examines three different approaches to enhancing the dielectric response: (i) percolative composites, (ii) polymer blending, and (iii) the induction of criticality, each applied to a novel organic or ceramic system.

In light of ecological sustainability, polymer materials, particularly those based on cellulose, have gained significant attention. Due to their low dielectric permittivity, a composite approach is typically used to develop percolative polymers that exhibit a divergent response near the percolation threshold. In this work, titanium carbide MXenes were used as a filler instead of graphene oxide within a cellulose matrix. Measurements across broad frequency and temperature ranges revealed the influence of the preparation method and the type of nanofibrils matrix on the overall dielectric response, as well as the notable effect of absorbed water. A detailed investigation of vacuum-filtered cellulose nanofibrils/MXene composites, which contained the fewest impurities, confirmed that their dielectric response follows the predictions of percolation theory, resulting in a pronounced enhancement of dielectric permittivity with increasing filler content.

Another approach in polymer systems focuses on achieving higher electric energy density by operating at higher electric fields. Dielectric breakdown in polymers is usually initiated by space charges, which are accelerated by an external electric field in the free volume of the system. Therefore, blending appropriate polymers to increase chain packing density and reduce the number of space charges, through strong electrostatic interactions between oppositely charged polymer chains, is expected to enhance dielectric breakdown strength. Accordingly, poly(ether imide)/polyimide blends exhibited approximately 2.5 times higher dielectric breakdown strength than the pristine polymers, contained fewer space charges, and absorbed less water due to higher chain packing density.

Despite containing environmentally hazardous lead, lead-based ceramics remain dominant due to their superior functional properties. A physical approach to induce the maximum dielectric response at a critical end point has produced exceptional functional properties in ferroelectric and relaxor systems. In this work, the existence of two critical end points is shown for the first time in antiferroelectric ceramics using the model system $Pb_{0.99}Nb_{0.02}[(Zr_{0.57}Sn_{0.43})_{0.92}Ti_{0.08}]_{0.98}O_3$. Moreover, enhanced energy storage density and dielectric tunability were observed near these critical end points. To determine the origin of the enhanced dielectric tunability (approximately 375 %) at the temperature of the field-induced triple point, minimization of domain size was proposed as the responsible mechanism and confirmed by Rayleigh measurements and piezoresponse force microscopy.

The results obtained in these novel systems provide new insights into the correlation between structural evolution and property changes in materials developed via different approaches, which is important both fundamentally and practically for developing new materials for advanced dielectric applications.

Povzetek

Dielektrični materiali so ključni sestavni deli elektronskih naprav in elektroenergetskih sistemov, zato sta načrtovanje in razvoj novih materialov z ojačenim dielektričnim odzivom še vedno izjemno pomembna. V tej disertaciji so preučeni trije različni pristopi za ojačenje dielektričnega odziva: (i) perkolativni kompoziti, (ii) mešanje polimerov in (iii) induciranje kritičnosti, pri čemer je vsak pristop izveden na novem organskem ali keramičnem sistemu.

Z ozirom na ekološko trajnost so polimerni materiali, še posebej tisti, ki temeljijo na celulozi, v zadnjem času pridobili veliko pozornosti. Zaradi nizke dielektrične konstante celuloznih polimerov je za doseganje visokih dielektričnih odzivov pogosto uporabljen kompozitni pristop, saj v bližini perkolacijskega praga dielektrični odziv divergira. V tej raziskavi so namesto grafenovega oksida uporabljeni MXeni iz titanovega karbida. Dielektrične meritve, ki so bile izvedene v širokem frekvenčnem in temperaturnem razponu, so pokazale, da način priprave ter izbira vrste celuloznih nanovlaken in absorbirana voda pomembno vplivajo na celoten dielektrični odziv. Podrobna preiskava vakuumsko filtriranih kompozitov iz celuloznih nanovlaken in MXenov, ki so vsebovali najmanj nečistoč, je potrdila, da njihov dielektrični odziv sledi perkolacijski teoriji, kar se kaže v izrazitem naraščanju dielektrične konstante z večanjem vsebnosti polnila.

Drugi pristop na področju polimernih sistemov je usmerjen v zvišanje gostote električne energije z delovanjem pri višjih električnih poljih. Dielektrični preboj v polimerih običajno sprožijo prosti naboji, ki jih zunanje električno polje pospeši v praznem prostoru v materialu. Z mešanjem dveh polimerov je preko močne elektrostatske interakcije med nasprotno nabitimi verigami mogoče povečati gostoto urejenih verig in zmanjšati število prostih nabojev ter posledično povečati dielektrično prebojno trdnost. Zmesi polieterskega imida (PEI) in poliimida (PI) so, v skladu z navedenim, pokazale približno 2,5-krat višjo dielektrično prebojno trdnost v primerjavi z izvirnima polimeroma, vsebovale manj prostih nabojev in absorbirale manj vode zaradi gostejše ureditve verig.

Kljub okolju škodljivi sestavi keramika na osnovi svinca še vedno prevladuje zaradi svojih izjemnih funkcionalnih lastnosti. Fizikalni pristop, ki omogoča dosego največjega dielektričnega odziva v kritični končni točki, je v feroelektričnih in relaksorskih sistemih privedel do izjemnih funkcionalnih lastnosti. V tej disertaciji je prvič prikazan obstoj dveh kritičnih končnih točk v antiferoelektrični keramiki z uporabo modelnega sistema $Pb_{0.99}Nb_{0.02}[(Zr_{0.57}Sn_{0.43})_{0.92}Ti_{0.08}]_{0.98}O_3$. V bližini teh točk sta bili opaženi izboljšana gostota shranjene energije in večja dielektrična nastavljivost. Da bi pojasnili izvor povečane dielektrične nastavljivosti (približno 375 %) pri temperaturi trojne točke, inducirane z električnim poljem, je bilo kot glavni mehanizem predlagano drobljenje domen, kar so potrdile Rayleighove meritve in slikanje s piezoelektričnim modulom na mikroskopu na atomsko silo.

Dobljeni rezultati v teh sistemih nudijo nov vpogled v korelacijo med strukturno evolucijo materialov, razvitih z različnimi pristopi, in njihovimi lastnostmi, kar je ključno za razvoj novih materialov za napredne dielektrične aplikacije tako na temeljni kot praktični ravni.

Contents

List of Figures

Abbreviations

AC	... alternating current
AFE	... antiferroelectric
AFE_O	... orthorhombic antiferroelectric structure
AFE_T	... tetragonal antiferroelectric structure
CNF	... cellulose nanofibrils
CP	... critical end point
cPANI	... conductive polyaniline
CTFE	... chlorotrifluoroethylene
DC	... direct current
FE	... ferroelectric
KNN	... potassium sodium niobate
MPB	... morphotropic phase boundary
MXene	... titanium carbide-based system $Ti_3C_2T_x$
P(VDF-TrFE)	... poly(vinylidene fluoride-trifluoroethylene)
PE	... paraelectric
PEI	... poly(ether imide)
PI	... polyimide
PLZST	... (Pb,La)(Zr,Sn,Ti)O_3
PLZT	... (Pb,La)(Zr,Ti)O_3
PMN	... lead magnesium niobate
PNZST	... (Pb,Nb)(Zr,Sn,Ti)O_3; $Pb_{0.99}Nb_{0.02}[(Zr_{0.57}Sn_{0.43})_{0.92}Ti_{0.08}]_{0.98}O_3$
PT	... lead titanate
PVDF	... poly(vinylidene fluoride)
PZT	... lead zirconate titanate
SEM	... scanning electron microscopy
TCNF	... (2,2,6,6-Tetramethylpiperidin-1-yl)oxy oxidized cellulose nanofibrils
TEMPO	... (2,2,6,6-Tetramethylpiperidin-1-yl)oxyl
XRD	... X-ray diffraction

Symbols

α	...	irreversible Rayleigh coefficient
α_{max}		maximum irreversible Rayleigh coefficient
ΔE	...	switching hysteresis
ΔT_{sample}	...	sample temperature change
ε_0	...	permittivity of free space
ε^*	...	complex linear dielectric constant
ε'	...	real part of the complex dielectric constant, i.e., dielectric permittivity
ε'_3	...	real part of the third harmonic of the dielectric permittivity
ε'_{max}	...	maximum dielectric permittivity
ε'_{norm}	...	normalized dielectric permittivity
ε'_{int}	...	intrinsic (reversible) Rayleigh coefficient
ε''	...	imaginary part of the complex dielectric constant
η	...	dielectric tunability
ν	...	frequency
σ	...	static effective electrical conductivity
σ'	...	real part of the electrical conductivity, i.e., electrical conductivity
σ_{diel}	...	conductivity of the dielectric phase
σ_{metal}	...	conductivity of the metallic phase
ω	...	angular frequency
C	...	capacitance
d	...	sample thickness
D	...	domain size
E	...	electric field
E_0	...	amplitude of the AC electric field
E_{AFE-FE}	...	critical electric field for the AFE–FE phase transition
E_b	...	dielectric breakdown strength
E_{CP}	...	electric field of the critical end point
E_{CP}^{AFE-PE}	...	electric field of the AFE–PE critical end point
E_{CP}^{FE-AFE}	...	electric field of the FE–AFE critical end point
E_{FE-AFE}	...	critical electric field for the FE–AFE phase transition
F	...	free energy density
G	...	electrical conductance
G_{aniso}	...	anisotropic free energy
I	...	electrical current
p	...	volume fraction of metallic regions
p_c	...	percolation threshold
P	...	polarization
P_{max}	...	maximum polarization
P_r	...	remanent polarization
P_S	...	spontaneous polarization

P_{slope}	...	slope of the polarization–electric field curve
R	...	electrical resistance
S	...	electrode area
t	...	time
$\tan\delta$	...	dielectric losses
T	...	temperature
T_C	...	Curie temperature
T_{CP}	...	temperature of the critical end point
$T_{CP}^{AFE–PE}$	...	temperature of the AFE–PE critical end point
$T_{CP}^{FE–AFE}$	...	temperature of the FE–AFE critical end point
T_{TR}	...	temperature of the triple point
U	...	voltage
U_0	...	activation energy; amplitude of the probing AC signal
U_e	...	electric energy density
V_{bd}	...	breakdown voltage
W_{rec}	...	recoverable energy storage density

Chapter 1

Introduction

Dielectric materials, which are used to control and store charges and electric energy, play a key role in modern electronics and electric power systems, making the development of high dielectric permittivity and high electric energy density materials one of the major scientific and technological issues [1–3]. The modern electronic industry desires materials with high dielectric permittivity for the advancement of energy storage devices, flexible electronics, embedded capacitors, actuators, and sensors [4–7].

Due to their lightweight, flexibility, low cost, and ease of processing, polymer-based composites have attracted more attention over the past decades than inorganic materials, despite their low dielectric permittivity. Consequently, novel polymer-based systems with an enhanced dielectric response have been successfully developed by considering basic physical and chemical phenomena. One such example is the composite approach, in which conductive particles are dispersed within a dielectric matrix [6,8]. This approach effectively increases dielectric permittivity due to a large Maxwell–Wagner polarization but simultaneously also boosts dielectric losses. An alternative approach to attain high electric energy density is operation under higher electric fields. This can be achieved by blending appropriately matched polymers, which reduces free volume and structural disorder in the blend system, thereby enhancing the dielectric breakdown strength [9–13].

In recent years, significant effort has been dedicated to designing green electronics. As a countermeasure to the growing problem of electronic waste, a variety of environment-friendly, bio-degradable, and low-cost electronic products have been developed using natural materials [14–16]. Biopolymers such as cellulose have been proposed and researched as promising base materials for flexible electronics [17,18]. One notable example is a percolative biopolymer made by incorporating functionalized graphene oxide into a cellulose-based matrix [19], in which the dielectric permittivity increased by one order of magnitude even at low graphene concentrations. Due to graphene's good electrical properties and high aspect ratio, a lot of effort has been made to further enhance the dielectric properties of graphene-filled composites [18–26]. However, the lack of a large-scale and cost-effective method for synthesizing graphene-based systems limits their application in high-performance electronics [26].

As an alternative to graphene oxide, novel 2D transition metal carbides, nitrides, and carbon nitrides (MXenes) are proposed as a filler in a cellulose-based matrix. These systems, generally represented by the formula $M_{n+1}X_nT_x$ (where M is an early transition metal, X is C and/or N, T represents surface termination unit such as hydroxyl, oxygen, or fluorine, and n=1–3), have attracted much attention due to their outstanding electrochemical properties, hydrophilicity, and metallic conductivity [27]. In particular, $Ti_3C_2T_x$ (the most commonly studied MXene) exhibits even higher electrical conductivity

than solution-processed graphene [28]. Thus, a strong increase in the dielectric response due to a large Maxwell–Wagner interfacial polarization is expected.

The recent focus has also been on keeping dielectric losses as low as possible and enhancing dielectric breakdown strength, both of which are required for large-scale energy storage in high-efficiency power capacitors [10–12,16,21,29,30]. Phenyl groups are fundamental chain components of many high-temperature polymers, and depending on the polymer's molecular structure, delocalized electrons in these groups may exhibit a partially positive or negative charge. Both poly(ether imide) and polyimide are high-temperature polymers with similar dielectric permittivity and contain oppositely charged phenyl groups. Therefore, blending these two polymers is not expected to increase dielectric permittivity or losses. Instead, attractive electrostatic forces between different polymer chains may increase chain packing density and reduce the number of weak points and accumulated space charges. These charges in weak points gain higher energies when accelerated by an applied electric field and, consequently, initiate breakdown at lower electric fields [12]. Zhang et al. [12] demonstrated that poly(ether imide)/polyimide blends can withstand significantly higher electric fields than pristine polyetherimide and polyimide. However, the origin of this enhanced dielectric breakdown strength has not yet been investigated.

Antiferroelectric materials are known to exhibit their highest dielectric response during a phase transition, which is always accompanied by a structural transformation triggered by an applied electric field, temperature variation, or hydrostatic pressure. Due to their extremely high dielectric permittivity, $PbZrO_3$-based ceramics continue to be widely used and studied, despite containing toxic lead. $PbZrO_3$-based antiferroelectrics are a group of important electronic materials with promising applications in high-energy storage capacitors, micro-actuators, pyroelectric security sensors, cooling devices, pulsed power generators, and more. Their remarkable functional properties are primarily attributed to the electric field-induced phase-switching behavior between the antiferroelectric and ferroelectric states [31,32]. To reduce the critical electric field required for the phase transition and to optimize material properties, $PbZrO_3$-based antiferroelectrics are often chemically modified with dopants such as Sn, Ti, Nb, or La [33–38]. A representative composition, $Pb_{0.99}Nb_{0.02}[(Zr_{0.57}Sn_{0.43})_{0.92}Ti_{0.08}]_{0.98}O_3$ (PNZST), demonstrates a reversible antiferroelectric-to-ferroelectric phase transition at a sustainable electric field [37]. Despite the intimate relation between functional properties and electric field-induced phase transitions, a detailed investigation of the relation between the electric field and the nature of the phase transition has not been explored yet. In particular, the existence of a critical point within the antiferroelectric system and its relation to functional properties such as polarization, dielectric tunability, and energy storage have yet to be thoroughly investigated.

In this work, three different approaches for achieving an enhanced dielectric response are demonstrated, each on an exemplary system. First, the composite approach is demonstrated using flexible, eco-friendly composites composed of cellulose nanofibrils and conductive $Ti_3C_2T_x$ filler. Next, the blending of polymers with oppositely charged phenyl groups as a means of attaining high electric energy density without increasing dielectric losses is shown using poly(ether imide)/polyimide blends. Finally, for the first time in an antiferroelectric system, a physical approach to induce an enhanced response in the proximity of a critical end point by manipulating experimental conditions is demonstrated in PNZST ceramics. A thorough dielectric investigation of these three systems provides deeper insight into structure-property evolution, which is important for both the fundamental and practical aspects of developing novel materials with enhanced dielectric response.

Chapter 2

Materials with Enhanced Dielectric Response

The development of materials with high dielectric permittivity has become one of the major scientific and technological challenges, as the demand for compact and low-cost systems designed to control and store electrical charges has increased substantially. Such materials are highly desirable not only as capacitor dielectrics, but also for a broad range of electromechanical applications, such as actuators, sonars, and high-frequency transducers. The input electric energy that can be converted into strain energy in electroactive materials is directly proportional to the real part of the complex dielectric constant (dielectric permittivity, ε'): $U_e \propto \varepsilon' {E_b}^2$. Therefore, by increasing the dielectric permittivity, the desired strain can be induced under a significantly reduced electric field. A prominent class of materials that exhibit high permittivity is ferroelectrics, which possess spontaneous polarization and strong electromechanical coupling. While some ferroelectric materials occur naturally, many technologically relevant ones, such as lead zirconate titanate, are tailored through compositional tuning and microstructural optimization to enhance their functional properties.

Parts of this chapter were originally published in V. Jurečič *et al., APL Mater.* (2024) 12(11): 111102, and in V. Jurečič *et al.*, *Macromolecules* (2023) 56(3): 1097–1104.

2.1 Ferroelectric Materials

Ferroelectrics represent a distinct subgroup of dielectric materials that exhibit spontaneous polarization in the absence of an applied electric field. The most common crystal structure found in ferroelectrics is the distorted perovskite, with a general formula ABO_3, where the valence of A-site cations ranges from +1 to +3, and that of B-site cations from +3 to +6. A typical perovskite structure is illustrated in Figure 1. Spontaneous polarization arises from the displacement of ions within a unit cell exhibiting tetragonal symmetry. When positive or negative ions are displaced from their symmetric positions, each unit cell acquires a dipole moment. The macroscopic spontaneous polarization results from the collective alignment of these adjacent dipole moments in the same direction. Regions within ferroelectric materials where spontaneous polarization is uniformly oriented are called ferroelectric domains, while the interfaces separating two domains are referred to as domain walls [39,40]. By applying an external electric field, the direction of polarization can be reversed: the domains begin to reorient in the direction of the applied field, leading to

polarization saturation and a characteristic hysteresis loop during electric field cycling, as depicted in Figure 2a.

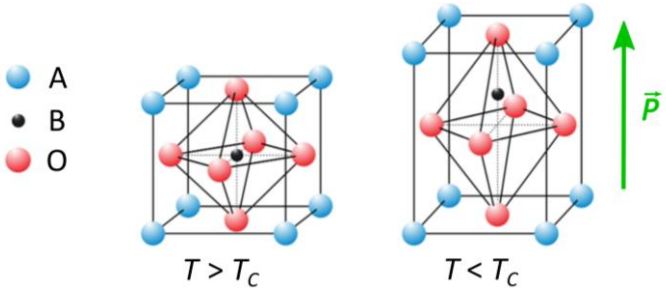

Figure 1: Schematic illustration of the perovskite structure ABO_3: cubic structure in the paraelectric phase (left) and tetragonal structure in the ferroelectric phase (right).

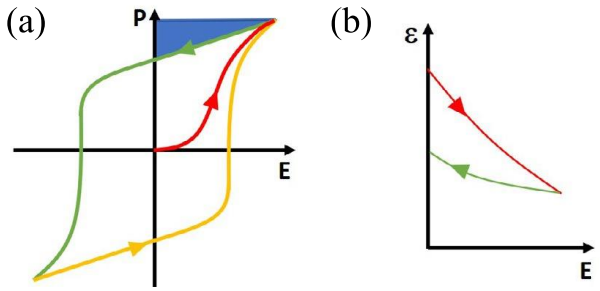

Figure 2: (a) Schematic illustration of a polarization hysteresis loop in ferroelectric materials. The red line represents the initial polarization curve, while the blue shaded area indicates the recoverable energy storage density. (b) Schematic representation of the dielectric permittivity as a function of increasing (red line) and decreasing (green line) electric field in ferroelectrics. The figure was adapted from [41].

The dielectric response consists of intrinsic (linear) and extrinsic (nonlinear) contributions. The intrinsic contribution in ferroelectrics arises from lattice deformation under applied subswitching electric fields, while the extrinsic contribution is associated with the motion of interfaces, such as phase boundaries and domain walls [40,42,43]. A schematic diagram of the polarization–electric field (P–E) loop for a ferroelectric material is shown in Figure 2a. Upon initial exposure to an applied DC electric field, the polarization begins to increase. As the electric field increases further, the majority of domains align in the direction of the field, leading to polarization saturation. When the electric field is removed, the polarization decreases slightly due to partial back-switching of domains, but a certain amount of polarization remains. This remaining polarization is known as the remanent polarization (P_r). If the electric field is subsequently applied in the opposite direction, the polarization begins to decrease and eventually changes sign. This sharp transition marks the main domain-switching event, and the electric field at which the polarization is reduced to zero is termed the coercive field. As the field continues to increase in the negative direction, the polarization again approaches a maximum (in the negative direction), and similarly, a remanent polarization remains upon removal of the field [39].

Once the ferroelectric phase is fully induced, i.e., poled, most domain walls are driven into alignment and become pinned, thereby eliminating their large, field-dependent contribution to the dielectric permittivity [44,45]. At the same time, the applied bias

hardens the soft phonon mode, which, via the Lyddane–Sachs–Teller relation, reduces the intrinsic lattice permittivity [46]. Both mechanisms are well-established in ferroelectrics and are responsible for the decrease in dielectric permittivity with increasing electric field (see Figure 2b).

Most ferroelectric materials undergo a structural phase transition from a low-temperature ferroelectric phase to a high-temperature paraelectric phase. Above the transition temperature, the dielectric permittivity follows the Curie–Weiss law:

$$\varepsilon' \approx \frac{C}{T - T_C} \tag{1}$$

where C is the Curie constant and T_C is the Curie temperature, i.e., the temperature at which the phase transition occurs [39]. During this transition, ferroelectric domains gradually vanish as the unit cells transform from a tetragonal to a cubic structure, thereby reducing the system's free energy. In this transitional regime, the material becomes highly susceptible to external influences, and ferroelectrics exhibit significantly enhanced dielectric and electromechanical responses. However, this so-called two-phase coexistence region typically exists within a narrow temperature range around T_C, which is generally far from room temperature (see Figure 3a,b) [40,47].

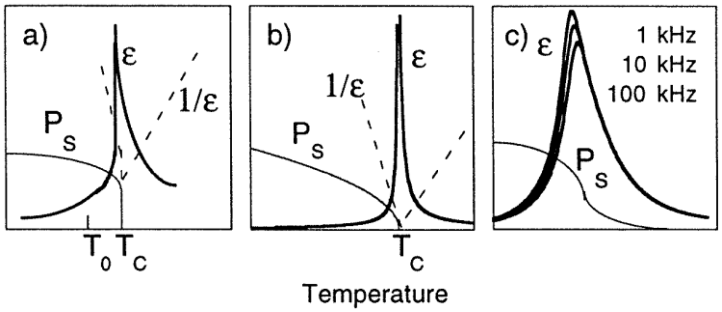

Figure 3: Schematic temperature dependence of the dielectric permittivity (ε) and spontaneous polarization (P_S) for (a) a first-order and (b) a second-order phase transition in ferroelectrics, and (c) relaxor ferroelectrics. The figure was taken from [39].

In general, free energy is a thermodynamic potential that determines the ability of a system to perform work under specific conditions by considering both internal energy and entropy. In ferroelectrics, a Ginzburg–Landau expansion of the free energy density (F) is often used to describe how the system's energy changes with spontaneous polarization near a phase transition [40]:

$$F(P,T) = \frac{1}{2}g_2P^2 + \frac{1}{4}g_4P^4 + \frac{1}{6}g_6P^6 - EP \tag{2}$$

where polarization (P) is the order parameter, g_2, g_4, and g_6 are temperature-dependent coefficients, and E is the external electric field.

Figure 4 shows the free energy density as a function of polarization across different temperature ranges. The minima of the free energy correspond to stable or metastable polarization states. Depending on the shape of the energy curve and the polarization behavior, two types of phase transitions can be distinguished: first-order and second-order phase transitions. A first-order phase transition is characterized by a discontinuous change in polarization at the transition temperature (see Figure 3a). During such a transition,

latent heat is exchanged: it is absorbed during heating, when the system transforms into a phase with higher enthalpy, and released upon cooling as the system returns to a lower-enthalpy phase. In contrast, a second-order (or continuous) phase transition involves a gradual, continuous decrease of polarization to zero at the critical temperature (see Figure 3b), and no latent heat is involved. In both cases, the dielectric permittivity exhibits a sharp increase near the phase transition temperature due to enhanced polarization fluctuations [40].

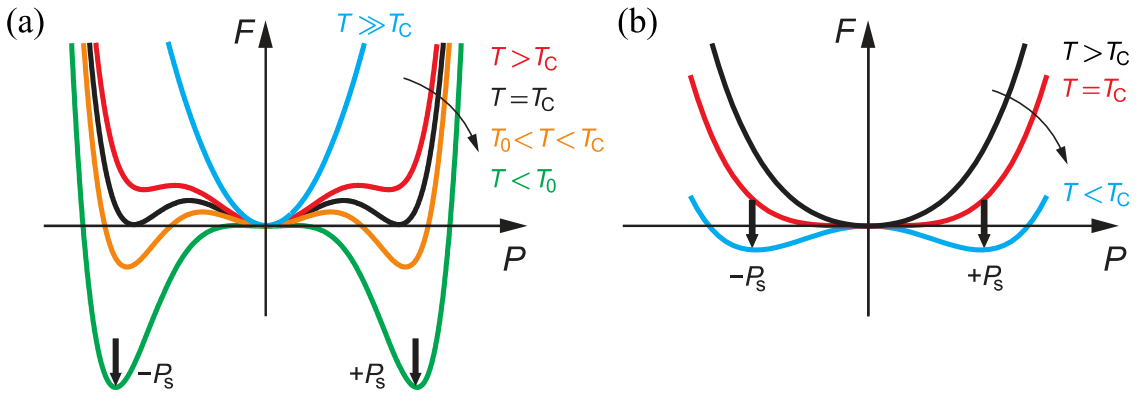

Figure 4: Free energy density as a function of polarization across different temperature ranges for a ferroelectric with (a) a first-order and (b) a second-order phase transition. Figures were taken from [40].

By applying an external electric field, both the nature and temperature of the phase transition in ferroelectrics can be modified, i.e., a first-order phase transition can be changed into a second-order or even a supercritical transition [48]. The critical electric field and the temperature of the crossover between the first- and second-order phase transitions define the critical point. Furthermore, if the second-order transition point represents a singular point that terminates the line of the first-order phase transitions, the point is referred to as the critical end point, above which a supercritical behavior is observed [49]. In the supercritical regime, the dielectric permittivity and heat capacity become non-critical and smeared out, while at the critical end point, both properties diverge, leading to an anomalous enhancement of functional properties such as the piezoelectric and electrocaloric response, as well as the energy storage density [50,51]. However, in ferroelectric materials, only a limited portion of the stored energy can be recovered due to significant losses associated with polarization reversal and large remanent polarization. The blue shaded area in Figure 2a represents the recoverable energy storage density (W_{rec}), which is defined by the equation [52]:

$$W_{rec} = \int_{P_r}^{P_{max}} EdP, \tag{3}$$

where E is the applied electric field, P_{max} is the maximum polarization, and P_r is the remanent polarization. W_{rec} is temperature dependent: both the maximum and remanent polarization decrease with increasing temperature and vanish at the ferroelectric-to-paraelectric phase transition temperature (T_C). Thus, upon approaching T_C, the P–E hysteresis loop becomes progressively slimmer and completely vanishes before transitioning into a linear (paraelectric) dielectric response [53].

Figure 5a shows the influence of various bias electric fields on the ferroelectric-to-paraelectric phase transition in barium titanate ($BaTiO_3$). With increasing electric field, the transition temperature rises, and the phase transition transforms from first-order to supercritical. The first-order nature of the transition is further confirmed by the release of latent heat during the field-induced tetragonal-to-cubic phase transition. Furthermore, the highest dielectric permittivity values are obtained near the critical end point, determined from the electric field–temperature phase diagram shown in Figure 5b [48].

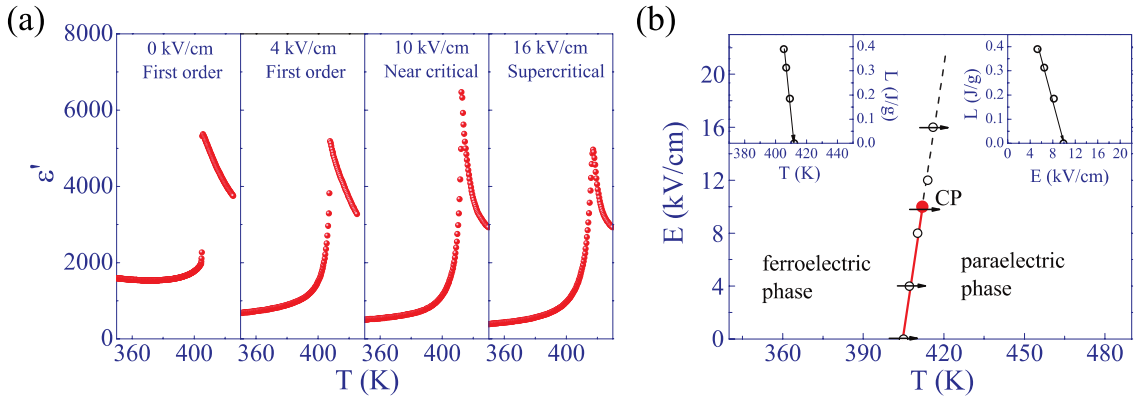

Figure 5: (a) Temperature dependence of the dielectric permittivity of a $BaTiO_3$ single crystal under various bias electric fields. (b) Electric field–temperature phase diagram for $BaTiO_3$. The solid line represents the electric field-induced first-order transition line between the ferroelectric and paraelectric phases, terminating at a critical end point at T_{CP} ≈412 K and E_{CP} ≈10 kV cm^{-1}. The insets show the temperature and electric field dependence of the latent heat. Figures were taken from [48].

Dielectric tunability (η) is defined as the relative change in dielectric permittivity under an applied electric field:

$$\eta = \frac{\varepsilon'(0) - \varepsilon'(E)}{\varepsilon'(0)} \times 100\ \%, \tag{4}$$

where $\varepsilon'(0)$ and $\varepsilon'(E)$ are the dielectric permittivities at zero and applied electric field E, respectively [54]. In ferroelectrics, dielectric tunability increases with increasing electric field, as the applied field drives the material toward polarization saturation, thereby reducing the dielectric permittivity. Barium strontium titanate ($Ba_xSr_{1-x}TiO_3$) is one of the most extensively studied ferroelectric materials for dielectric tunability. By tuning the Ba/Sr ratio, its Curie temperature can be shifted to room temperature, thereby reducing dielectric losses and optimizing tunability under modest bias fields. Figure 6a shows the evolution of dielectric permittivity under an applied DC electric field, while Figure 6b shows the dielectric tunability of different $Ba_xSr_{1-x}TiO_3$ compositions at room temperature. The highest dielectric tunability (approximately 20 %) is observed in a $Ba_{0.7}Sr_{0.3}TiO_3$ thick film under a DC bias field of 5.5 kV cm^{-1} [55].

Ferroelectric materials include a wide range of compounds, from perovskite-structured oxides such as barium titanate ($BaTiO_3$) [56], lead titanate ($PbTiO_3$), and potassium niobate ($KNbO_3$), to oxides with ilmenite structures (e.g., $LiNbO_3$), tungsten bronze and Aurivillius phases, as well as relaxor ferroelectrics, organic salts such as triglycine sulfate, and polymer ferroelectrics such as poly(vinylidene fluoride) (PVDF) and its copolymers [57].

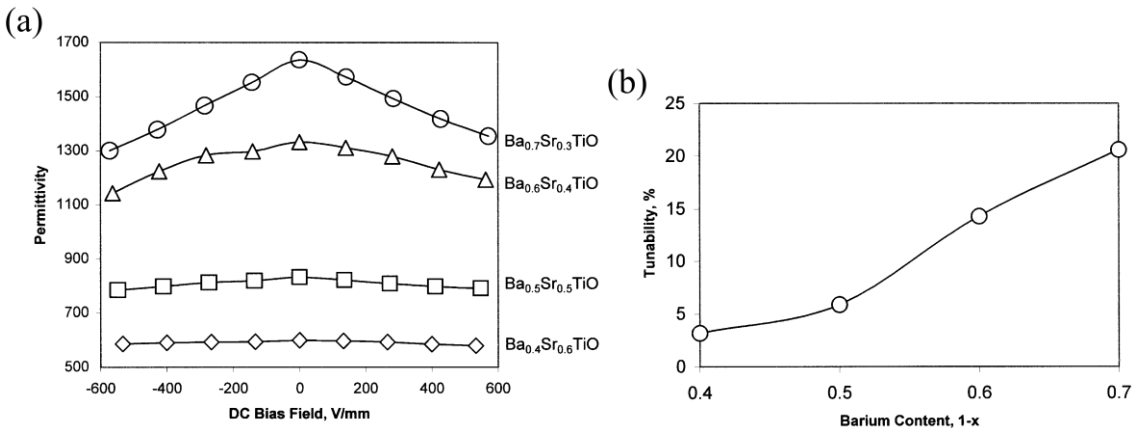

Figure 6: (a) Dielectric permittivity as a function of DC bias field and (b) dielectric tunability of $Ba_{1-x}Sr_xTiO_3$ thick films (x = 0.3–0.6) measured at room temperature. Figures were taken from [55].

To enhance the functional properties of classical ferroelectrics, various approaches have been developed and investigated, including chemical modification through doping [58], the preparation of solid solutions near the morphotropic phase boundary (MPB) [59,60], the fabrication of composites [61], the application of external and internal mechanical stress [62], and the exploitation of criticality [49,51].

Lead zirconate titanate ($Pb(Zr_xTi_{1-x})O_3$, PZT) is one of the most widely used commercial ferroelectric and piezoelectric materials. It is synthesized by mixing lead, zirconium, and titanium oxides, resulting in a ferroelectric solid solution with the MPB, i.e., a special compositional region where two or more distinct crystallographic phases with different symmetries and nearly equal free energies coexist. At the MPB, the energy barrier between polarization directions becomes very low, allowing easier rotation of polarization vectors under applied electric fields and resulting in enhanced dielectric properties such as dielectric permittivity and piezoelectric coefficients. By adjusting the Zr/Ti ratio in PZT, the MPB with coexisting tetragonal and rhombohedral phases occurs at x = 0.48 [63,64].

Sodium bismuth titanate ($Na_{0.5}Bi_{0.5}TiO_3$), on the other hand, is widely studied as a lead-free alternative to PZT for environmentally friendly piezoelectric ceramics. However, its piezoelectric response remains moderate compared to that of PZT.

2.1.1 Relaxor ferroelectrics

Relaxor ferroelectrics are frequently synthesized by doping a conventional ferroelectric material with suitable impurities. The structural behavior of relaxor ferroelectrics, commonly referred to as relaxors, resembles the two-phase coexistence region observed in ferroelectrics but extends over a much broader temperature range. Inorganic relaxors are typically compositionally disordered perovskites, characterized by a random distribution of different cations occupying the same crystallographic site. This chemical disorder forms nano-sized polar regions within a nonpolar matrix, which persist across a wide temperature range. Consequently, no transition into a long-range ferroelectric state occurs at any temperature in the absence of an external electric field. Furthermore, the broad peak of dielectric permittivity exhibits pronounced frequency dispersion and shifts to higher temperatures with increasing frequency (see Figure 3c). Relaxors do not follow the Curie–Weiss law; therefore, they do not exhibit a drop of polarization to zero at the temperature

of maximum dielectric permittivity. Instead, the polarization gradually decreases with increasing temperature and retains finite values to rather high temperatures due to the persistence of polar nanoregions [53].

At high temperatures, relaxors exhibit a slim P–E loop, characteristic of an ergodic state with dynamic polar nanoregions (see Figure 7). Polarization continues to increase gradually with increasing electric field, as there is no clear saturation in relaxor systems. Once the field is removed, most polar nanoregions return to their random orientations, resulting in a small remanent polarization. However, under a sufficiently strong electric field, the ergodic state can undergo a reversible transition into an induced ferroelectric phase, resulting in an ergodic loop with a reversible relaxor–ferroelectric crossover. At lower temperatures, or under prolonged field exposure, this transition may become irreversible, and the material enters a nonergodic state, displaying a classic ferroelectric hysteresis loop [53,65].

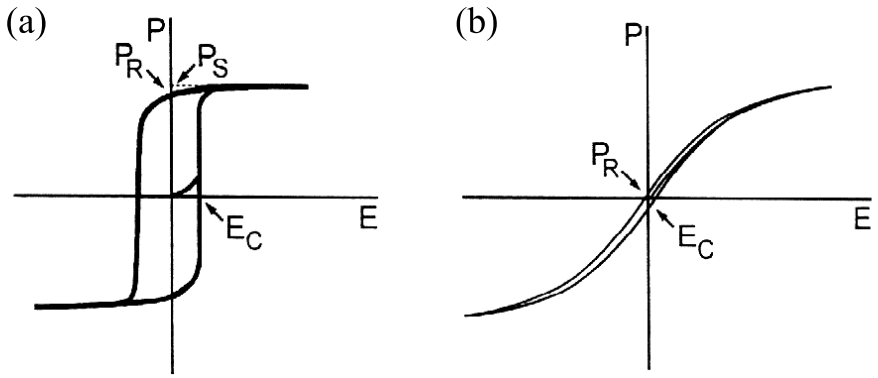

Figure 7: Polarization–electric field hysteresis in a ferroelectric (left) and a relaxor (right) system. The figure was adapted from [53].

Relaxors are known for their high energy storage efficiency compared to typical ferroelectrics. They exhibit a slim P–E hysteresis loop due to low remanent polarization and a low coercive field, resulting in low energy dissipation and high recoverable energy storage density (see Eq. (3)). Moreover, relaxors can withstand higher electric fields, leading to greater maximum polarization, which further enhances W_{rec}.

A representative example is PLZT ceramics, derived from PZT and doped with lanthanum. In PLZT, La^{3+} and Pb^{2+} ions are randomly distributed on the A-sites of the perovskite unit cell, O^{2-} ions occupy the face centers, while Ti^{4+} and Zr^{4+} ions are randomly located on the B-sites. As a result, PLZT exhibits high dielectric permittivity across a broad temperature range.

Modification of lead magnesium niobate ($Pb(Mg_{1/3}Nb_{2/3})O_3$, PMN) with lead titanate ($PbTiO_3$, PT) results in a gradual transition from relaxor to normal ferroelectric behavior at a critical composition $x_C \approx 0.33$ in the solid solution $(PMN)_{(1-x)}(PT)_x$. The system with $x<0.33$ remains a classical relaxor until a field-induced ferroelectric transition occurs [65]. Although the dielectric response is already enhanced at the MPB, which separates the rhombohedral and tetragonal ferroelectric phases, the dielectric permittivity reaches even higher values near the field-induced critical end point (see Figure 8a). Figure 8b shows the electric field–temperature phase diagram for the PMN–PT system near the MPB ($x = 0.295$), indicating the location of the critical end point at an accessible electric field of 1.3 kV cm^{-1} [49].

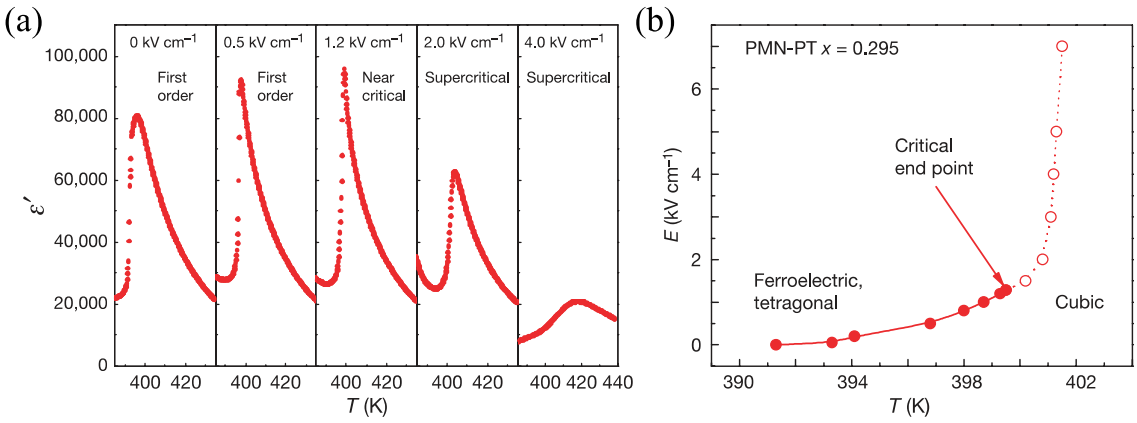

Figure 8: (a) Temperature dependence of the dielectric permittivity measured in the PMN–PT system with x = 0.295 under various bias electric fields. (b) Electric field–temperature phase diagram for the PMN–PT system with x = 0.295. Red circles denote first-order ferroelectric phase transitions, which terminate at a critical end point at E_{CP} =1.3 kV cm^{-1}. Open circles above the critical end point denote the positions of smeared-out anomalies that gradually disappear at higher fields in the supercritical region. Phase labels correspond to the zero-field phases. Figures were taken from [49].

Furthermore, an exceptionally high dielectric tunability of 87 %, with minimal dielectric dispersion and hysteresis, was observed near the critical end point of $Pb(Zn_{1/3}Nb_{2/3})O_3$–9%PT ceramics. Although the operating temperature (460 K) was much higher than room temperature, this result confirms that operation in the proximity of a critical end point is a promising approach for enhancing the functional properties of relaxors [66].

2.2 Antiferroelectric Materials

Antiferroelectric materials are a subgroup of dielectric materials with spontaneous polarization in which adjacent dipoles are arranged antiparallel so that their unit cells and the material have zero macroscopic polarization in the absence of an external electric field. However, an externally applied electric field of sufficient magnitude can induce a phase transition to a ferroelectric phase with a polar space group and ordered parallel dipole moments to build a non-zero macroscopic polarization [41,67–71]. If this transition is reversible, the material switches back to the antiferroelectric phase when the electric field is reduced below the critical electric field. The reversibility of the electric field-induced phase transition results in a double hysteresis loop, a characteristic fingerprint of antiferroelectrics (see Figure 9).

In antiferroelectric (AFE) materials, the P–E loop exhibits a distinctly different shape than in ferroelectric (FE) materials. At low electric fields, the material displays very low net polarization due to the antiparallel alignment of adjacent dipoles, characteristic of the antiferroelectric phase (see Figure 10). When the electric field exceeds a critical threshold (E_{AFE-FE}), the system undergoes a field-induced phase transition to a ferroelectric state with aligned dipoles, resulting in a sharp increase in polarization. A further increase in the electric field leads to polarization saturation, similar to the behavior observed in ferroelectric materials. Upon reducing the electric field, the polarization decreases, and as the field drops below a critical threshold (E_{FE-AFE}), the material reverts to the

antiferroelectric state, resulting in a sharp decrease in polarization. When the electric field is subsequently applied in the opposite direction and exceeds the critical threshold, the material again undergoes a transition to the ferroelectric state with polarization oriented in the opposite direction. As the field is reduced, the material returns to the antiferroelectric state, completing the characteristic double hysteresis loop.

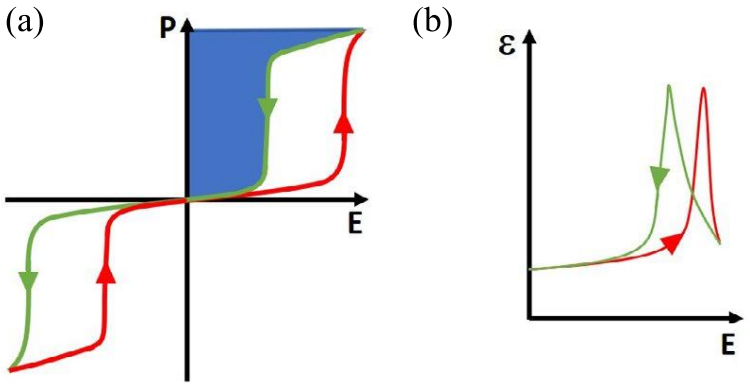

Figure 9: (a) Schematic illustration of a polarization hysteresis loop in antiferroelectrics. The blue shaded area corresponds to the recoverable energy storage density. (b) Schematic representation of the dielectric permittivity as a function of increasing (red line) and decreasing (green line) electric field in antiferroelectrics. The figure was adapted from [41].

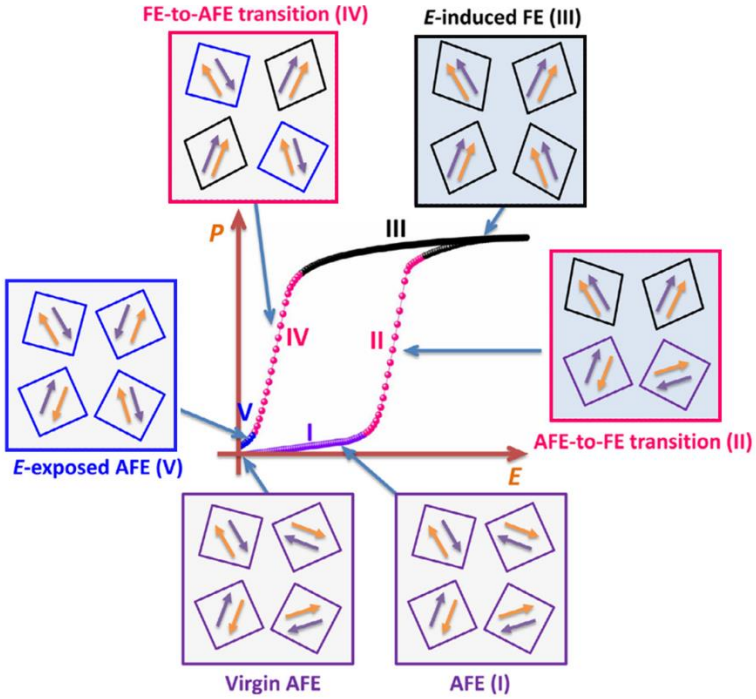

Figure 10: Schematic illustration of the first half-cycle of the polarization–electric field hysteresis in antiferroelectrics and the corresponding domain orientations: (I) a minor polarization change from the virgin AFE state, (II) the field-induced AFE–FE phase transition, (III) the polarization saturation in the FE phase, (IV) the FE–AFE phase reversal upon reducing the field, and (V) an AFE state with domains retaining their FE-induced orientation. The figure was adapted from [71].

The double hysteresis loop and low remanent polarization provide a more rectangular and symmetric P–E response, allowing for a larger proportion of the stored energy to be released during discharge. This makes antiferroelectrics particularly attractive for high-efficiency energy storage applications. The blue shaded area in Figure 9a represents the recoverable energy density. Moreover, W_{rec} is strongly dependent on P_{max} and E, where E is limited by the dielectric breakdown strength, as well as by the critical electric fields (E_{AFE-FE}, E_{FE-AFE}) and switching hysteresis ($\Delta E = E_{AFE-FE} - E_{FE-AFE}$). Thus, a good antiferroelectric material should possess high E_{AFE-FE}, E_{FE-AFE}, P_{max}, as well as low P_r, to ensure a large recoverable energy storage density (see Eq. (3)). A small ΔE is also desirable to achieve high efficiency. Needless to say, a high dielectric breakdown strength is necessary to guarantee a high applied electric field for inducing AFE–FE phase transition [52].

Figure 9b exhibits an increase in dielectric permittivity with increasing electric field up to a critical value, at which a field-induced AFE–FE phase transition occurs. Beyond this transition, the dielectric response resembles that of classical ferroelectrics, with permittivity decreasing due to the reduced domain dynamic and/or saturation of polarization [44,45].

In order for switching between phases to occur, the free energies of antiferroelectric and ferroelectric states need to be similar. The polar instability at the field-induced phase transition is often considered the origin of the peculiar electrical [72,73], thermal [74], and mechanical [37] properties of antiferroelectrics, such as the negative electrocaloric effect [75–77], an increase in dielectric permittivity with increasing electric field [73,78–80], high strain response [81], high energy storage density [52], and negative capacitance [72]. Hence, the applicability of antiferroelectrics ranges from pulse-power capacitors [82], DC-link capacitors for power electronics [83], electromechanical actuators [84], capacitor memory cells [85,86], voltage signal amplifiers to solid-state coolants [77], and more.

In antiferroelectrics, the dielectric tunability (η) is defined as:

$$\eta = \frac{\varepsilon'_{max}(E) - \varepsilon'(0)}{\varepsilon'(0)} \times 100\ \%, \tag{5}$$

where $\varepsilon'_{max}(E)$ is the maximum dielectric permittivity of the antiferroelectric phase and $\varepsilon'(0)$ is the dielectric permittivity at zero electric field. Note that the numerator of Eq. (5) differs from the conventional equation for tunability used in dielectrics (see Eq. (4)). Here, $\varepsilon'_{max}(E)$ and $\varepsilon'(0)$ are switched, which satisfies the condition that the dielectric permittivity increases with electric field and gives positive value for the tunability.

The antiferroelectric structure is often found in perovskite-type oxides. In terms of structure, there are two types of AFEs: orthorhombic AFE (AFE_O) and tetragonal AFE (AFE_T). Due to their different phase structures, temperature-dependent phase transitions of the two AFEs are quite different [32]. With increasing temperature, AFE_O usually experiences a phase switching from AFE to FE and then to PE [87,88]. AFE_T goes through a phase transition from FE to AFE and then to PE, as the temperature is increased [89,90].

The most common approach to investigate the formation and stabilization of the antiferroelectric structure and its properties is chemical modification of canonical antiferroelectrics, such as lead zirconate ($PbZrO_3$) [31], silver niobate ($AgNbO_3$) [91], and sodium niobate ($NaNbO_3$) [92].

$AgNbO_3$ is an environmentally friendly antiferroelectric material that exhibits relatively high dielectric permittivity, making it suitable for capacitor applications. However, silver is expensive and can be volatile during sintering, potentially leading to stoichiometric imbalance or the formation of defects, which complicates processing and hinders reproducibility [93]. To enhance its performance, $AgNbO_3$ is often doped with elements

such as Ba, K, Ta, or rare-earth elements. In Ta-modified $AgNbO_3$ ceramics, a recoverable energy density of 4.2 J cm^{-3} has been achieved over a wide temperature range, which is 2.6 times higher than that of pure $AgNbO_3$ [52]. Co-doping $AgNbO_3$ with Nd and Ta further stabilizes the antiferroelectric phase, thereby increasing both the critical electric field required for the field-induced phase transition and the dielectric breakdown strength. Furthermore, a recoverable energy density of 6.5 J cm^{-3} has been reported in $Ag_{0.97}Nd_{0.01}Ta_{0.20}Nb_{0.80}O_3$ at an applied field of 370 kV cm^{-1}, a value comparable to that of lead-based ceramics [91].

$NaNbO_3$ is a promising lead-free alternative; however, it exhibits weak piezoelectric properties due to its irreversible AFE−FE phase transition [94]. Nevertheless, a reversible phase transition, characterized by a double polarization hysteresis loop, has been successfully achieved in $NaNbO_3$-based systems such as $NaNbO_3$-$CaZrO_3$ [95] and $NaNbO_3$-$SrSnO_3$ [96].

Therefore, the number of known antiferroelectric material systems, particularly those in which AFE−FE phase transition can be reversibly triggered, remains very limited. Although $PbZrO_3$-based materials have been more extensively studied than lead-free antiferroelectrics, the origin of antiferroelectricity is still not well understood. Moreover, the functionality of antiferroelectrics and the range of applications that this functionality could enable are still poorly explored, especially in comparison to ferroelectrics. One of the unique and attractive properties of antiferroelectric materials is the increase in dielectric permittivity with increasing electric field, which is especially pronounced in $PbZrO_3$-based materials. The underlying reason for this strong field response remains unclear, but it may be related to the proximity of a triple point where the metastable ferroelectric, antiferroelectric, and paraelectric (PE) phases merge [94,97,98].

Various strategies have been employed to tailor the phase transformation behavior of antiferroelectric materials to enhance their performance. Due to their relatively low dielectric breakdown strength, most $PbZrO_3$-based orthorhombic AFE ceramics are broken down before a critical switching field can be applied. As a result, they are often chemically modified, typically by adding Sn, Ti, and Nb or La, to reduce the critical field and optimize their properties [99]. Among the most prominent modified $PbZrO_3$-based systems known to exhibit a reversible phase transition at room temperature are the (Pb,La)(Zr,Sn,Ti)O_3 (PLZST) and (Pb,Nb)(Zr,Sn,Ti)O_3 (PNZST) [94].

PNZST is a $PbZrO_3$-based antiferroelectric ceramics with substituted zirconium at B sites with Sn, Ti, and Nb. Sn^{4+} enhances incommensurate modulation, which stabilizes the antiferroelectric phase and increases the AFE−FE switching field [32], while Ti^{4+} stabilizes the ferroelectric phase, increases induced polarization, and lowers the AFE−FE switching field [32,84]. At the same time, Nb^{5+} acts as a donor, reducing oxygen vacancies (improving leakage currents and dielectric losses) and enhancing ferroelectric stability, thereby reducing the AFE−FE switching field [99].

Furthermore, modifying the chemical composition also changes the phase transition temperatures, e.g., Ti-fraction in PNZST lowers the AFE−FE transition temperature [84]. On the other hand, increasing the pressure (compressing the lattice) stabilizes the AFE order and pushes the AFE−FE or AFE−PE transition to higher temperatures [100]. Moreover, applying a DC electric field on the sample lowers the AFE−PE phase transition temperature and increases the FE−AFE phase transition temperature as the electric field stabilizes the ferroelectric state during a heating run in a PNZST system [84,98]. Thereby, both phase boundaries in the electric field−temperature phase diagram are tilted towards each other and should merge at a triple point where FE, AFE, and PE phases coexist. The existence of a triple point in a PNZST antiferroelectric ceramics, where the rhombohedral

ferroelectric phase (FE_R), tetragonal antiferroelectric phase (AFE_T), and paraelectric multicell cubic phase (PE) coexist, was identified in the electric field–temperature phase diagram shown in Figure 11 [98]. The diagram was constructed based on isofield, temperature-dependent dielectric permittivity measurements during heating. While the study focused on the electrocaloric effect and its correlation to the triple point, a detailed investigation into the nature of the phase transitions in the vicinity of the triple point is still missing. Moreover, identifying a critical point or critical end point could lead to enhanced functional properties, as demonstrated in ferroelectric materials.

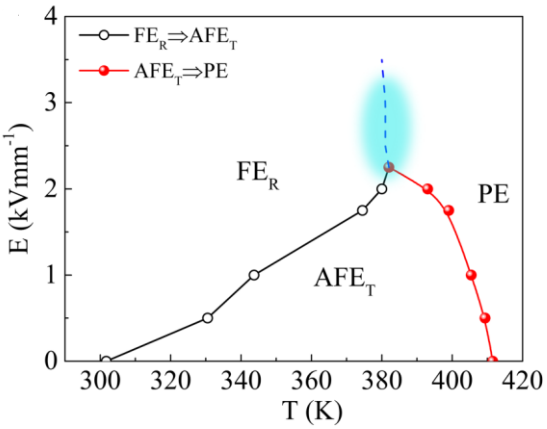

Figure 11: Isofield electric field–temperature phase diagram for PNZST antiferroelectric ceramics reveals the presence of a triple point around 380 K and 2.25 kV mm^{-1}. The shadowed area marks the estimated electric field and temperature phase coexistence regime around the triple point. The figure was taken from [98].

2.3 Composites

Another commonly used method to enhance the dielectric response is the composite approach, in which conductive particles are dispersed within the dielectric matrix to effectively increase the dielectric permittivity of the composite material. Even dielectric particles in a composite act as additional dipole moments under an applied electric field, contributing to the total polarization of the composite and significantly increasing its dielectric permittivity. However, the contribution is much higher when a conductive filler is used.

The effect in which electric charge accumulates at the interface between two materials with different dielectric permittivity and electrical conductivity is called the Maxwell–Wagner interfacial polarization. It occurs in electrically heterogeneous materials and is illustrated in Figure 12 for a spherical particle within a matrix under an external electric field. Charges within the sphere migrate to the interface according to Coulomb's law and attract opposite charges from the surrounding material to the sphere's surface. By increasing the number of particles, their overall contribution is enhanced. Moreover, the contribution is heavily amplified when conductive filler particles are used. The dielectric permittivity of the composite then follows percolation theory as the number of conductive particles, i.e., the filler volume ratio, increases.

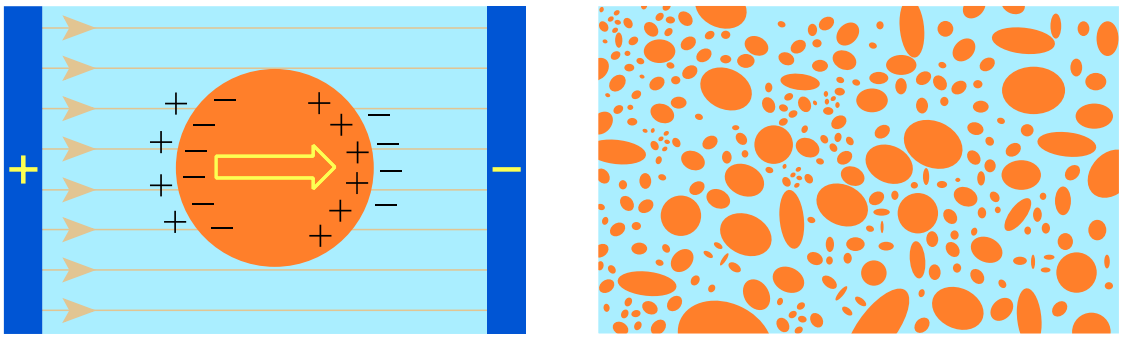

Figure 12: Schematic illustration of Maxwell–Wagner interfacial polarization for a spherical particle within a matrix under an external electric field (left) and a percolative composite (right; orange and blue regions represent conductive and dielectric/ferroelectric material, respectively).

The theory of percolation in general explains a physical process in which a macroscopic magnitude is strongly modified due to small microscopic changes in connectivity [101]. One such process is the anomalous behavior observed in metal-insulator composites (so-called percolative composites, Figure 12) near their percolation threshold, which is characterized by an abrupt discontinuity in the real part of the electrical conductivity [102—104]. The theory further predicts that the dielectric permittivity of a composite consisting of a conductive filler embedded in a dielectric matrix diverges at the percolation threshold, where the insulator-metal transition occurs [102]. The fact that the effective dielectric permittivity of the mixture is much larger than the values of the individual constituents can be intuitively understood through a simple geometrical approach: near the percolation threshold, numerous conducting particles are isolated only by thin dielectric layers.

An excellent review of a system composed of randomly distributed metallic and dielectric regions is given in the paper by Efros and Shklovskii [102]: it is shown that the static dielectric constant diverges at the percolation threshold–at the volume fraction of metallic regions (p) where the insulator-to-metal transition occurs, i.e., the static effective electrical conductivity (σ) undergoes a transition from

$$\sigma = \sigma_{diel} \left(\frac{p_c - p}{p_c} \right)^{-q} \tag{6}$$

which is valid below the percolation threshold p_c into

$$\sigma = \sigma_{metal} \left(\frac{p - p_c}{p_c} \right)^{t} \tag{7}$$

which holds true for $p > p_c$. σ_{diel} and σ_{metal} are conductivities of the dielectric and metallic phases, respectively, while q and t are critical exponents that govern the effective conductivity of the composite material below and above the percolation threshold. The theoretical dependence of the effective electrical conductivity for a system consisting of randomly distributed metallic and dielectric regions is depicted in Figure 13. A smooth transition between the behaviors described by Eqs. (6) and (7) occurs within a small interval near the percolation threshold.

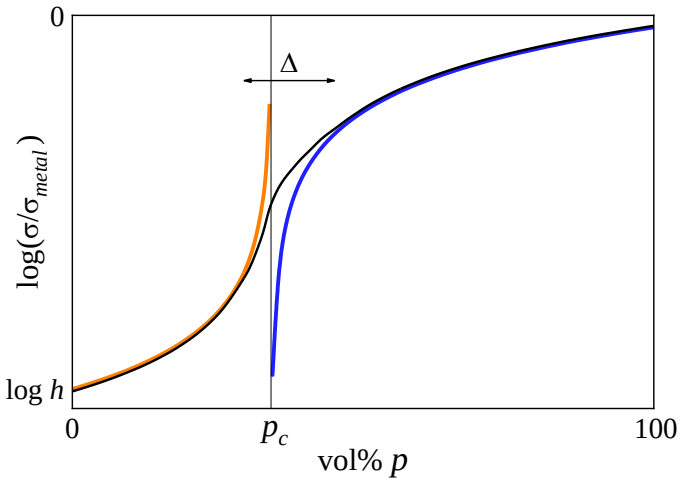

Figure 13: Theoretical dependence of the effective electrical conductivity (σ) on the volume fraction of metallic regions (p) for a system with randomly distributed metallic and dielectric regions ($h = \sigma_{diel}/\sigma_{metal} \ll 1$). A smooth transition between the behaviors described by Eq. (6) (orange line) and Eq. (7) (blue line) occurs within a small interval Δ near the percolation threshold (p_c).

The composite approach, in which conductive particles are dispersed within an insulating dielectric or ferroelectric matrix, has been successfully realized in both polymeric and inorganic systems.

2.3.1 Ceramic composites

A divergent evolution of the dielectric permittivity was achieved in a ceramic $BaTiO_3$-Ni composite, in which conductive nickel particles were homogeneously dispersed within a ferroelectric $BaTiO_3$ matrix. The first percolative capacitors made from this composite exhibited an extraordinarily high dielectric permittivity ($\varepsilon' \approx 80{,}000$), which was nearly independent of both frequency and temperature [105]. While the composite approach effectively increases dielectric permittivity due to a large Maxwell–Wagner interfacial polarization, it also boosts dielectric losses ($\tan\delta = \varepsilon''/\varepsilon'$). According to the Kramers–Kronig relations, the real part of the complex dielectric constant, i.e., dielectric permittivity (ε'), and the imaginary part of the complex dielectric constant (ε'') increase simultaneously, ultimately inflating the dielectric losses.

2.3.1.1 All-ceramic percolative composites

An identical behavior was observed in all-ceramic percolative composites, composed of conducting and insulating grains. The constituents were carefully selected to prevent chemical reactions between them during high-temperature sintering. A uniform distribution of the conductive filler throughout the ferroelectric matrix in the PZT–$Pb_2Ru_2O_{6.5}$ and $K_{0.5}Na_{0.5}NbO_3$–RuO_2 (KNN–RuO_2) composite systems is shown in Figure 14. In both systems, the dielectric permittivity increased by two orders of magnitude near the percolation threshold compared with pure PZT and KNN ceramics. The evolution of the dielectric permittivity with increasing conductive content for both systems is depicted in Figure 15 [106,107].

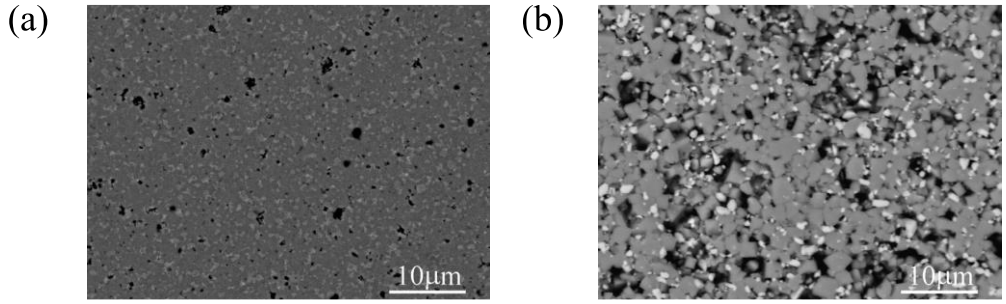

Figure 14: Microstructures of (a) PZT–$Pb_2Ru_2O_{6.5}$ composite with 15 vol% of $Pb_2Ru_2O_{6.5}$ and (b) KNN–RuO_2 composite with 15 vol% of RuO_2. Light areas represent dispersed conductive grains in the grey ferroelectric matrix, while black areas indicate pores in the structure. Figures (a) and (b) were taken from [106] and [107], respectively.

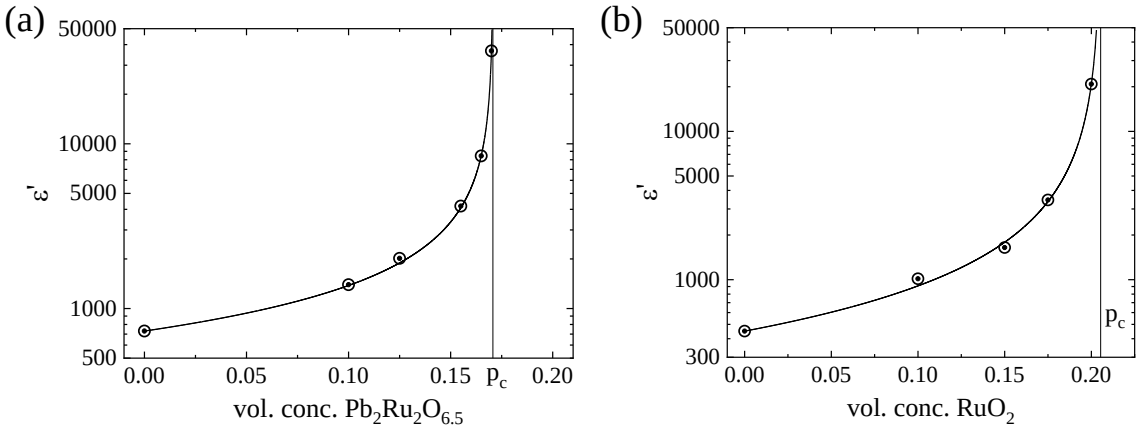

Figure 15: Evolution of the dielectric permittivity at 1 kHz with increasing conductive content in (a) PZT–$Pb_2Ru_2O_{6.5}$ and (b) KNN–RuO_2 composites. Figures (a) and (b) were taken from [106] and [107], respectively.

KNN was developed in an effort to minimize lead content in electronics and potentially replace PZT. Although lead-based materials have thus far exhibited a significantly higher dielectric response, selecting grains with approximately seven times higher electrical conductivity and increasing the amount of conductive particles can minimize this gap. As a result, the dielectric permittivity values in both systems become comparable (see Figure 15), confirming that the composite approach is an effective strategy for developing eco-friendly, lead-free materials for various applications.

2.3.2 Polymer percolative composites

The development of high-dielectric permittivity materials is particularly desired in the field of electroactive materials. During electromechanical operation, the amount of electric energy that can be converted into strain energy is directly proportional to the dielectric permittivity:

$$\frac{1}{2}\varepsilon_0\varepsilon' E^2 \geq \frac{1}{2}kx^2 \tag{8}$$

Therefore, increasing the dielectric permittivity allows the desired strain to be induced under a significantly reduced electric field. Here is an example from the field of relaxor polymers. Electroactive polymers based on poly(vinylidene fluoride-trifluoroethylene) copolymer, P(VDF-TrFE), have exhibited a giant electrostrictive strain of 5 % after high-energy irradiation, which is two orders of magnitude higher than that observed in inorganic piezoelectrics [108]. Furthermore, it has been shown that substantial electrostriction can also be achieved by incorporating chlorotrifluoroethylene (CTFE) as a third bulky monomer to form P(VDF-TrFE-CTFE) terpolymers, rather than relying on irradiation. This modification transforms the material into a relaxor-like system. Because polymers typically exhibit relatively low dielectric permittivity, extremely high external electric fields are required to induce this otherwise giant electromechanical response. For example, an electric field of 150 MV m^{-1} was needed to induce a 4 % thickness strain in P(VDF-TrFE-CTFE) terpolymers [109]. However, dispersing conductive polyaniline (cPANI) particles into the P(VDF-TrFE-CTFE) terpolymer increases the dielectric permittivity by two orders of magnitude near the percolation threshold (25.9 vol% cPANI; see Figure 16) [110,111]. Embedding cPANI particles consequently enables significant strain under much lower external electric fields [8].

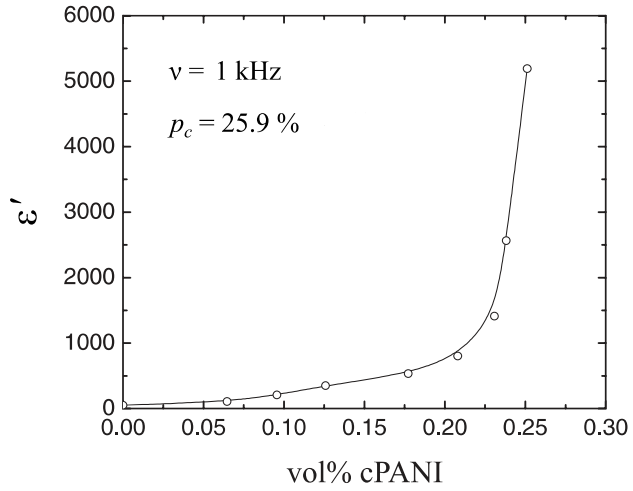

Figure 16: Evolution of the dielectric permittivity at 1 kHz for cPANI–P(VDF-TrFE-CTFE) composites as a function of cPANI volume concentration. The figure was adapted from [110].

2.3.2.1 Cellulose composites

Biopolymers such as cellulose have been proposed as an auspicious base material for flexible electronics due to their low cost and biodegradability [17,18]. Native wood cellulose can be converted into individual nanofibrils 3–4 nm wide and several microns in length, exhibiting a high aspect ratio [112], a high elastic modulus (138 GPa) [113], and a low thermal expansivity (0.1 ppm K^{-1}) [114] compared to other polymers. Cellulose nanofibrils (CNFs) are isolated from wood pulp either by physical or chemical methods. The physical method involves applying high shear forces to rip apart larger wood fibers by using high-pressure homogenizers, ultrasonic homogenizers, grinders, or microfluidizers, making this method very energy-consuming. Therefore, enzymatic or mechanical pre-treatments and the introduction of charged groups, e.g., through carboxymethylation or (2,2,6,6-

tetramethylpiperidin-1-yl)oxyl (TEMPO)-mediated oxidation, are commonly employed to significantly reduce energy consumption. Furthermore, TEMPO oxidation of cellulose results in a high density of carboxylate groups on the surfaces of cellulose nanofibrils, enabling homogeneous dispersion in composites and further improving their physical properties [115−117]. Since the high dielectric permittivity is crucial for energy storage applications, the main strategy in the fabrication of flexible cellulose-based materials with enhanced dielectric performance focuses on incorporating nano-additives such as carbon nanotubes and graphene-based nanosheets, due to their ultra-high specific surface area and excellent electrical properties [18].

With the two-dimensional sheet-like structure with covalently attached carbon atoms having various functional groups on the edges and basal planes, graphene oxide shows excellent dispersibility in polymeric matrices [118]. However, for the fabrication of electronic devices, its low electrical conductivity, caused by the high density of chemical functional groups attached to a carbon plane and by structural defects within the plane [20], limits its applicability. To overcome this limitation, ammonia-functionalized graphene oxide [19] or reduced graphene oxide [119] is widely used as a filler for the fabrication of high-ε' flexible cellulose-based films, which substantially increase dielectric permittivity even at low filler content due to a large Maxwell–Wagner interfacial polarization. Moreover, incorporating ammonia-functionalized graphene oxide into a CNF or TEMPO-oxidized cellulose matrix results in composites that are both mechanically strong and thermally stable [119].

2.4 High Dielectric Breakdown Systems

One of the major challenges in developing dielectric polymers is realizing high energy density while maintaining low dielectric losses, even under very high applied electric fields [120]. The composite approach, in addition to increasing dielectric permittivity, also boosts dielectric losses. An alternative approach is to operate under higher electric fields, i.e., increasing the dielectric breakdown strength without increasing the dielectric permittivity, which, via the Kramers−Kronig relations, always inflates dielectric losses. Moreover, the electric energy density is only linearly proportional to the dielectric permittivity, while its maximum value depends quadratically on the dielectric breakdown strength, following the relation: $U_e \propto \varepsilon' {E_b}^2$. Classical models suggest that the intrinsic breakdown strength of dielectric polymers exceeds 1 GV m^{-1} due to their large energy bandgap and small mean free path for mobile charges [121]. However, experimentally obtained dielectric breakdown strength values in many widely used polymers are significantly lower due to imperfect chain packing, such as coiled and entangled polymer chains, resulting in weak points such as free volume and structural disorder [121−123]. Therefore, new approaches that increase chain packing density and reduce the number of weak points and structural disorder in polymers, thereby enhancing breakdown strength without increasing dielectric permittivity, are highly desirable.

Chapter 3

Aims and Hypotheses

Designing and developing new materials with enhanced dielectric properties is crucial for technological innovation, scientific understanding, and ecological sustainability. The main aim of this dissertation is to conduct a detailed investigation of newly developed materials to improve their dielectric properties. This investigation will evaluate three conceptually different approaches to designing novel organic and inorganic materials with enhanced dielectric response. The results will provide new insights into the correlation between structure and property evolution in different systems, which is important both fundamentally and practically for the development of new materials for advanced dielectric applications.

This dissertation aims to achieve the following goals for polymer systems:

- Providing information on how dielectric properties can be tailored and/or improved by changing the composition of the polymer system.
- Enhancing dielectric response by embedding MXenes into a cellulose nanofibrils matrix.
- Successfully synthesizing poly(ether imide)/polyimide blends from poly(ether imide) pellets and polyimide powder by the solution casting method.
- Determining the origin of enhanced dielectric breakdown strength, and other possible contributions to the dielectric response of poly(ether imide)/polyimide blends.

The goals for the antiferroelectric $Pb_{0.99}Nb_{0.02}[(Zr_{0.57}Sn_{0.43})_{0.92}Ti_{0.08}]_{0.98}O_3$ (PNZST) ceramics are:

- Determining the electric field–temperature phase diagram of the investigated antiferroelectric system.
- Identifying the position of the critical end point in the electric field–temperature phase diagram.
- Elucidating the impact of the critical end point on functional properties (polarization, dielectric tunability, energy storage) of the antiferroelectric material.

The following hypotheses are formed individually for each investigated system based on fundamental physical and chemical phenomena:

- The dielectric permittivity will increase strongly upon approaching the percolation threshold in cellulose nanofibrils-$Ti_3C_2T_x$ MXene composites due to pronounced Maxwell–Wagner polarization.

- Blending poly(ether imide) with polyimide will significantly enhance dielectric breakdown strength compared to pristine polymers due to (i) a reduced number of space charges and (ii) increased chain packing density. Because dielectric breakdown is initiated by charges accelerated by an applied electric field at weak points (voids), both (i) and (ii) are expected to contribute to this enhancement. Low-frequency dielectric measurements will reveal a significant reduction of accumulated space charges in the blends compared to pristine polymers, and a comparison of annealed (dry) and unannealed (wet) samples will confirm the higher chain packing density.
- The presence of an electric field-induced critical end point in PNZST antiferroelectric ceramics will enhance polarization, dielectric tunability, and energy storage capability.

Chapter 4

Materials Preparation

Several polymer samples were prepared with the aim of investigating the influence of composition on the dielectric response of the material. The cellulose/MXene composites were synthesized by a collaborative research group at the Faculty of Mechanical Engineering, University of Maribor, while the poly(ether imide)/polyimide blend films were prepared at the Jožef Stefan Institute by me.

The ceramic sample with chemical formula $Pb_{0.99}Nb_{0.02}[(Zr_{0.57}Sn_{0.43})_{0.92}Ti_{0.08}]_{0.98}O_3$ (abbreviated as PNZST) was obtained from the Technical University of Darmstadt and fabricated using a mixed-oxide route, as described elsewhere [124].

4.1 Cellulose/MXene Composites

Multi- and few-layered 2D $Ti_3C_2T_x$ MXene powders with accordion-like morphology, consisting of well-packed and aligned 10–20 nm thin nanosheets, were purchased from Nanochemazone (Canada) and used as received. In $Ti_3C_2T_x$, T represents a hydroxyl, oxygen, or fluorine surface termination group. The multi-layered MXene powders were 10–20 μm thick, while the few-layered powders had a thickness of ≈1 μm. In addition, titanium aluminum carbide (Ti_3AlC_2) powder (MAX phase) of 10–30 μm in diameter was obtained to self-prepare the MXene by the hydrofluoric acid etching method at room temperature [125]. Here, 0.5 g of Ti_3AlC_2 powder was dispersed in 10 mL of 30 % hydrofluoric acid by magnetic stirring at 20 rpm for 24 h. Then, the sample was washed several times with deionized water via centrifugation until the supernatant pH value reached ≈6. The $Ti_3C_2T_x$ sediments were rewashed with deionized water via vacuum-assisted filtration using a polyvinyl difluoride filter membrane with 0.22 μm pore size before collection of the remaining MXene. Then, the sample was intercalated/delaminated by magnetic stirring at 20 rpm for 24 h in dimethylsulfoxide, followed by 1 h of sonication at 20 % amplitude using a Vibra Cell VCX 750 sonicator (Sonics, USA). Finally, the obtained MXene powder was vacuum-dried at 375 K for 24 h [126].

Figure 17 shows cross-sectional scanning electron microscopy (SEM) images of purchased multi-layered titanium carbide MXene powder and self-prepared MXenes. Both images confirm the accordion-like morphology of well-packed and aligned MXene nanosheets, 10–20 nm thick.

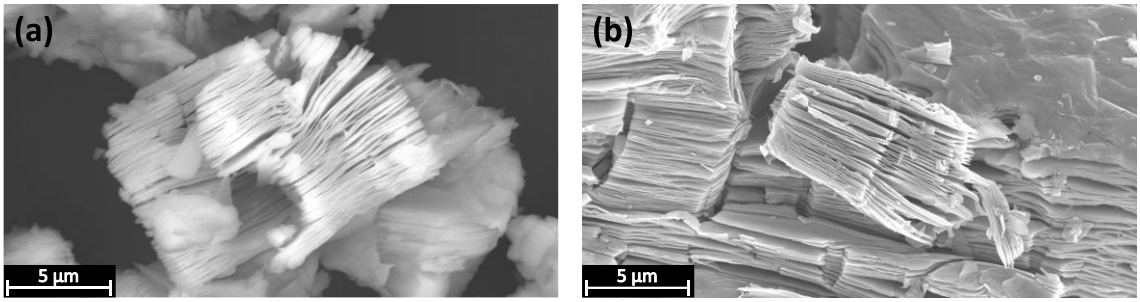

Figure 17: Cross-sectional SEM images of (a) multi-layered titanium carbide MXene powder purchased from Nanochemazone and (b) self-prepared MXenes.

Cellulose nanofibrils (CNF) or (2,2,6,6-tetramethylpiperidin-1-yl)oxyl (TEMPO) oxidized CNF (TCNF), with lengths of 1–3 μm and diameters of 10–70 nm, were derived from bleached softwood pulp at the University of Maine, USA. Pristine cellulose and CNF- or TCNF-based MXene composite films were prepared either by the solvent casting or vacuum filtration methods. Various quantities of the $Ti_3C_2T_x$ powder were homogeneously dispersed in 15 mL of dimethyl sulfoxide by an ultrasonic processor, then mixed with an appropriate amount of Milli-Q water-suspended CNF/TCNF, and stirred for 1 h to get homogeneous cellulose/MXene dispersions. The dispersions were poured directly into polystyrene Petri dishes and dried at room temperature (solvent-casted films), or vacuum filtered through a cellulose filter with a pore size of 5–8 μm, transferred in a wet stage to Petri dishes of 6 cm in diameter, left to dry at room temperature, and finally pressed at 4 bar for 5 h with a hydraulic press. The thickness of developed films was ≈40 μm in the case of pristine cellulose, while it increased to almost 300 μm in samples with 90 wt% MXene [126].

4.2 Poly(ether imide)/Polyimide Blends

Poly(ether imide) (product name Ultem 1000) pellets and polyimide (Matrimid 5218) powder were supplied by PolyK Technologies. The schematic chemical structures of both compounds are shown in Figure 18.

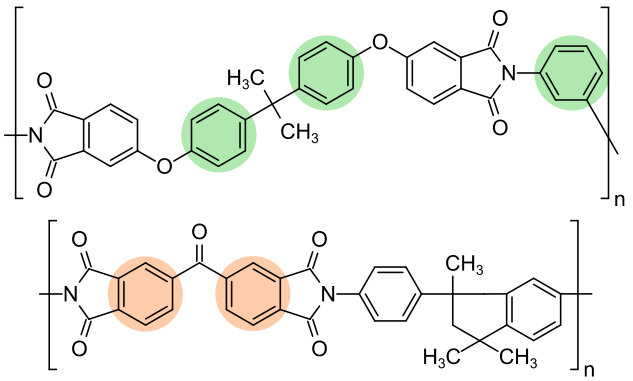

Figure 18: Schematic chemical structures of poly(ether imide) (PEI, top) and polyimide (PI, bottom). The relatively strong negatively charged phenyls in PEI and strong positively charged phenyl groups in PI are marked by green and orange, respectively.

Blend solutions were prepared by dissolving 200 mg of polyimide powder and poly(ether imide) pellets with a designed weight ratio in 10 mL of 1-methyl-2-pyrrolidinone (NMP, ≥99.5%, Sigma-Aldrich) and stirring at 200 rpm for 24 h at 70 °C, which yielded a clear and homogeneous solution. The solution was drop-casted (typically 2 mL for a 50 mm × 50 mm surface) onto a glass substrate (Corning Eagle XG), which was previously cleaned with Kemex A cleaning solution (Kemika) and deionized water, in an ultrasonic cleaner (Iskra PIO, 5 min) and finally in a UV-ozone cleaner (Ossila, 3 min). To remove the solvent, the solution was first kept in a drying oven at 80 °C for 12 h and then at 120 °C for 5 h, followed by annealing at 150 °C under vacuum for 24 h to further remove any residual solvent. The cast film was peeled off from the glass substrate after soaking in deionized water for up to 45 min, and the resulting free-standing film, with a typical thickness of about 10 μm, was then dried in a vacuum oven at 70 °C for 18 h [127]. The preparation procedure for poly(ether imide)/polyimide blend films is illustrated step by step in Figure 19.

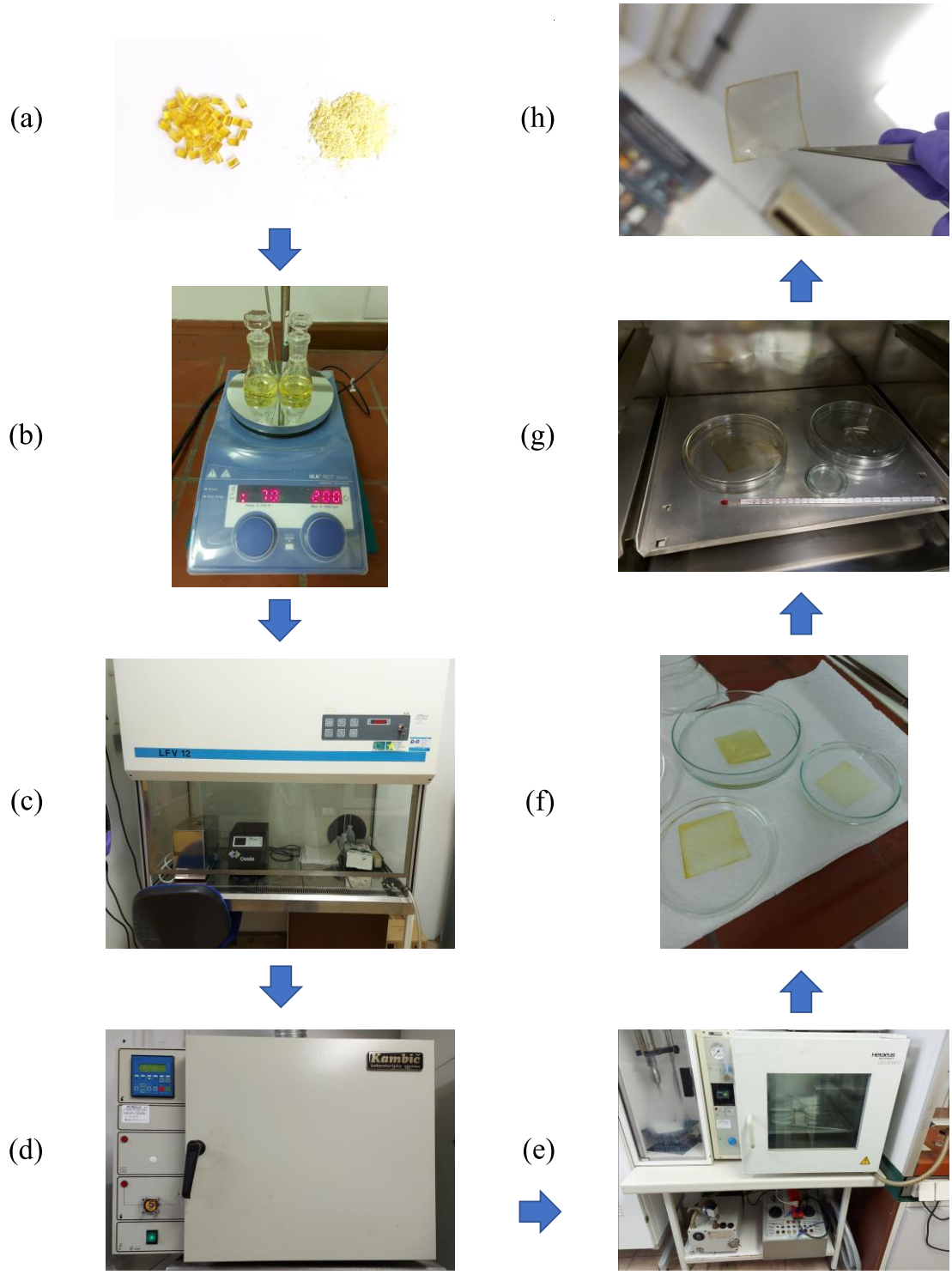

Figure 19: Preparation of PEI/PI blend films in sequential steps: (a) PEI pellets and PI powder; (b) stirring of PI powder and PEI pellets in NMP solvent for 24 h; (c) drop-casting the solution onto a clean glass substrate; (d) drying at 80 °C for 12 h and then at 120 °C for 5 h; (e) annealing under vacuum at 150 °C for 24 h; (f) soaking the cast films in deionized water; (g) drying the resulting free-standing films under vacuum at 70 °C for 18 h; (h) the final PEI/PI blend film.

Chapter 5

Experimental Techniques and Methods

In this chapter, different measurement techniques and methods used to investigate the dielectric response of cellulose/$Ti_3C_2T_x$ composites, poly(ether imide)/polyimide blends, and PNZST ceramics are presented.

The complex linear dielectric constant ($\varepsilon^*(\omega,T) = \varepsilon' - i\varepsilon''$) is a frequency- and temperature-dependent physical property of materials. Therefore, ε^* was analyzed over broad frequency and temperature ranges. The values of the real part of the complex dielectric constant, i.e., dielectric permittivity (ε'), and the values of the real part of the complex electrical conductivity, i.e., electrical conductivity (σ'), were calculated from the actual measured quantities: capacitance (C) and electrical resistance (R), using $\varepsilon' = Cd/\varepsilon_0 S$ and $\sigma' = d/RS$, where d is the sample thickness, S is the electrode area, and $\varepsilon_0 = 8.85 \times 10^{-12}$ A s V^{-1} m^{-1} is the permittivity of free space. The imaginary part of the dielectric constant ($\varepsilon''=$ is connected to the electrical conductivity via $\sigma' = 2\pi\nu\varepsilon_0\varepsilon''$.

5.1 Frequency-Dependent Measurements

Capacitance and electrical resistance of the samples were measured as a function of frequency at a constant temperature using either a Novocontrol Alpha High Resolution Dielectric Analyzer or an Agilent E4980A Precision LCR Meter under zero bias field. The amplitude of the probing AC electric signal was typically 1 V. The sample temperature was stabilized within ±0.01 K by using the lock-in bridge technique with a platinum resistor Pt100 as a thermometer. Measurements were performed in the frequency range from 1 Hz to 1 MHz.

5.2 Temperature-Dependent Measurements

For polymer samples, the temperature-dependent measurements were conducted at several frequencies (1 Hz–100 kHz) during heating or cooling runs with a Novocontrol Alpha High Resolution Dielectric Analyzer. The amplitude of the probing AC electric signal was 1 V. The temperature increased or decreased at a rate of 0.75 K min^{-1}. The sample temperature was controlled within ±0.01 K by using the lock-in bridge technique with a platinum resistor Pt100 as a thermometer. Measurements were performed in the temperature range between 125 and 400 K.

For the ceramic sample, the dielectric response was measured during a heating run with the probing AC signal of 1 V. The complex dielectric constant was measured with an Agilent E4980A Precision LCR Meter at a heating rate of 1 K min^{-1}. Measurements under various external DC bias electric fields were conducted using a standard external electrical circuit with two capacitors ($C_0 = 1$ μF) and a resistor ($R_0 = 10$ kΩ) (see Figure 20). The capacitors served as blocking capacitors to prevent the high DC voltage and current from damaging the Precision LCR Meter. The DC voltage was applied to samples by TREK 610C High Voltage Amplifier. To avoid any possible history-dependent effects, the sample was heated to 430 K for 15 min and then cooled under an external bias electric field to 240 K. The temperature was controlled with a Lake Shore Model 350 Cryogenic Temperature Controller that uses a platinum resistor Pt100 as a thermometer. Measurements were performed in the temperature range between 240 and 430 K.

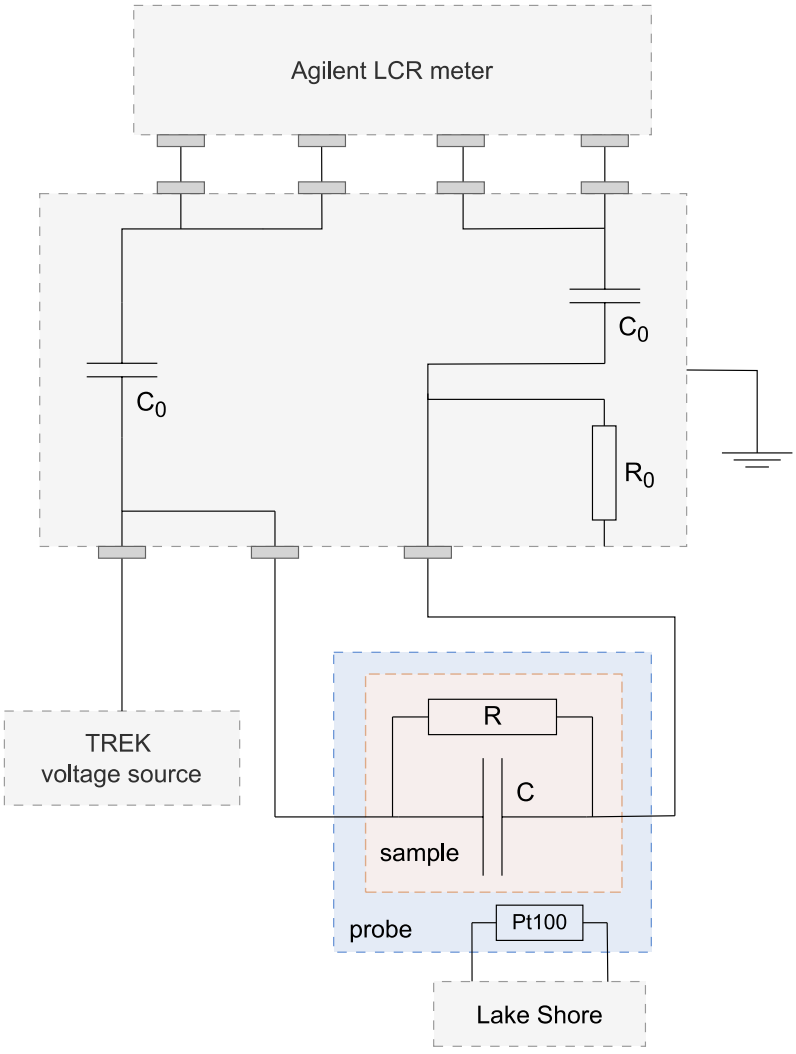

Figure 20: Schematic representation of the setup for temperature-dependent complex dielectric constant measurements. The sample is represented by an equivalent circuit of a leaky capacitor.

Polarization measurements were also performed under various external DC bias electric fields, applied using a TREK 610C High Voltage Amplifier. Prior to each measurement, the sample was heated to 430 K for 15 min and then cooled to 240 K under an external

bias electric field. Polarization data were obtained by measuring the voltage across a reference capacitor during a heating run at a rate of 2 K min^{-1} using a Keithley 6517B Electrometer. Since the reference capacitor was connected in series with the ceramic sample (see Figure 21), the charge on the reference capacitor was equal to the charge on the sample. Consequently, the sample polarization was calculated from the measured charge on the reference capacitor and the electrode surface area of the sample. Temperature control was achieved using a Lake Shore Model 350 Cryogenic Temperature Controller. Measurements were conducted in the temperature range from 300 to 430 K.

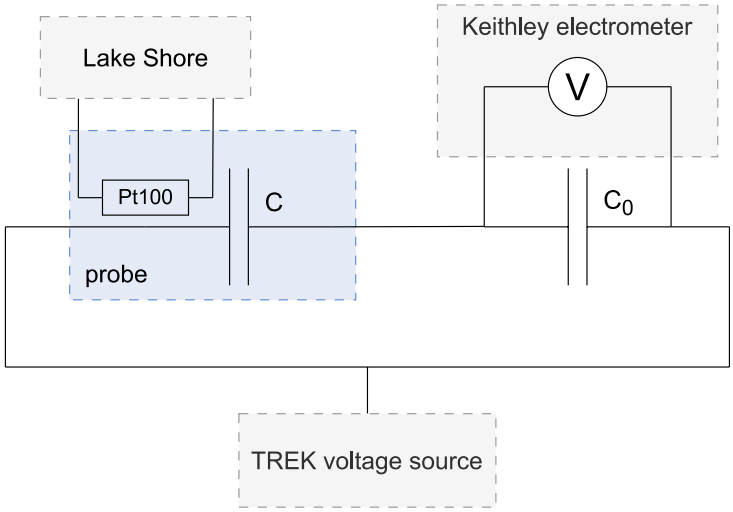

Figure 21: Schematic representation of the setup for temperature-dependent polarization measurements. C_0 is the capacitance of the reference capacitor and C is the capacitance of the sample.

The third harmonic of the dielectric response was obtained without an external DC bias field using a 20 V AC signal during a heating run from 200 to 410 K at a rate of 1 K min^{-1}. An HP35665A Dynamic Signal Analyzer was used to measure the voltage across a reference capacitor and analyze its frequency components using the Fast Fourier Transform algorithm. The real part of the third harmonic of the dielectric permittivity (ε_3') was determined from Eq. (10), i.e., a relationship derived from a Taylor series expansion of the polarization–electric field dependence:

$$\frac{P(E)}{\varepsilon_0} = (\varepsilon_1' - 1)E + \varepsilon_3' E^3 + \varepsilon_5' E^5 + \cdots \tag{9}$$

$$\varepsilon_3' = \frac{4C_0}{C_X} \cdot \frac{d^2}{(U_0 - U_1)^3} \cdot U_3 \tag{10}$$

where ε_1' ε_3', ε_5' are the first, third, and fifth harmonics of the dielectric permittivity, respectively. C_0 is the capacitance of the reference capacitor, C_X is the calculated capacitance of the sample based on its geometry, d is the sample thickness, U_0 is the amplitude of the probing AC signal, and U_1 and U_3 are the first and third harmonic voltage amplitudes, respectively.

5.3 Electric Field-Dependent Measurements

The complex dielectric constant as a function of the DC bias electric field, i.e., the dielectric tunability, was measured at various fixed temperatures using a probing signal of 1–20 V in 5 V steps, and at frequencies of 1 kHz and 10 kHz, with an Agilent E4980A Precision LCR Meter. A standard external electrical circuit, consisting of two blocking capacitors ($C_0 = 1\ \mu$F) and a resistor ($R_0 = 10\ \text{k}\Omega$), was used to prevent damage to the impedance analyzer by the high DC voltage and current (see Figure 22). The ceramic sample was heated to 430 K, then cooled and stabilized at the desired measurement temperature within ±2 mK by a Lake Shore Model 350 Cryogenic Temperature Controller, in order to avoid any possible history-dependent effects from previous measurements. During each measurement, the electric field was linearly cycled between ±35 kV cm^{-1} at a frequency of 1 mHz using an Agilent 33220A 20 MHz Function/Arbitrary Waveform Generator, and the generated voltage was amplified using a TREK 610C High Voltage Amplifier.

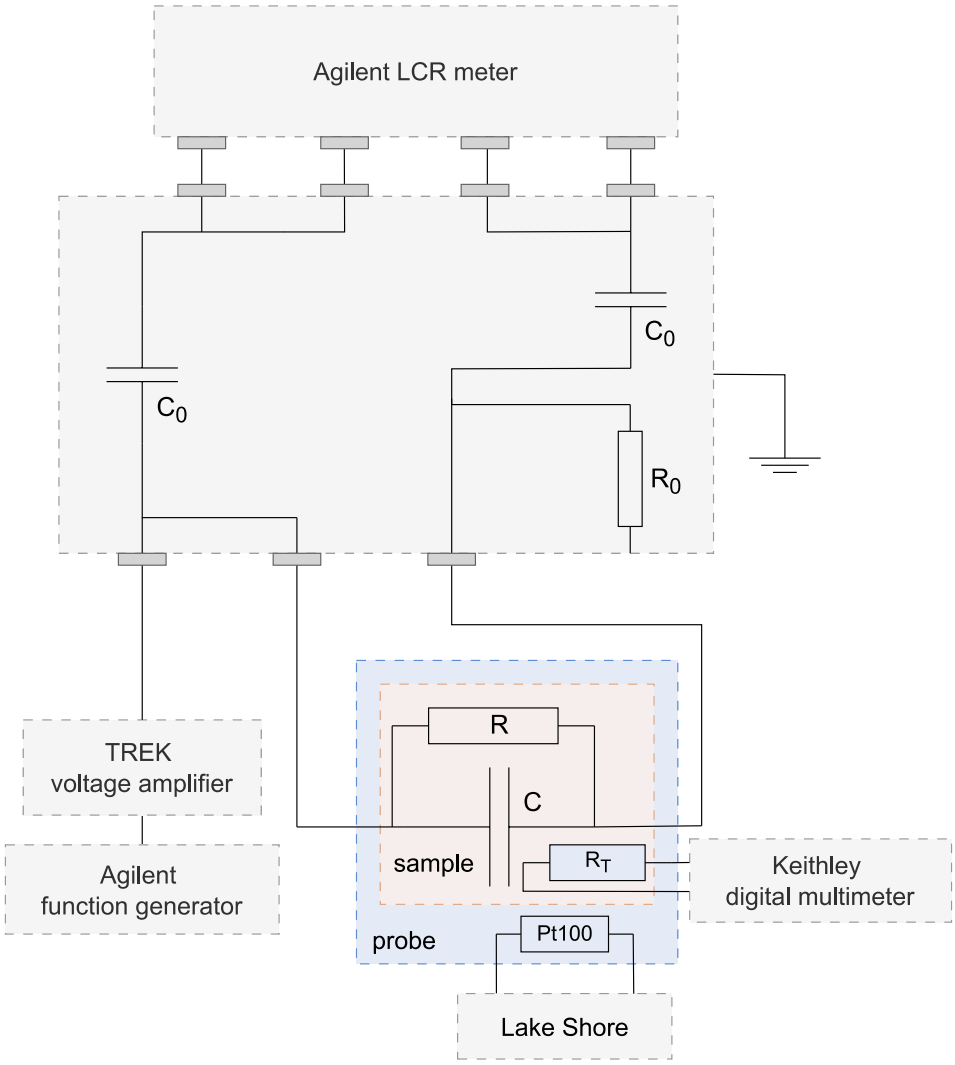

Figure 22: Schematic representation of the setup for electric field-dependent complex dielectric constant measurements. The sample is represented with an equivalent circuit of a leaky capacitor.

To determine the sample temperature, the resistance R_T of a 500 kΩ NTC thermistor, attached to the sample using diluted GE varnish, was measured simultaneously with a Keithley 2002 High Performance Digital Multimeter (see Figure 22). The sample temperature T was then calculated using the following equation:

$$\frac{1}{T} = a_0 + a_1 \log\frac{R_T}{1000} + a_2 \log^2\left(\frac{R_T}{1000}\right) + a_3 \log^3\left(\frac{R_T}{1000}\right) \tag{11}$$

where a_0, a_1, a_2, and a_3 are thermistor coefficients and R_T is the measured thermistor resistance.

Polarization was measured as a function of the DC electric field at various temperatures using a Keithley 6517B Electrometer. Prior to each measurement, the sample was heated to 430 K and then cooled to the measurement temperature and stabilized using a Lake Shore Model 350 Cryogenic Temperature Controller. The electric field was cycled between ±40 kV cm^{-1} at a frequency of 1 mHz using an Agilent 33220A 20 MHz Function/Arbitrary Waveform Generator. The generated voltage was amplified by a TREK 610C High Voltage Amplifier. Figure 21 shows a schematic representation of the experimental setup, excluding the function generator that preceded the voltage amplifier.

5.4 Rayleigh Measurements

Rayleigh measurements are typically performed by applying AC electric signals of increasing amplitude (below the coercive field of the sample) at a constant frequency, while measuring the dielectric response. By plotting the dielectric permittivity as a function of the electric field amplitude, the intrinsic (reversible) and extrinsic (irreversible) contributions to the dielectric response can be separated according to the Rayleigh law:

$$\varepsilon' = \varepsilon'_{int} + \alpha E_0 \tag{12}$$

where ε'_{int} is the intrinsic (reversible) Rayleigh coefficient, α is the irreversible Rayleigh coefficient, and E_0 is the amplitude of the AC electric field.

Due to experimental limitations, the maximum amplitude of the AC voltage was 20 V, corresponding to an electric field of 0.85 kV cm^{-1}. Therefore, to investigate the domain contribution, the ceramic sample was additionally exposed to different DC electric fields, onto which the AC field was superimposed and swept between 0.04–0.85 kV cm^{-1} at several temperatures. The AC voltage was applied at a frequency of 10 kHz and increased in 1 V steps, from 1 to 20 V, using an Agilent E4980A Precision LCR Meter. The external DC electric field was supplied by a TREK 610C High Voltage Amplifier. To eliminate history-dependent effects, the ceramic sample was heated to 430 K for 15 min and subsequently cooled under an external bias electric field to the measurement temperature, where it was stabilized using a Lake Shore Model 350 Cryogenic Temperature Controller. A schematic representation of the experimental setup is shown in Figure 20.

5.5 Time-Dependent Measurements

The dielectric permittivity was monitored over time at room temperature with a 1 V AC probing signal at a measurement frequency of 100 kHz, using a Novocontrol Alpha High Resolution Dielectric Analyzer.

5.6 DC Conductivity Measurements

DC conductivity measurements were conducted by applying a DC voltage to the sample in steps of 1 V, from 1 to 30 V, and measuring the electrical current through the sample using a Keithley 6517B Electrometer/High Resistance Meter. The sample was placed inside a metal box that served as both a safety and noise shield and was fixed between two metal plates. Figure 23 shows a schematic representation of the circuit used in the measurement setup. The electrical conductance $G = 1/R$ of the sample was determined using Ohm's law from the slope of the I–U curve in the linear regime. The electrical conductivity was then calculated based on the sample dimensions and the determined conductance in accordance with the relation $\sigma' = Gd/S$.

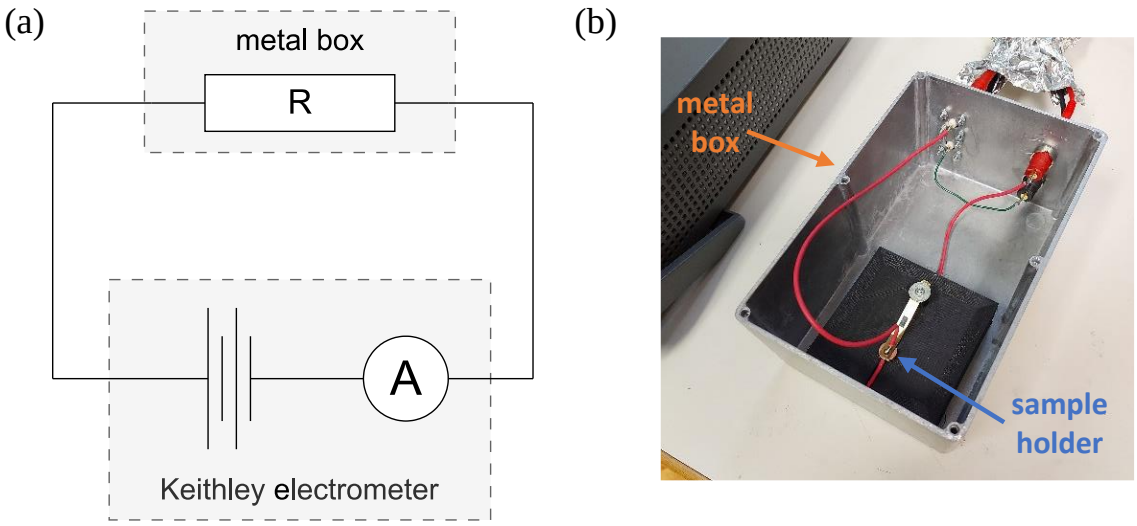

Figure 23: (a) Schematic representation of the DC conductivity measurement setup. R is the resistivity of the sample. (b) Position of the sample holder within the opened metal box of the custom-built DC conductivity measurement setup.

5.7 Dielectric Breakdown Strength Measurements

Dielectric breakdown strength measurements were conducted with a custom-built high-voltage setup. The DC voltage was applied to samples by a TREK 20/20C-HS High Voltage Amplifier with the rate of 100 V s^{-1}, while the linear-increasing signal was generated with a National Instruments data acquisition card and controlled by a LabVIEW program. Each sample, which was geometrically identical to those used for dielectric characterization, was fixed between the top and bottom half-sphere steel electrodes (see Figure 24). The breakdown event was identified when the current through the sample reached 20 mA. The dielectric breakdown strength was calculated according to the equation $E_b = V_{bd}/d$, where V_{bd} is the breakdown voltage and d is the sample thickness.

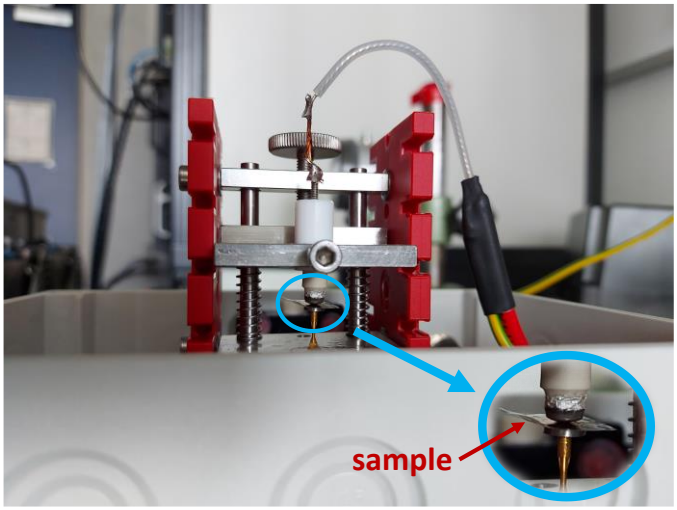

Figure 24: Placement of a polymer sample between two half-sphere steel electrodes in the custom-built high-voltage setup.

5.8 Piezoresponse Force Microscopy

The ceramic sample was investigated with an atomic force microscope (AFM; Molecular Force Probe 3D, Asylum Research, Santa Barbara, California, USA) equipped with a piezoresponse force microscopy (PFM) module. Images were acquired in dual AC resonance-tracking (DART) vertical mode. Before scanning, the sample was thinned to 45 μm to ensure good thermal equilibrium during the high-temperature PFM measurements. After that, the sample was polished on fabric using a polishing paste with a gradual decrease in the size of the diamond abrasive down to 0.25 μm, then fine-polished with a colloidal SiO_2 suspension, and finally cleaned with distilled water. For the PFM scanning, Pt-coated silicon tips with a radius of curvature ~10 nm (OMCL-AC240TM-R3, Olympus, Japan) were used. PFM measurements were performed at 333 K and 388 K using a custom-built high-temperature setup with a commercial heater (PolyHeater, Asylum Research, Santa Barbara, California, USA). Before each measurement, the sample was heated to 423 K for 10 min. First, an area of 20×20 μm was scanned using a DC tip voltage of 70 or 140 V. After that, a 35×35 μm scan was performed with a drive amplitude of 5 V, a frequency of 300 kHz, and a DC tip voltage of 0 V, followed by a few μm large scans of selected regions at similar voltage.

5.9 Scanning Electron Microscopy

SEM imaging of the cellulose/MXene composites was performed using a low-vacuum scanning electron microscope (FEI Quanta 200 3D, Thermo Fisher Scientific Inc., USA), equipped with an energy-dispersive X-ray spectrometer (Inca 350, Oxford Instruments Nanoanalysis, UK) for microchemical mapping. On the other hand, a Thermo Fisher Verios 4G HP scanning electron microscope equipped with an energy-dispersive X-ray spectrometer (Oxford Instruments, AZtec Live, Ultim Max SDD 65 mm^2, UK) was used to analyze the morphology and composition of the ceramic PNZST sample.

Chapter 6

Dielectric Investigations of Cellulose/MXene Composites

A composite approach as a method to enhance the dielectric response of a material is presented in this chapter. Conductive particles, dispersed in an insulating dielectric matrix, significantly increase the dielectric permittivity of the material near the percolation threshold. Here, cellulose nanofibrils (CNF) were used as the dielectric matrix and titanium carbide ($Ti_3C_2T_x$) sheets as the conductive filler. A dielectric investigation of these cellulose nanofibrils/$Ti_3C_2T_x$ composite films was conducted to determine the influence of the preparation method and the type of nanofibril matrix on the overall dielectric response and to verify whether the dielectric response follows the percolation theory, despite the unique shape of the conductive $Ti_3C_2T_x$ sheets.

A large portion of this chapter was originally published in V. Jurečič *et al., APL Mater.* (2024) 12(11): 111102.

6.1 Overview

With the aim of designing sustainable green electronics, considerable research has focused on cellulose as a base material for flexible electronics [14–18]. Although a percolative biopolymer made by incorporating functionalized graphene oxide into a cellulose-based matrix [19] showed promising results, a large-scale and cost-effective method for the synthesis of graphene-based systems is still missing, which limits their use in high-performance electronics [26].

Titanium carbide $Ti_3C_2T_x$ belongs to a class of novel 2D transition metal carbides, nitrides, and carbon nitrides known as MXenes. These systems (denoted as $M_{n+1}X_nT_x$, where M is an early transition metal, X is C and/or N, T is a hydroxyl, oxygen, or fluorine surface termination unit, and n=1–3) have attracted a considerable amount of attention due to their outstanding electrochemical properties, hydrophilicity, and metallic conductivity [27]. Furthermore, MXenes–particularly $Ti_3C_2T_x$–demonstrate even higher electrical conductivity than solution-processed graphene [28,128]. Therefore, a strong increase in the dielectric response due to a large Maxwell–Wagner interfacial polarization is expected near the percolation threshold.

6.2 General Dielectric Response

For dielectric measurements, surfaces of films were covered by ≈100 nm thick sputtered gold electrodes with a diameter of 4 mm. Figure 25 shows the frequency dependence of the dielectric permittivity and electrical conductivity, measured at room temperature in a pristine CNF film using a Novocontrol Alpha Analyzer. The absorbed water strongly enhances the values of both ε' and σ' at low frequencies in the as-prepared sample (note the logarithmic ε'-scale). While free absorbed water requires low energy to be removed, water molecules can also be trapped in the fiber network [129] or bound to the hydroxyl groups on the surface of cellulose. Trapped and bound water can be removed under specific drying conditions to overcome capillary forces and other interactions. After drying the sample, ε' and σ' values at low frequencies decrease by orders of magnitude but increase again when the sample is exposed to air moisture. A similar behavior was detected in the composite sample with 5 wt% $Ti_3C_2T_x$ MXene (denoted as CNF-5MX in Figure 25, both samples were prepared by vacuum filtration). It can be seen that the low-frequency ε' values of the as-prepared samples are significantly lower in the composite. MXene sheets not only reduce the space for trapped water within the fibril network but also decrease the amount of bound water due to CNF–$Ti_3C_2T_x$ interactions. To minimize the influence of air moisture on the dielectric results, the films were dried at 375 K for 1 hour prior to all following dielectric measurements.

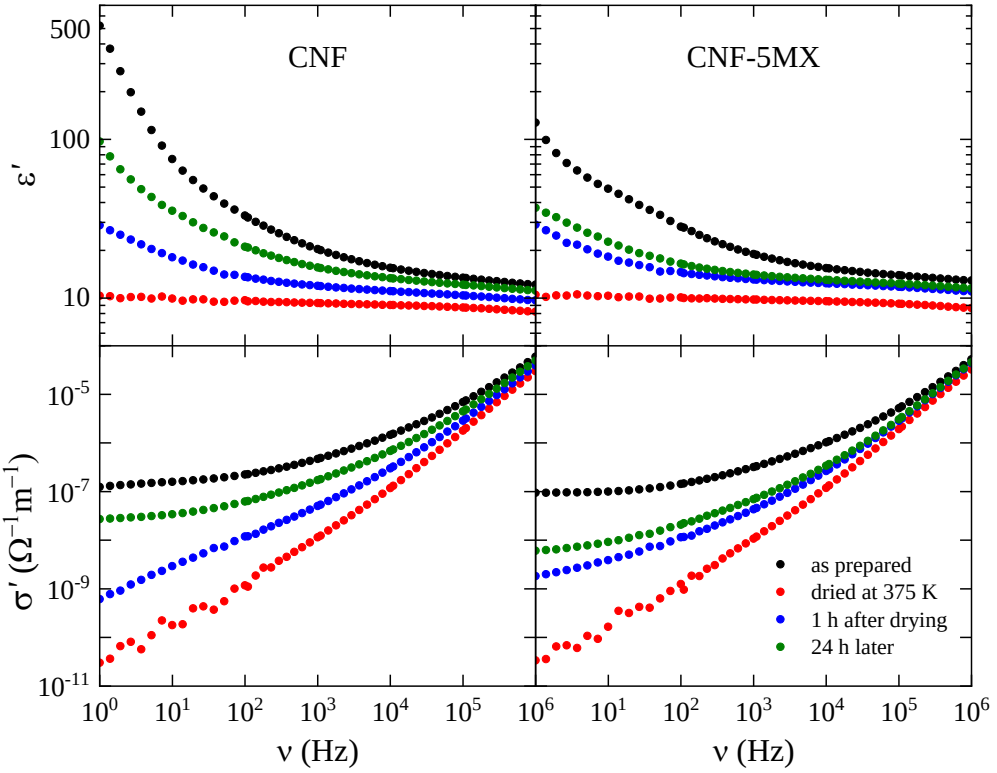

Figure 25: Frequency dependence of the dielectric permittivity and electrical conductivity of the pristine CNF sample (left) and the CNF-5MX composite (right), measured at room temperature: (i) in the as-prepared film, (ii) after drying at 375 K, (iii) 1 hour after drying, and (iv) 24 hours later.

6.2.1 Influence of the preparation method on the dielectric response

To compare the influence of $Ti_3C_2T_x$ MXene on the dielectric properties of different cellulose films, the dielectric response of composite samples prepared with 5 wt% $Ti_3C_2T_x$ was first investigated. Figure 26 shows the temperature dependence of the dielectric permittivity and electrical conductivity of vacuum-filtered CNF-based, solvent-casted CNF-based, and solvent-casted TCNF-based composite films (a high-water retention ability of TCNF prevents it from being vacuum filtered). The temperature-dependent dielectric response was measured at several frequencies from 1 Hz to 100 kHz during a cooling run from 375 to 150 K at a rate of ± 0.75 K min^{-1} using a Novocontrol Alpha Analyzer. While the intrinsic data at the highest frequencies are almost identical, the increase in both ε' and σ' at low frequencies and high temperatures is much more pronounced in the solvent-casted than in the vacuum-filtered CNF-5MX sample. This suggests that solvent-casted samples contain a higher amount of free space charges or other impurities than vacuum-filtered ones. Since these charges increase dielectric losses and imply the dielectric breakdown at lower electric fields, the dielectric response of vacuum-filtered CNF/$Ti_3C_2T_x$ composite films was thoroughly analyzed. The number of space charges is the highest in the TCNF-based sample–this is not surprising, as a high number of hydroxyl groups on the surface of CNF are replaced by highly hydrophilic and polar carboxylate groups after TEMPO-mediated oxidation of cellulose [115,117].

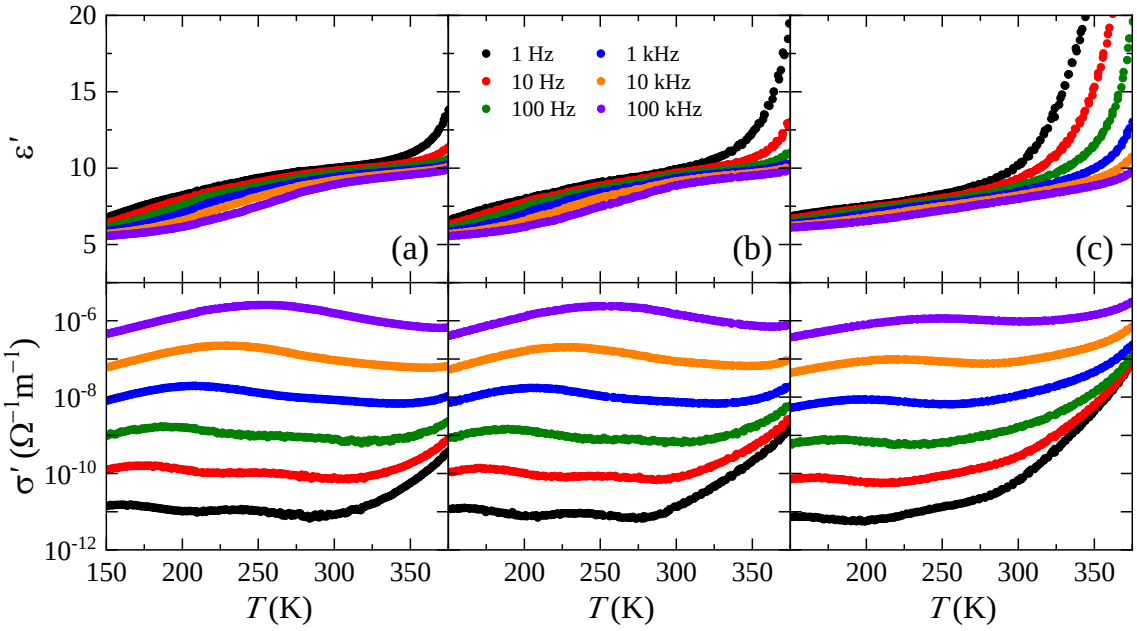

Figure 26: Dielectric response detected during cooling runs after various composite samples with 5 wt% $Ti_3C_2T_x$ were heated to 375 K: (a) the vacuum-filtered CNF-5MX, (b) the solvent-casted CNF-5MX, (c) the solvent-casted TCNF-5MX.

The dielectric spectra in Figure 26 also reveal a relaxation behavior between 150 and 300 K, particularly in both CNF-based composites. It is known that amorphous cellulose exhibits two secondary relaxations, the so-called γ and β relaxations, at temperatures below its glass transition temperature. The activation energy of the γ relaxation, along with comparisons to other polysaccharides, leads to the conclusion that it corresponds to the noncooperative rotation of CH_2OH lateral groups [130]. On the other hand, β relaxation

is characterized by high values of the activation parameters, suggesting that this dissipation process originates from cooperative but localized motions of segments of the main chain [131]. The dielectric relaxation strength of the γ relaxation is typically much higher than that of the β relaxation; however, it is difficult to distinguish the heavily overlapping relaxation signals, as both occur in the temperature range of 150–300 K.

6.2.2 Influence of absorbed water

To investigate the impact of moisture and $Ti_3C_2T_x$ MXenes on the relaxation behavior of cellulose, we have performed temperature-dependent measurements, as presented in Figure 27. The main frame shows the dielectric response of the as-prepared (undried) CNF-10MX composite, detected at several frequencies during a cooling run from room temperature to 125 K, a subsequent heating run to 375 K, and a final cooling run to 125 K, at a rate of ± 0.75 K min^{-1}. It can be seen that the relaxation intensity is much lower during the second cooling run, after the sample has been heated to a high temperature, i.e., dried. This suggests that, similar to many other polymer systems [132–134], these molecular motions–particularly those associated with γ relaxation–involve water molecules that are absorbed into the free volume of the system and attached to cellulose polar groups via weak physical or stronger hydrogen bonds.

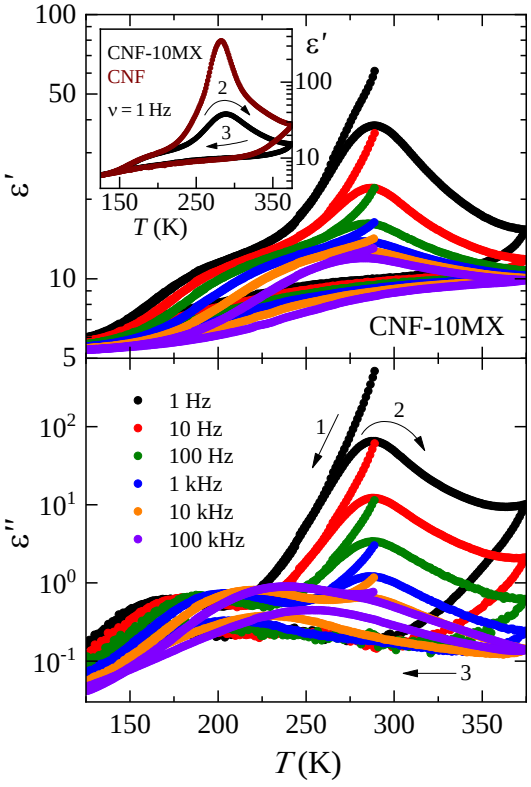

Figure 27: Dielectric response of the vacuum-filtered CNF-10MX composite, detected at several frequencies during (1) a cooling run from room temperature to 125 K, (2) a subsequent heating run to 375 K, and (3) a final cooling run to 125 K (indicated by arrows). The inset shows a comparison of the dielectric permittivity of this composite with that of the pristine vacuum-filtered CNF sample at the lowest measurement frequency of 1 Hz during the second (125–375 K) and third (375–125 K) temperature runs.

The inset of Figure 27 compares the response of the CNF-10MX composite with that of the pristine CNF sample at the lowest measurement frequency of 1 Hz during the second and third temperature runs. It can be seen that 10 wt% $Ti_3C_2T_x$ has a negligible influence on the cellulose relaxation behavior; however, as already shown in Figure 25, the influence of moisture is much more pronounced in the pristine CNF.

6.3 Percolative Behavior

The frequency dependence of the room-temperature dielectric response in the vacuum-filtered CNF/$Ti_3C_2T_x$ composite films with various $Ti_3C_2T_x$ content is shown in Figure 28a. While the electrical conductivity increases at higher frequencies, the values at lower frequencies tend toward the DC conductivity plateau. This behavior corresponds to an equivalent circuit composed of two R–C circuits connected in series. The resistivity of the low-frequency plateau is then $R_1 + R_2$ (R_1 and R_2 are resistivities of titanium carbide and CNF, respectively), while at higher frequencies the conductivity follows a ν^2 law if $R_2 \gg R_1$ [102], as is evidently the case in a percolative composite (then the value of the low-frequency plateau is just the resistivity of the CNF matrix). Concomitantly, the frequency dependence of the effective capacity of such an equivalent circuit would obey a Debye-like behavior from C_1 at low to C_2 at high frequencies if $C_1 \gg C_2$. Aside from modeling the spectra by an equivalent circuit with frequency-independent elements, the detected dielectric response can also be qualitatively understood in physical terms. While at lower frequencies the conductivity of the $Ti_3C_2T_x$ inclusions is effectively blocked, at sufficiently high frequencies their higher conductivity is revealed, as most of the charge carriers have no time to feel the blocking boundaries. Therefore, the effective AC conductivity (σ') increases with frequency and would continue to increase up to the high-frequency plateau corresponding to the value of the MXene's conductivity. As the Kramers–Kronig relations must be satisfied even for an inhomogeneous system, the increasing σ' parts of the spectra contribute to the static dielectric permittivity through a strong dielectric relaxation. It should be stressed that composite films with 75, 80, and 90 wt% $Ti_3C_2T_x$ are evidently above the percolation threshold; thus, their high electrical conductivity prevents the determination of the dielectric permittivity. Finally, the measured sample forms an electrical circuit with the resistance and, eventually, the inductance of the measuring setup, resulting in a resonant-like behavior of the detected response. Such behavior usually occurs at frequencies far beyond the measurement range ($\approx$ 10 GHz); however, in samples close to the percolation threshold, the capacitance is so high that it can already influence the data at the highest measurement frequencies.

CNF/$Ti_3C_2T_x$ composite films do not represent an ideal percolative composite with randomly distributed small-scale metallic regions within a dielectric matrix. Figure 29 shows cross-sectional SEM images of a vacuum-filtered pristine cellulose nanofibrils film and a CNF-10MX composite film. The morphology of the CNF/$Ti_3C_2T_x$ composite films differs significantly from that of an ideal percolative composite (see Figure 14). Here, the high electrical conductivity filler $Ti_3C_2T_x$ is in the form of relatively large 2D sheets, which, in addition to electrostatic interactions with the matrix, also form hydrogen bonds with hydroxyl and carboxyl surface groups on the CNF. Nevertheless, the dielectric permittivity strongly increases with increasing $Ti_3C_2T_x$ content. Figure 28b depicts the ε' values, measured at the highest frequency (1 MHz), where the contribution of free space charges or extrinsic effects, such as the presence of surface layers, is the lowest [135]. The inset to Figure 28b shows a zoomed-in view of the ε' data from Figure 28a for samples with the lowest $Ti_3C_2T_x$ contents (1, 2, 5, and 10 wt%) in the high-frequency region. The

experimental data shown in Figure 28c were collected at the lowest measurement frequency of 1 Hz, since they are closest to the intrinsic DC conductivity of the material. While these data already appear to follow the theoretical predictions of Eqs. (6) and (7), additional measurements were performed to determine the DC conductivity of samples that had not yet reached the DC conductivity plateau at 1 Hz, i.e., those with the lowest $Ti_3C_2T_x$ contents (1, 2, 5, and 10 wt%).

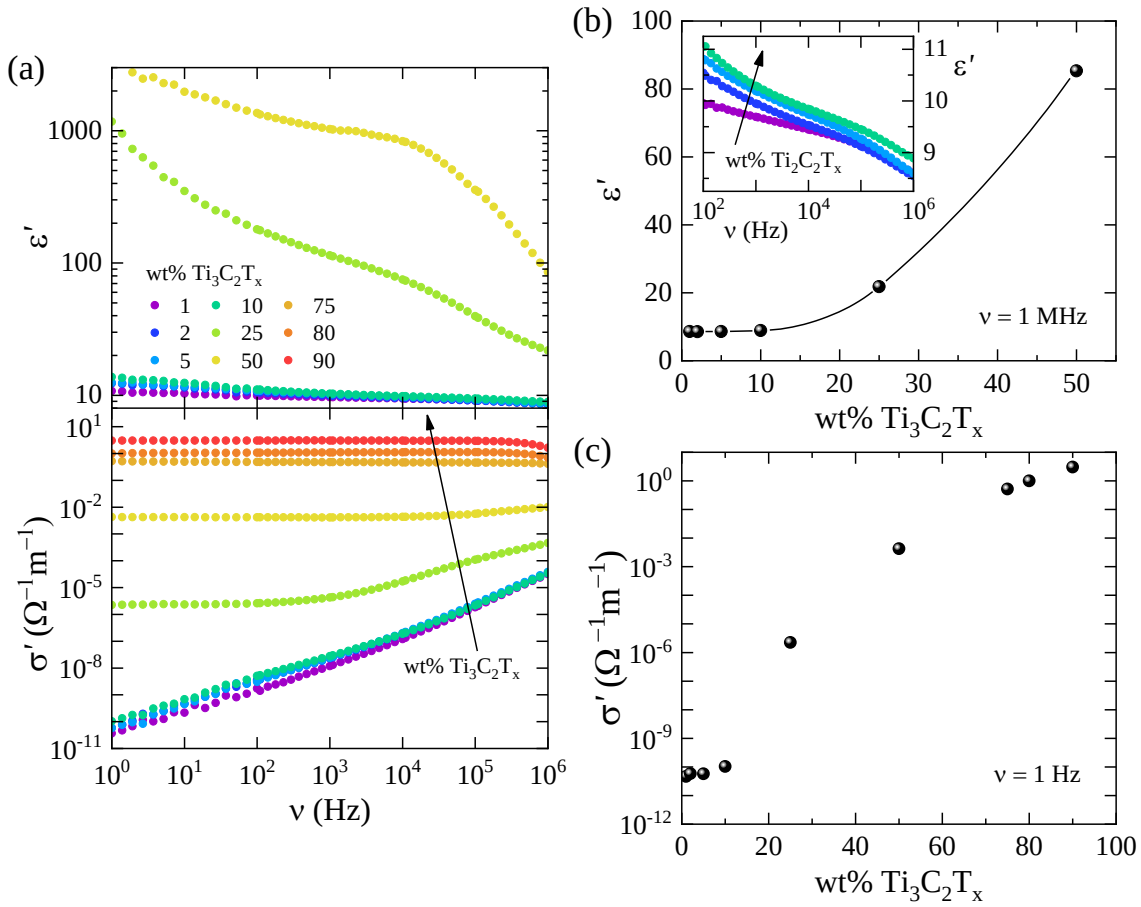

Figure 28: (a) Frequency dependence of the dielectric permittivity and electrical conductivity, detected at room temperature in the vacuum-filtered CNF/$Ti_3C_2T_x$ composite films with various $Ti_3C_2T_x$ contents. (b) Room temperature dielectric permittivity of the composite films at the highest measurement frequency of 1 MHz as a function of $Ti_3C_2T_x$ content. The solid line is a guide to the eye. The inset zooms in on ε' data from (a) for samples with the lowest $Ti_3C_2T_x$ contents (1, 2, 5, and 10 wt%) in the high-frequency range. (c) Electrical conductivity of the CNF/$Ti_3C_2T_x$ composite films as a function of $Ti_3C_2T_x$ content. Data were collected from (a) at the lowest measurement frequency of 1 Hz.

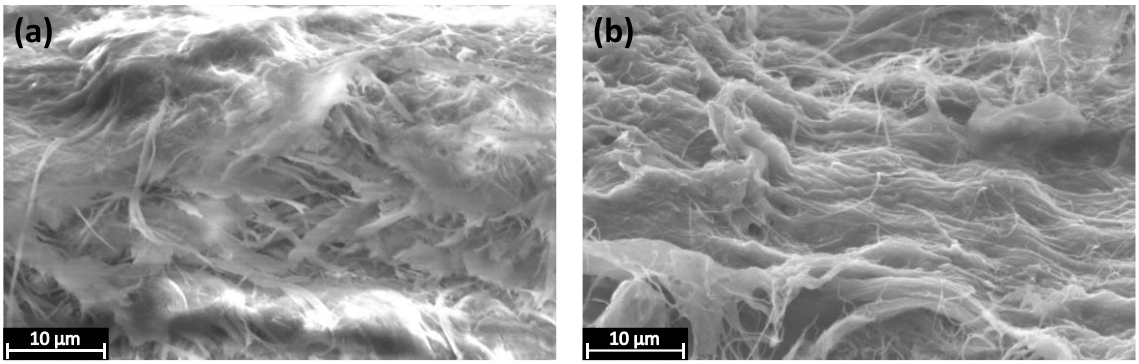

Figure 29: Cross-sectional SEM images of vacuum-filtered (a) the pristine cellulose nanofibrils film and (b) the CNF/MXene composite film with 10 wt% $Ti_3C_2T_x$.

Figure 30a shows data collected on dry and wet samples during the DC conductivity measurements. The wet samples were inserted directly into the setup, while the dry samples were placed in a drying oven for 1 h at 375 K beforehand. As previously discussed, the influence of absorbed water is evident: the measured current through the wet samples is five orders of magnitude higher than in the previously dried samples. It can be seen that the amount of $Ti_3C_2T_x$ increases the measured current through the sample. Moreover, the slope of the I–U curve indicates the electrical conductance of the sample, which was determined from the solid lines in Figure 30b. The electrical conductivity was then calculated based on the sample dimensions and the determined conductance. The DC conductivity values obtained for samples with the lowest $Ti_3C_2T_x$ contents (1, 2, 5, and 10 wt%) using this experimental technique are two orders of magnitude lower than those shown in Figure 28c. Figure 30c, therefore, presents the electrical conductivity of CNF/$Ti_3C_2T_x$ composite films as a function of the $Ti_3C_2T_x$ content, including the corrected data for samples with the lowest $Ti_3C_2T_x$ content (1, 2, 5, and 10 wt%), which reasonably well follow the predictions of the percolation theory (see inset).

As is typical for all percolative systems [105–107], the strong conductivity increase near the percolation point also increases the dielectric losses ($\tan\delta$). While in samples with up to 10 wt% $Ti_3C_2T_x$ content $\tan\delta$ remains nearly constant (≈0.07), it increases to 0.4 and 2.1 in composites with 25 and 50 wt% $Ti_3C_2T_x$, respectively. Despite this, the developed composites still show application potential, particularly in the field of flexible piezoelectric materials. Cellulose nanofibril films, namely, exhibit a promising piezoelectric response [136]. Moreover, since the electric energy ($U_e = \frac{1}{2}\varepsilon_0\varepsilon' E^2$) that can be converted into strain energy during electromechanical operation is directly proportional to the dielectric permittivity, an increase in ε' can enhance the piezoelectric response or, alternatively, induce the desired strain under a much reduced electric field.

Broadband dielectric spectroscopy also enables the separation of dielectric contributions from individual constituents in both organic and inorganic composite systems. This was thoroughly demonstrated by A. Eršte in her doctoral dissertation [137], whereas the focus of this work is on experimentally obtaining an enhanced dielectric response in different novel materials. Since the composite approach invariably leads to increased losses according to the Kramers–Kronig relations, the following chapter introduces an alternative strategy aimed at enhancing the electric energy density without increasing dielectric losses.

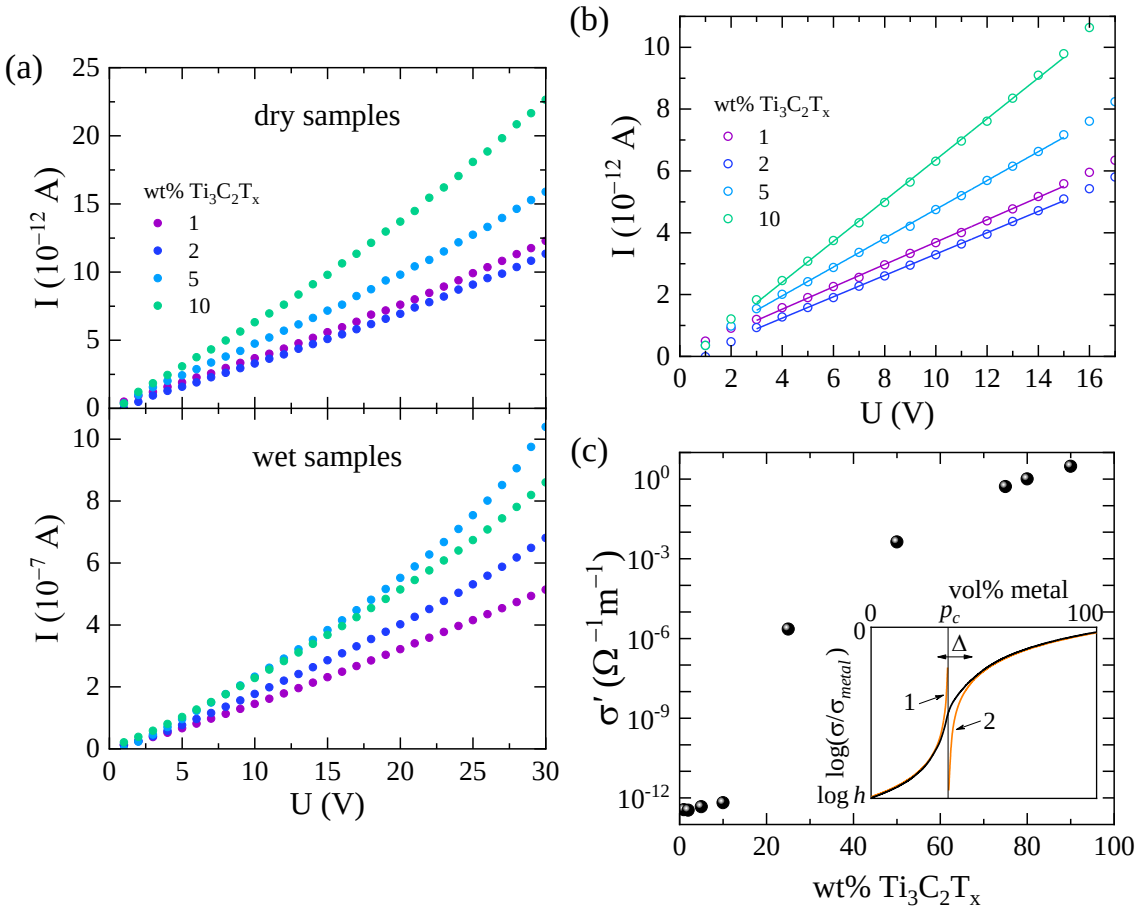

Figure 30: (a) Current as a function of applied DC voltage measured at room temperature for samples with the lowest $Ti_3C_2T_x$ contents before (wet) and after drying (dry). (b) Fits to the *I–U* curves of dry samples, represented by solid lines in the linear regime below 15 V. (c) Electrical conductivity of CNF/$Ti_3C_2T_x$ composite films as a function of the $Ti_3C_2T_x$ content. Data for samples with the lowest $Ti_3C_2T_x$ content (1, 2, 5, and 10 wt%) from Figure 28c were corrected based on the results from (b). The inset shows the theoretical dependence of the effective electrical conductivity for a system consisting of randomly distributed metallic and dielectric regions ($h = \sigma_{diel}/\sigma_{metal} \ll 1$). A smooth transition between the behaviors described by Eqs. (6) and (7) (orange lines) occurs within a small interval Δ near the percolation threshold (p_c).

Chapter 7

Poly(ether imide)/Polyimide Blend Systems

In this chapter, an alternative approach to enhance the dielectric response is presented. Unlike the composite approach, which simultaneously increases both the real and imaginary parts of the complex dielectric constant, this approach focuses on achieving high electric energy density by operating under high electric fields. It has already been demonstrated that blends of polymers that contain phenyl groups can withstand much higher electric fields than pristine systems [12]. However, the origin of this enhanced dielectric breakdown strength has not yet been investigated.

The aim of this chapter is to investigate the origin of the enhanced dielectric breakdown strength through extensive dielectric measurements of poly(ether imide)/polyimide blend systems. The contents of this chapter were published in V. Jurečič *et al.*, *Macromolecules* (2023) 56(3): 1097–1104.

7.1 Overview

Polymer-film capacitors are very attractive for high-temperature and high-power applications because they are inexpensive, can be produced in a variety of shapes, and exhibit both high dielectric breakdown strength and low dielectric losses. However, one of the major challenges in developing dielectric polymers is realizing high electric energy density while maintaining low dielectric losses, even at very high applied electric fields [120].

The electric energy density is only linearly proportional to the dielectric permittivity, while its maximum value depends quadratically on the dielectric breakdown strength (E_b) following $U_e \propto \varepsilon' {E_b}^2$. Classical models suggest that the intrinsic breakdown strength of dielectric polymers exceeds 1 GV m^{-1} because of their large energy bandgap and small mean free path for mobile charges [121]. However, experimentally measured E_b values in many widely used polymers are significantly lower than theoretically predicted intrinsic values due to imperfect chain packing (usually coiled and entangled chains), which results in weak points such as free volume and structural disorder [121–123].

Phenyl groups are fundamental chain components of many high-temperature polymers, and, depending on the polymer's molecular structure, delocalized electrons in these groups may exhibit a partially positive or negative charge. Blending appropriately matched polymers can thus result in strong interchain electrostatic interaction between chains of different polymers, leading to systems with high chain packing density and a reduction in

not only weak points but also, just as importantly, in the amount of accumulated space charge. These charges at weak points gain higher energies when accelerated by an applied electric field and, consequently, initiate breakdown at lower electric fields. Blending of polymers is thus a highly scalable strategy that has already been used to improve their dielectric, mechanical, and thermal properties [138–141].

Poly(ether imide) (PEI) and polyimide (PI) are high-temperature polymers with similar dielectric permittivities and contain oppositely charged phenyl groups. Therefore, blending these two polymers should not increase the real and imaginary parts of the complex dielectric constant. However, due to the presence of two strong positively charged phenyl groups in PI and three relatively strong negatively charged phenyl groups in PEI (see Figure 18), space charges may accumulate in both systems. In blends, strong electrostatic interactions between phenyl groups of different polymer chains may not only lead to higher chain packing density and, concomitantly, to reducing the free volume and structural disorder, but they could also reduce the number of accumulated space charges in the system, and thus enhance the dielectric breakdown strength of PEI/PI blends. The results of dielectric measurements in the following sections will determine whether this deduction is correct.

7.2 General Dielectric Characterization

The general dielectric response was measured for seven different polymer films: pristine PEI, pristine PI, and five PEI/xPI blends, where x denotes the weight percentage of PI. For dielectric measurements, surfaces of films were covered by ≈100 nm thick sputtered gold electrodes having a diameter of 6 mm. Figure 31 shows the frequency dependence of the dielectric permittivity (ε') and electrical conductivity (σ') of PEI, PI, and the PEI/50PI blend, detected in the frequency range of 500 Hz–500 kHz by an Agilent E4980A Precision LCR meter. All samples were first heated to 360 K, and the frequency-dependent response was measured after the temperature was stabilized at designated values, decreasing in steps of 20 K. It can be seen that the dielectric response is almost independent of temperature in the range of 360–160 K for all three samples.

Similar results were obtained for all other blends, and their dielectric responses at 300 K are collected in Figure 32a. The intrinsic responses of all samples at 110 kHz and 300 K are summarized in Figure 32b. It can be seen that both the electrical conductivity and dielectric permittivity of the blend samples are lower than those of pristine PEI and PI, particularly in the PEI/50PI and PEI/80PI blends. An identical dependence on the PI content was detected at all measured temperatures (see the inset in Figure 32b). Notably, changes in the dielectric permittivity are minor (a 5 % decrease in the PEI/80PI blend compared to the pristine polymers), while the electrical conductivity in the same blend is almost 40 % lower than in PEI and PI.

The observed changes in the intrinsic dielectric response (110 kHz, Figure 32b) cannot account for the enhancement of the dielectric breakdown strength. To check the number of space charges in various samples, additional measurements were conducted.

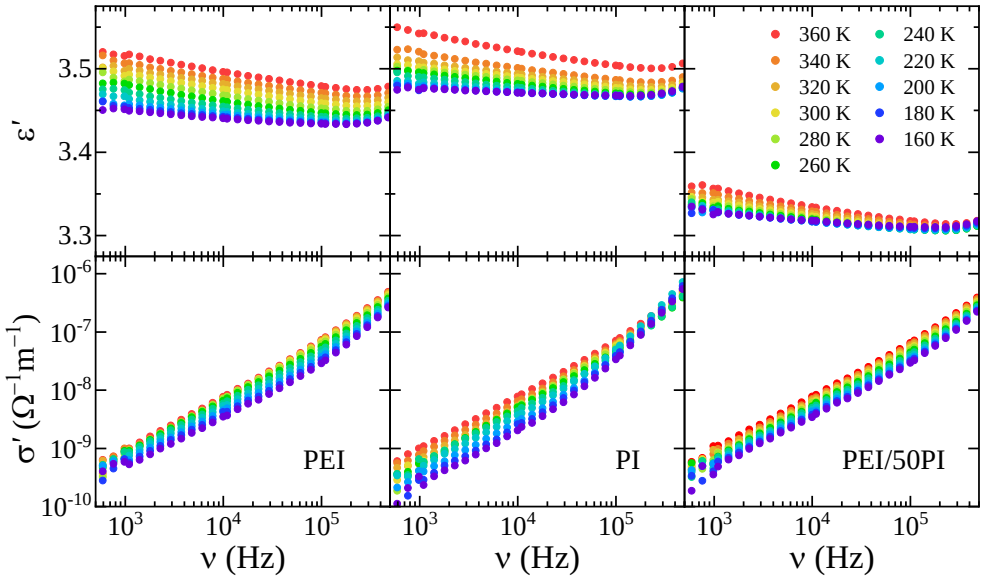

Figure 31: Frequency dependence of the dielectric permittivity (ε') and electrical conductivity (σ') of PEI, PI, and the PEI/50PI blend measured at various temperatures from 360 K down to 160 K.

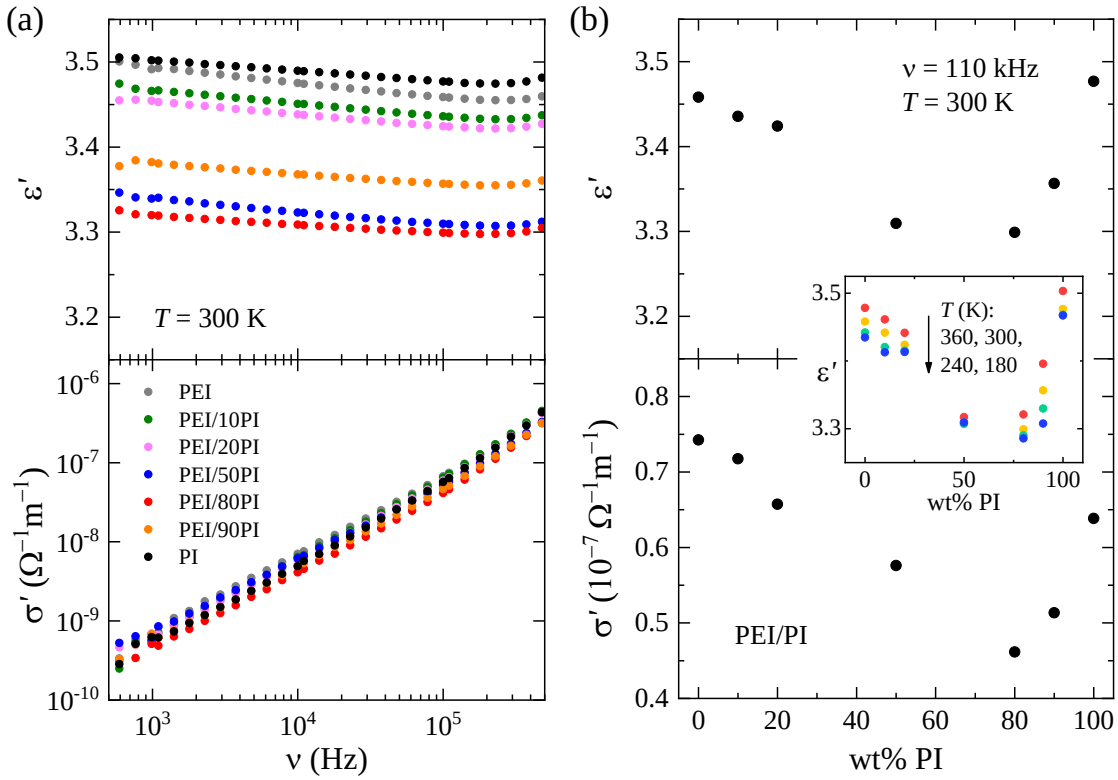

Figure 32: (a) Frequency-dependent dielectric permittivity and electrical conductivity detected at 300 K in PEI, PI, and various PEI/PI blends after annealing at 360 K. (b) Room-temperature ε' and σ' of annealed PEI/PI blends. The inset shows that the dependence on the PI content is identical over the temperature range of 360–180 K.

7.3 Low-Frequency Dielectric Response

To determine the presence and influence of space charges in the samples, low-frequency dielectric measurements were performed using a Novocontrol Alpha Analyzer, since space charges predominantly dictate the response at low frequencies. Figure 33a shows a typical measurement run of dielectric permittivity and electrical conductivity measurement run, performed at several frequencies in the range from 1 Hz to 100 kHz during (i) a heating run from room temperature to 400 K and (ii) a subsequent cooling run down to 250 K with the rate of ± 0.75 K min^{-1}. It should be stressed once again that all data in Figure 31 and Figure 32 were collected during cooling runs, i.e., the samples were first heated up to 360 K, and the frequency spectra were then recorded on cooling in steps of 20 K. Here, the measurement of the samples, previously exposed to normal air atmosphere conditions, started at room temperature. A decrease is seen in the dielectric permittivity at the beginning of the heating run, while the increase of ε' above 350 K is mainly due to the charges accumulated in the sample, which influence the dielectric response, particularly at low frequencies.

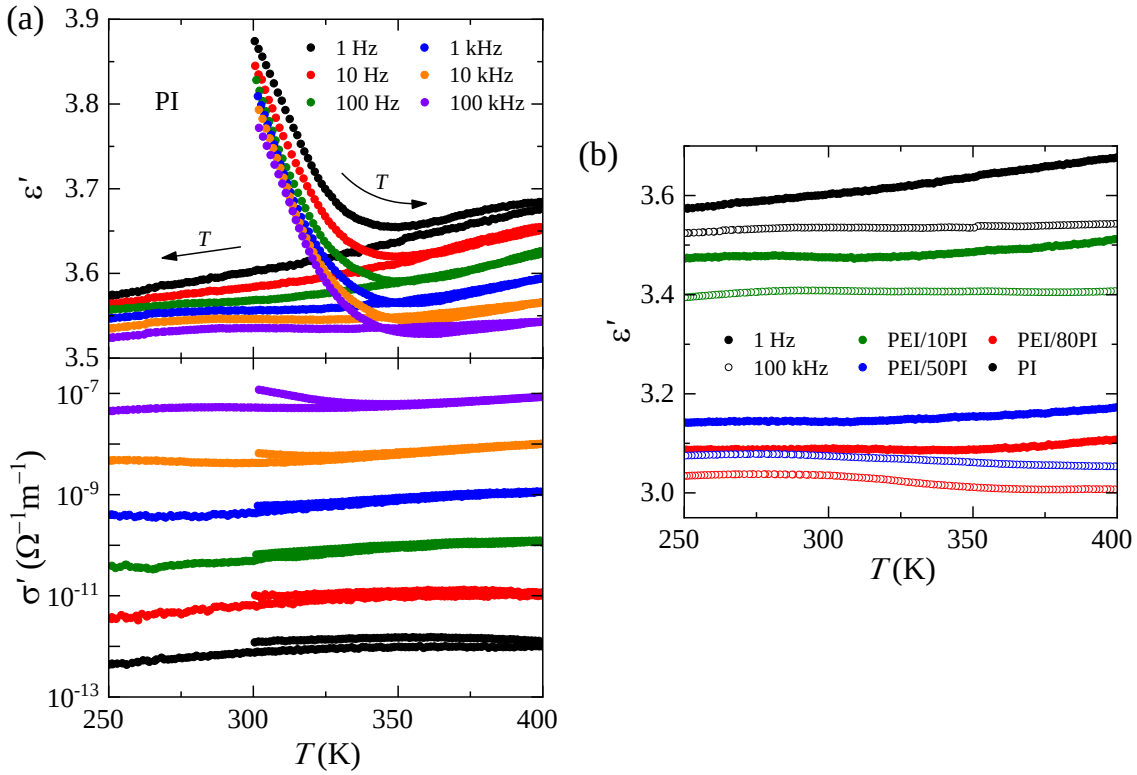

Figure 33: (a) Dielectric permittivity and electrical conductivity of PI, detected at several frequencies during heating from room temperature to 400 K and a subsequent cooling run to 250 K (indicated by arrows). (b) Dielectric permittivity measured at 1 Hz and 100 kHz in various PEI/PI blends during a cooling run from 400 to 250 K. At 1 Hz, the increase toward higher temperatures is much higher in the pristine PI than in the blend samples.

Figure 33b summarizes the dielectric permittivity of four samples at the lowest and highest measurement frequencies, collected during cooling runs from 400 to 250 K, which followed heating runs from room temperature to 400 K. While data at 100 kHz for the PEI/50PI and PEI/80PI blends are almost temperature-independent, there is still a slight

increase toward higher temperatures in the pristine PI and PEI/10PI blend. On the other hand, data at 1 Hz, where space charge contributions are most pronounced, increase toward higher temperatures in all samples; yet the increase is much higher in the PEI/10PI blend and, particularly, in the pristine PI. These results thus already indicate a lower amount of accumulated space charge in the blends in comparison to pristine polymers.

7.4 Aging of the Dielectric Permittivity

To determine whether an aging mechanism contributes to the decrease in dielectric permittivity of PEI/PI blends, the samples were exposed to a probing AC electric signal of 1 V for several hours. The term aging itself is not well-defined; it is usually used to describe the changes in properties occurring during a broad range of experimental conditions, but in the most basic sense, it indicates the time-dependent change of physical and/or electrical properties [142].

Figure 34 shows a decrease in dielectric permittivity with time when the measuring AC electric field (frequency of 100 kHz) is applied at room temperature conditions. Various mechanisms exist that explain dielectric aging, particularly in ferroelectric materials [142,143]. In dielectric polymers, however, the most plausible mechanism is the drift of free charge carriers: even under a small AC electric field, these charges are forced to migrate toward sample surfaces, where they screen the electrical polarization and thereby decrease the dielectric permittivity over time. Nevertheless, as can be seen in Figure 34, aging processes in PEI, PI, and PEI/PI blends are stochastic and change the dielectric response by <1.5 %. Therefore, the decrease in the data at the beginning of the measurement run in Figure 33a (heating the PI sample from room temperature) is not due to dielectric aging but mainly the result of water evaporation. The effects of moisture, i.e., water absorption and evaporation, on the physical properties of polyimide-based systems are well known [144–146] and will be discussed in detail in the next section.

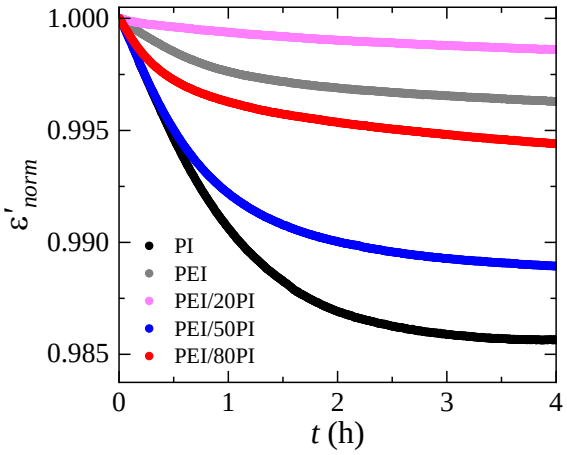

Figure 34: Time dependence of the normalized permittivity ($\varepsilon'_{norm} = \varepsilon'(t)/\varepsilon'(t=0)$) in various PEI/PI samples at 100 kHz and under room temperature conditions.

7.5 Influence of Absorbed Water

Most aromatic polymers exhibit relaxation processes in their dynamic mechanical and dielectric behaviors [132–134]. The α relaxation process, attributed to the glass transition, can normally be observed in PI at temperatures above 570 K. The two others, β and γ, are associated with localized motions of rigid segments along the PI backbone. They are, however, usually not present in the dry state but are induced by water molecules that are absorbed into the free volume of the polymer and attached to side polar groups via weak physical or stronger hydrogen bonds. β relaxation occurs in a temperature range around 350 K and is characterized by high values of the activation parameters, suggesting that this dissipation process originates from cooperative relaxation phenomena. On the other hand, the location and activation energy of the low-temperature ($\approx$200 K) γ relaxation are characteristic of local molecular motions [144,147,148].

Figure 35a shows the dielectric response of PI, detected at several frequencies during (i) a cooling run from room temperature to 150 K, (ii) a subsequent heating run to 400 K, and (iii) a final cooling run to 150 K, with the cooling/heating rate of $\pm$0.75 K min^{-1}. The relaxation, which is detected during the first cooling run, after the sample has been exposed to normal air atmosphere conditions, almost completely disappears during the second cooling run, after the sample has been heated (dried) to 400 K.

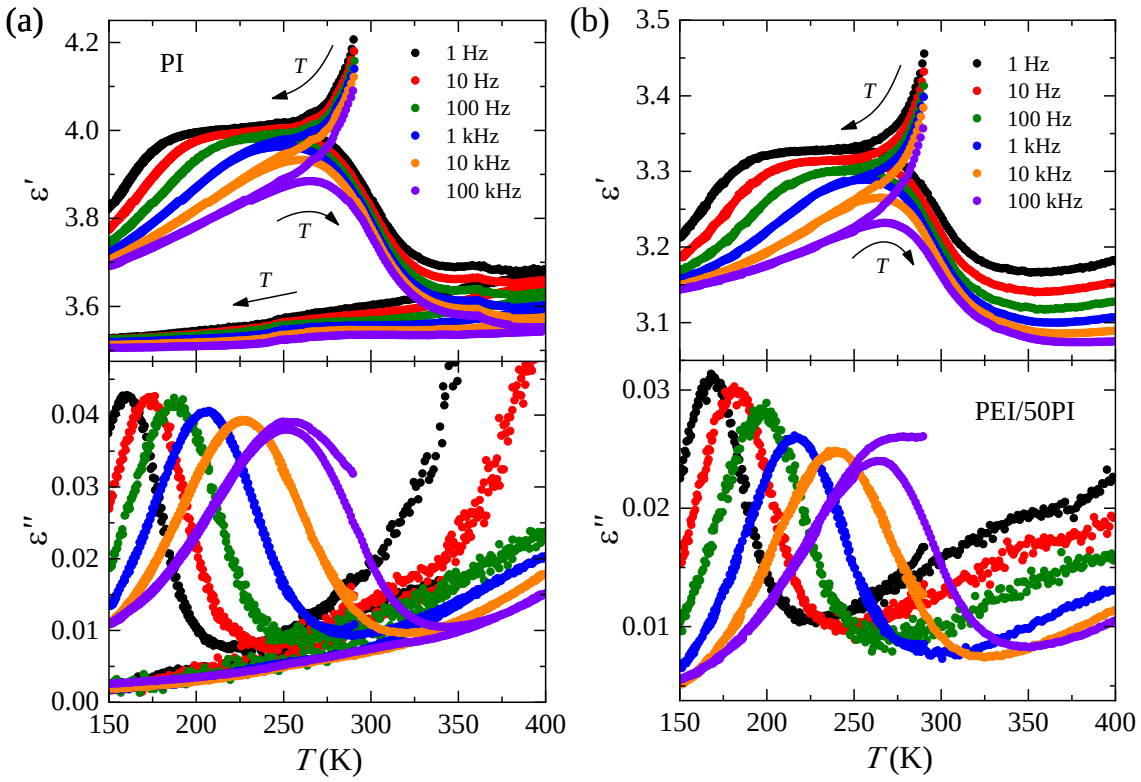

Figure 35: (a) Dielectric response of PI, detected at several frequencies during (i) a cooling run from room temperature to 150 K, (ii) a subsequent heating run to 400 K, and (iii) a final cooling run to 150 K (indicated by arrows). (b) Dielectric response of the PEI/50PI blend, detected during a cooling run from room temperature to 150 K and a subsequent heating run to 400 K (indicated by arrows).

Moreover, Figure 36 shows the relaxation frequency as a function of inverse temperature (data were determined from the $\varepsilon''(T)$ peak values), with the solid line representing a fit to the Arrhenius law: $\nu = \nu_0 \exp(-U_0/kT)$. The determined activation energy ($U_0 = 0.44$ eV) almost agrees with the theoretically predicted value of 0.45 eV for the γ relaxation process of PI [148].

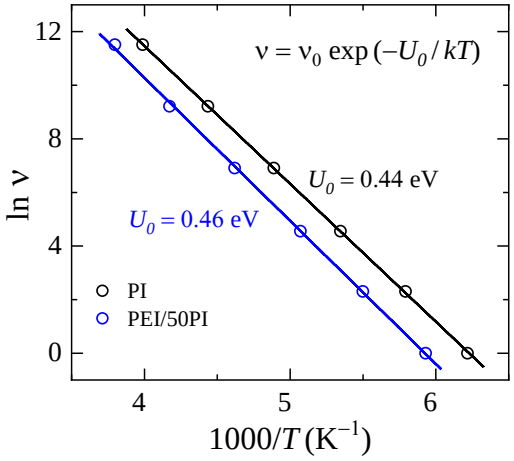

Figure 36: Dependence of the γ relaxation frequency on inverse temperature in PI and the PEI/50PI blend (from the data in Figure 35). Fits to the Arrhenius law (solid lines) reveal that the activation energies in both systems are almost identical.

The activation energy is almost identical in blend samples: we obtained values of $U_0 = 0.46$ eV in the PEI/40PI, $U_0 = 0.45$ eV in the PEI/80PI, and $U_0 = 0.46$ eV in the PEI/50PI blend. The dielectric response of the latter, detected during a cooling and a subsequent heating run, is shown in Figure 35b, while due to their similarity, the responses of the other two blends are not shown. This result reveals that interactions between PEI and PI polymer chains in the blends nearly do not affect the motion of side polar groups that contribute to the γ relaxation process.

7.6 Space Charge Contribution

While at higher measurement frequencies the dielectric response is governed by the intrinsic response of dipole moments, mobile space charges strongly influence the response at lower frequencies, with their contribution being more pronounced at higher temperatures. To reveal the amount of space charge in different samples, the main frame of Figure 37 presents the normalized low-frequency (1 Hz) dielectric permittivity ($\varepsilon'_{norm}(T) = \varepsilon'(T)/\varepsilon'(T = 250$ K)) of various blends and pristine PI. It should be stressed that all data were detected on completely dry, annealed samples; i.e., during cooling runs after the samples have been heated to 400 K (see Figure 33b). Any presence of water molecules could namely induce a similar dielectric response as accumulated space charges. The increase in ε'_{norm} at higher temperatures is much more pronounced in PI than in the blends, which undoubtedly reveals a significant amount of space charges in PI compared with the blend samples. The lowest influence of space charges has been detected in the PEI/80PI blend, which also exhibits the lowest intrinsic electrical conductivity (see Figure 32b).

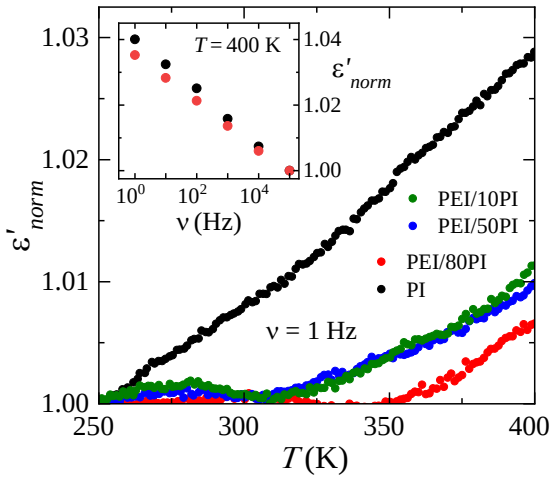

Figure 37: Low-frequency space charge contributions to the dielectric response of PEI/PI blends. Main frame: increase in the low-frequency ($\nu = 1$ Hz) normalized dielectric permittivity ($\varepsilon'_{norm}(T) = \varepsilon'(T)/\varepsilon'(T = 250\ \mathrm{K})$) at higher temperatures in various blends compared with pure PI. Inset: increse in the high-temperature (T = 400 K) normalized dielectric permittivity ($\varepsilon'_{norm}(\nu) = \varepsilon'(\nu)/\varepsilon'(\nu = 100\ \mathrm{kHz})$) at lower frequencies in PI and the PEI/80PI blend. Data were detected during cooling runs after the samples had been heated to 400 K.

Finally, the inset to Figure 37 additionally confirms higher space charge contributions in PI than in the PEI/80PI blend: the increasing of the high-temperature (T = 400 K) normalized dielectric permittivity ($\varepsilon'_{norm}(\nu) = \varepsilon'(\nu)/\varepsilon'(\nu = 100\ \mathrm{kHz})$) at lower frequencies is more pronounced in the pristine PI. Therefore, PEI/PI blends indeed accumulate less space charge than pristine PEI and PI.

7.7 Dielectric Breakdown Strength

An extensive review of the dielectric breakdown strength of PI films, based on the experimental data from 13 different publications, which were analyzed in terms of the Weibull statistical model and partially explained by percolation theories, revealed a strong dependence of E_b (reported values range from 800 up to 5200 kV cm^{-1}) on experimental conditions, film thickness, and surface electrode area [149]. The highest values were obtained for samples with extremely small surface electrodes (diameter of 0.2 mm). Moreover, a strong thickness dependence in the form of an inverse power function was reported: $E_b \propto d^{-1/3}$, [150]. Although the final thickness of films prepared by the solution casting method cannot be precisely controlled, and relatively large electrodes were used in dielectric investigations to enhance the measured signal due to low dielectric permittivity, E_b measurements were conducted for both pristine polymers and the blend systems.

Dielectric breakdown strength was determined as $E_b = V_{bd}/d$, where V_{bd} is the breakdown voltage, defined as the voltage at which the current through the sample exceeds 20 mA, and d is the sample thickness. Figure 38 shows data obtained from samples that are geometrically identical to those used for dielectric measurements (electrodes' diameter of 6 mm). Due to the notable influence of absorbed water on the overall dielectric response, the impact of high-temperature annealing on the dielectric breakdown strength was also investigated. It can be seen that unannealed PEI/PI blends exhibit ≈2.5 times higher E_b

values than pristine PEI and PI. On the other hand, annealing at 400 K for 1 hour before the measurement significantly increases the dielectric breakdown strength of pristine polymers, while values obtained in blend systems remain unchanged within the estimated experimental error (approx. 100 kV cm^{-1} in pristine and 200 kV cm^{-1} in blend systems; mainly attributed to slight thickness variations in different samples). This is most probably the result of a higher chain packing density in the blend systems and, concomitantly, a lower amount of absorbed water. Nevertheless, due to the much lower amount of space charge, E_b values of blends remain almost twice as high as those of annealed PEI and PI. Having in mind the large electrode area of our samples, the PI values confirm their good quality, as they are completely comparable with published data [149]. Finally, it should be stressed that all results in Figure 38 were obtained on intact samples. It namely turned out that the breakdown strength is significantly lower in samples that had previously been dielectrically investigated, possibly due to mechanical clamping in the measurement cell during temperature-dependent investigations.

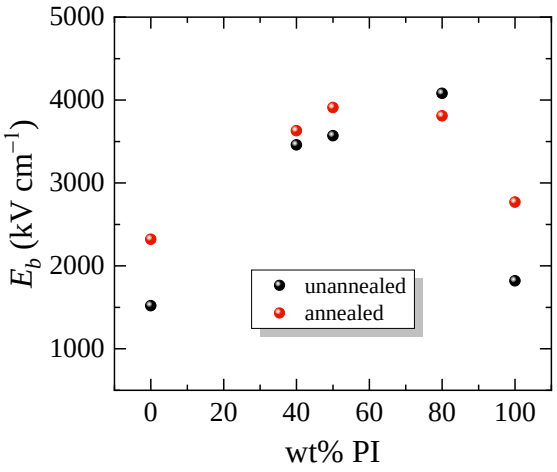

Figure 38: Dielectric breakdown strength of (i) unannealed PEI, PI, and PEI/PI blends and (ii) samples that were annealed at 400 K for 1 hour and then cooled back to room temperature before the measurement.

Blending PEI and PI indeed increases chain packing density, thereby limiting both the amount of water molecules that can be absorbed and the amount of accumulated space charge within the system. Since breakdown is initiated by charges accelerated by the applied electric field within voids in the system, both features contribute to the increase in E_b, as fewer space charges are accelerated and over shorter distances. The blending of appropriately matched polymers thus once again proves to be an effective strategy for improving the dielectric properties of polymer systems.

Chapter 8

Antiferroelectric PNZST Ceramics

In this chapter, a physical approach for achieving an enhanced dielectric response in an antiferroelectric system is presented using PNZST ceramics. To determine the specific experimental conditions under which an enhanced response can be induced and to evaluate their impact on the functional properties of the sample, an electric field-temperature phase diagram was constructed, and the nature of the phase transitions was investigated.

A large portion of this chapter was originally published in V. Jurečič *et al.*, *Phys. Rev. Mater.* (2023) 7(11): 114407, and in V. Jurečič *et al.*, *Adv. Funct. Mater.* (2025) 35(2): 2412739.

8.1 Overview

Antiferroelectric ceramics are considered highly promising materials for the development of novel DC-link, snubber, and filter capacitors used in high-power and high-speed electronics for electromotive and renewable energy applications, medical equipment, and weapons platforms. In particular, the increase in dielectric permittivity with an applied bias electric field, i.e., dielectric tunability, is one of the most interesting and still not fully understood functional properties of antiferroelectric materials.

Despite their promising dielectric behavior under an external bias field, only a few studies on the dielectric tunability of antiferroelectrics can be found [73,79,151–157]. Moreover, most works investigate the relationship between dielectric tunability and field-induced phase transitions or chemical modification.

It has been shown that the temperature and nature of inter-ferroelectric, ferroelectric-to-paraelectric [48], and relaxor-to-ferroelectric [49] phase transitions change under the influence of an external electric field. When an electric field is applied, a first-order phase transition can be transformed into a second-order one. The critical electric field and the corresponding temperature at which this crossover occurs define the critical point. Furthermore, if the second-order transition point represents a singularity that terminates the line of first-order phase transitions, it is referred to as the critical end point, above which supercritical behavior is observed [49]. In the supercritical regime, dielectric permittivity and heat capacity lose their critical character and become smeared out. At the critical end point, however, both dielectric permittivity and heat capacity diverge, leading to anomalous enhancements in functional properties such as piezoelectric and electrocaloric responses, as well as energy storage density [50,51].

It is known that antiferroelectrics exhibit their highest dielectric response during a phase transition, which is always accompanied by structural change, as a result of applying an electric field and temperature. It has been demonstrated that the presence of a critical

end point in ferroelectric and relaxor systems leads to significantly enhanced polarization, dielectric permittivity, piezoelectric response, and electrocaloric effects, which are attributed to the divergent behavior of the dielectric permittivity in the vicinity of the critical end point. Thus, a similar enhancement should also apply to antiferroelectric systems if a critical end point can be induced under certain experimental conditions.

8.2 Sample Characteristics

The investigation was exemplarily conducted on a (Pb,Nb)(Zr,Sn,Ti)O_3 system, which represents one of the most widely studied antiferroelectrics, with high-energy storage properties. $Pb_{0.99}Nb_{0.02}[(Zr_{0.57}Sn_{0.43})_{0.92}Ti_{0.08}]_{0.98}O_3$ (PNZST) with a ferroelectric-to-antiferroelectric-to-paraelectric phase sequence, was obtained by doping $PbZrO_3$ with suitable amounts of Sn, Ti, and Nb. The quality of the PNZST ceramic sample was checked by performing X-ray diffraction (XRD) and scanning electron microscopy (SEM). The room-temperature XRD pattern and SEM micrograph of the antiferroelectric PNZST sample (see Figure 39) suggest the presence of a pure perovskite phase with no evidence of secondary phases, which was further corroborated by energy-dispersive X-ray spectroscopy analysis of differently colored areas in the SEM micrograph. The XRD pattern matches the previously reported data in the literature [37,124], and its peaks are well indexed to a tetragonal perovskite system with space group P4mm (No. 99). Examination of the SEM micrograph confirms the high density of the prepared ceramics and a relatively uniform grain distribution.

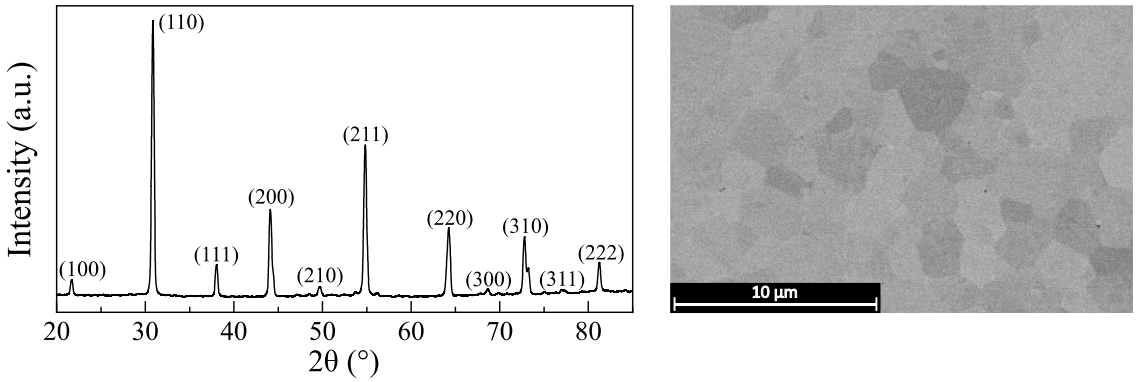

Figure 39: XRD pattern of the antiferroelectric PNZST ceramics with peaks indexed according to a pseudocubic perovskite structure (left), and SEM micrograph of a polished PNZST sample (right). Different shades of grey in the SEM micrograph indicate different grain orientations.

The investigated composition of PNZST ceramics possesses a rhombohedral ferroelectric (FE) phase at low temperatures, which transforms, upon increasing the temperature, into a tetragonal antiferroelectric (AFE) phase at ≈304 K, a paraelectric (PE) multicell cubic phase at ≈411 K, and a single-cell cubic phase at ≈453 K [81,158]. The temperature evolution of the phases and their transition temperatures are highly sensitive to thermal and electrical treatment history. Therefore, the 230 μm thick sample, with sputtered gold electrodes of a diameter 1.5 mm, was heated to 430 K for 15 min before each measurement to avoid any history-dependent effects.

8.3 Isofield Dielectric Measurements

The temperature-dependent complex dielectric constant was measured under various DC bias electric fields to determine FE–AFE and AFE–PE phase transition temperatures. Figure 40a shows the temperature dependence of the real and imaginary parts of the complex dielectric constant between 240 and 430 K during heating at a rate of 1 K min^{-1} for all applied DC bias electric fields. Typically, the resistance of the ferroelectric material drops at the phase transition, which manifests itself in the increase of the imaginary part of the complex dielectric constant (ε''). Therefore, the FE–AFE and AFE–PE phase transition temperatures were determined from the first and second peaks of ε'', respectively. The sequence of phase transitions and their temperatures at zero electric field (FE $\xrightarrow{297\ K}$ AFE $\xrightarrow{408\ K}$ PE) is in good agreement with the literature [81,98]. Applying an external DC electric field shifts the FE–AFE and AFE–PE transition temperatures. The FE–AFE transition temperature increases, while the AFE–PE transition temperature decreases with increasing electric field. At an electric field of 21 kV cm^{-1}, the FE–AFE and AFE–PE transition temperatures shift to 370 and 396 K, respectively. By further increasing the electric field, the transition anomalies finally merge at 25 kV cm^{-1} and 388 K.

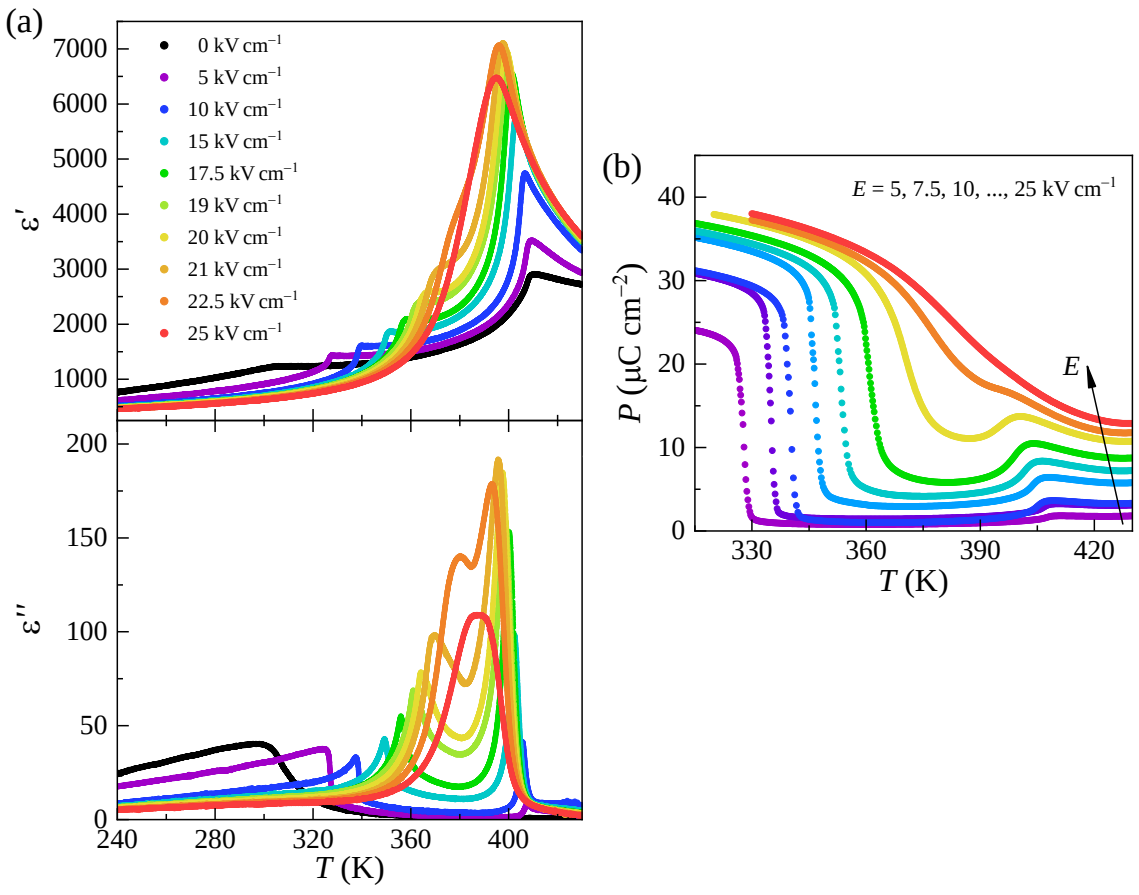

Figure 40: (a) Real and imaginary parts of the complex dielectric constant as a function of temperature measured at 1 kHz and various DC bias electric fields. (b) Temperature evolution of macroscopic polarization measured at electric fields from 5 to 25 kV cm^{-1} in steps of 2.5 kV cm^{-1}.

To determine the order of the phase transitions, polarization under various DC bias electric fields in the temperature range of the previously determined phase transition temperatures was measured. The FE–AFE and AFE–PE transition temperatures obtained from dielectric measurements coincide well with the sharp drop of polarization at lower temperatures and the anomaly at higher temperatures depicted in Figure 40b. The sharp drop of macroscopic polarization at the FE–AFE transition corroborates the first-order nature of the transition as demonstrated in Ref. [98]. The applied electric field not only shifts the transition temperatures but also changes the evolution of polarization. The FE–AFE transition is sharp and discontinuous at low electric fields, whereas it becomes continuous at 22.5 kV cm^{-1} and smeared and suppressed above 22.5 kV cm^{-1}, suggesting a supercritical behavior and the existence of a critical end point. The non-zero macroscopic polarization in the AFE phase implies that the FE–AFE transition is not fully reversible: remains of the FE phase persist under the applied electric field, resulting in a so-called ferrielectric state [98,99,159,160]. In this state, the antiparallel sublattice polarizations do not completely cancel each other, because one sublattice aligns favorably with the field. This effect becomes more pronounced under higher fields. Consequently, the measured polarization in the AFE phase increases with the applied field, rising from 1 to 11 μC cm^{-2} as the field is increased from 5 to 20 kV cm^{-1}. Upon approaching the AFE–PE transition temperature, the polarization exhibits an anomaly that shifts toward lower temperatures with increasing electric field, coinciding with the second peak of ε''. Therefore, this anomaly can be attributed to the AFE–PE transition. However, its behavior does not reveal any information about the nature of the AFE–PE phase transition as clearly as the polarization change does during the FE–AFE transition. Thus, we measured the third harmonic component of the dielectric permittivity (ε_3'). It has been predicted by the thermodynamic theory and demonstrated experimentally that ε_3' changes its sign at the Curie temperature for the second-order phase transition, whereas for the first-order transition, the sign remains positive [161]. The sign of the measured ε_3' of PNZST ceramics (see Figure 41) does not change at the AFE–PE transition temperature; hence, the transition is of the first order. This is in accordance with differential scanning calorimetry results, where two endothermic peaks were detected at the FE–AFE and AFE–PE transitions, indicating both transitions are of the first order [162]. Therefore, both FE–AFE and AFE–PE phase transitions can change to the second order under an externally applied electric field.

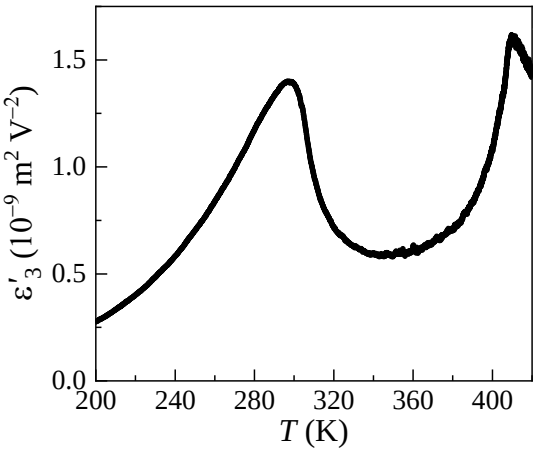

Figure 41: Temperature dependence of the real part of the third harmonic component of the dielectric permittivity measured at zero DC bias field.

The divergent nature of the dielectric permittivity was analyzed to determine the electric field and temperature of the critical end points that terminate the lines of the first-order FE–AFE and AFE–PE phase transitions. To identify the divergent nature of the dielectric permittivity at the FE–AFE phase transition, the background of the dielectric response was first fitted with a polynomial function that best described the data on the left and right side of the FE–AFE peak. Figure 42a depicts the background fit for the dielectric response measured at 10 kV cm^{-1}. Then, the fitted background response was subtracted from the measured dielectric response to determine the electric field at which the dielectric permittivity exhibits the maximum value. Figure 42b shows the subtracted dielectric response around the FE–AFE phase transition. The dielectric permittivity at the FE–AFE transition increases under higher electric fields and exhibits the maximum value at 21 kV cm^{-1}. Further increasing the electric field leads to a suppressed and smeared dielectric response at the FE–AFE phase transition. Similar to the FE–AFE transition, the AFE–PE phase transition also exhibits an enhanced dielectric response at 21 kV cm^{-1} and a smeared and suppressed dielectric response at higher electric fields (see Figure 40a).

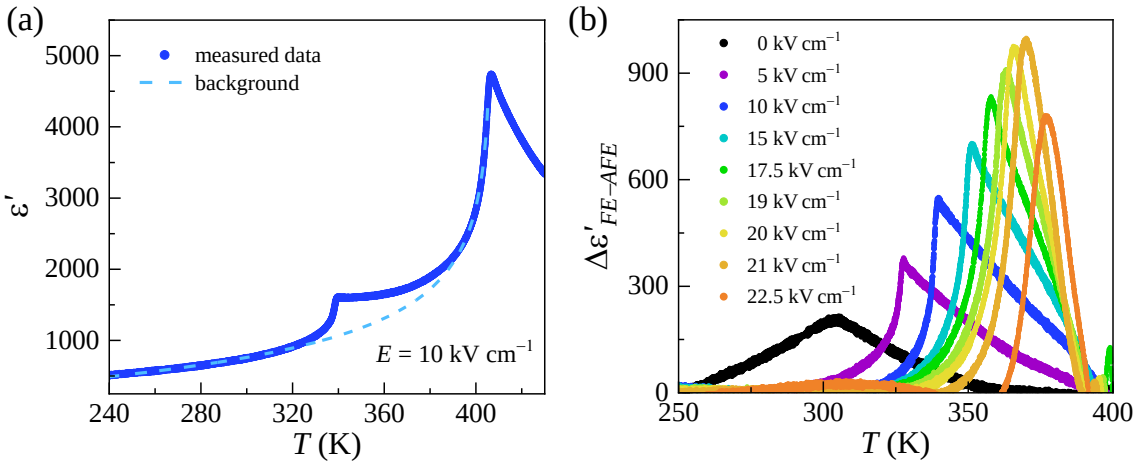

Figure 42: (a) Dielectric response measured at 10 kV cm^{-1}. The background is represented by the dashed line. (b) Dielectric anomaly of dielectric permittivity around FE–AFE phase transition, after the fitted background was subtracted from the measured data. The maximum dielectric permittivity is determined at 21 kV cm^{-1} and 370 K.

8.3.1 Electric field–temperature phase diagram

According to the determined order of the FE–AFE and AFE–PE phase transitions under different experimental conditions, an electric field–temperature (E–T) phase diagram was constructed. The analyzed dielectric response at the FE–AFE and AFE–PE phase transitions demonstrates a typical behavior anticipated for a critical end point and a supercritical regime. It can be concluded that the lines of the first-order FE–AFE and AFE–PE phase transitions terminate in two critical end points located at $E_{CP}^{FE-AFE} = 21$ kV cm^{-1}, $T_{CP}^{FE-AFE} = 370$ K and $E_{CP}^{AFE-PE} = 21$ kV cm^{-1}, $T_{CP}^{AFE-PE} = 396$ K, respectively. The temperature stability of FE, AFE, and PE phases under various electric fields are represented in the E–T phase diagram depicted in Figure 43, with locations of both critical end points denoted by stars. Above the electric field of the critical end points, both transitions exhibit supercritical behavior. The FE–AFE phase transition merges with the

AFE–PE phase transition at an electric field of 25 kV cm^{-1} and a temperature of 388 K, i.e., at the triple point.

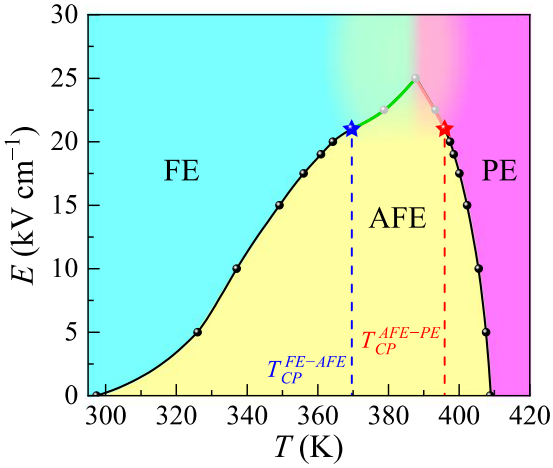

Figure 43: Electric field–temperature phase diagram of antiferroelectric PNZST ceramics. Solid lines represent the first-order FE–AFE and AFE–PE transition lines, which are terminated by the critical end points marked with stars. Above the critical end points, both transitions exhibit supercritical behavior. The FE–AFE and AFE–PE phase transitions merge at 25 kV cm^{-1} and 388 K.

8.4 Recoverable Energy Storage Density

To determine the recoverable energy storage density (W_{rec}) and its relation to both critical end points in the antiferroelectric PNZST ceramics, the polarization hysteresis loops at different temperatures were measured (see Figure 44a), and W_{rec} was determined according to Eq. (3): by integrating the area between the upper branch of the polarization hysteresis loop and the polarization axis (see Figure 44b).

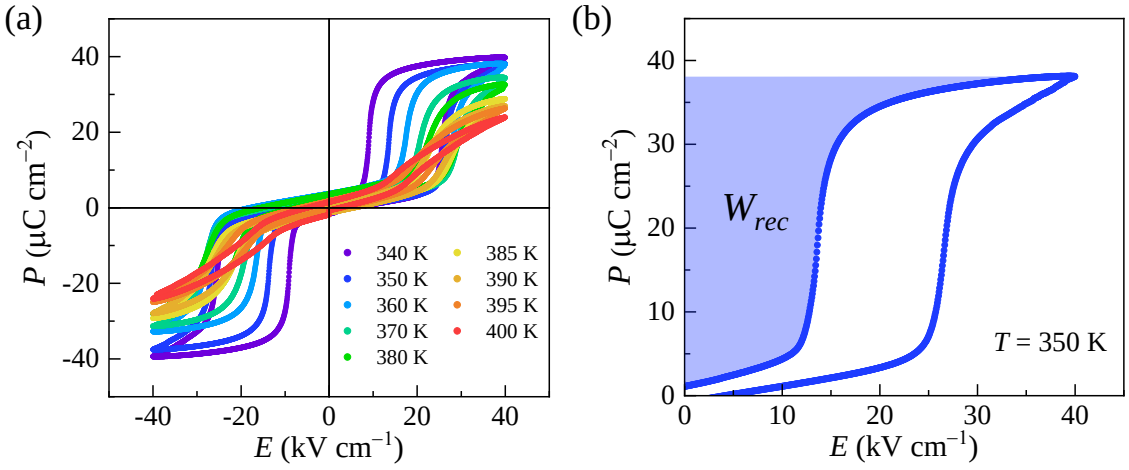

Figure 44: (a) Polarization hysteresis loops at all measured temperatures. (b) Recoverable energy storage density (W_{rec}) at 350 K, determined from the colored area.

Figure 45a shows the temperature-dependent W_{rec} of the antiferroelectric PNZST ceramics. The maximum W_{rec} of 0.66 J cm^{-3} is observed at 370 K, which corresponds to the temperature of the FE–AFE critical end point. To understand the enhancement of W_{rec}, the interplay between the maximum polarization, reverse critical electric field, and the shape of the polarization hysteresis curve needs to be considered. Figure 45b depicts the temperature behavior of the maximum polarization (P_{max}) and the slope of the P–E curve around the field-induced phase transition (P_{slope}). Below the temperature of the FE–AFE critical end point, P_{max} exhibits a gradual decay with increasing temperature. A significant decrease of P_{max} at the FE–AFE critical end point and an increase of the decay rate above the FE–AFE critical end point are observed. Thus, according to Eq. (3), W_{rec} should decrease with increasing temperature. However, with increasing temperature, the critical electric field for induction of the FE phase increases, which, in contrast to the decreasing polarization, contributes to the increase of W_{rec}.

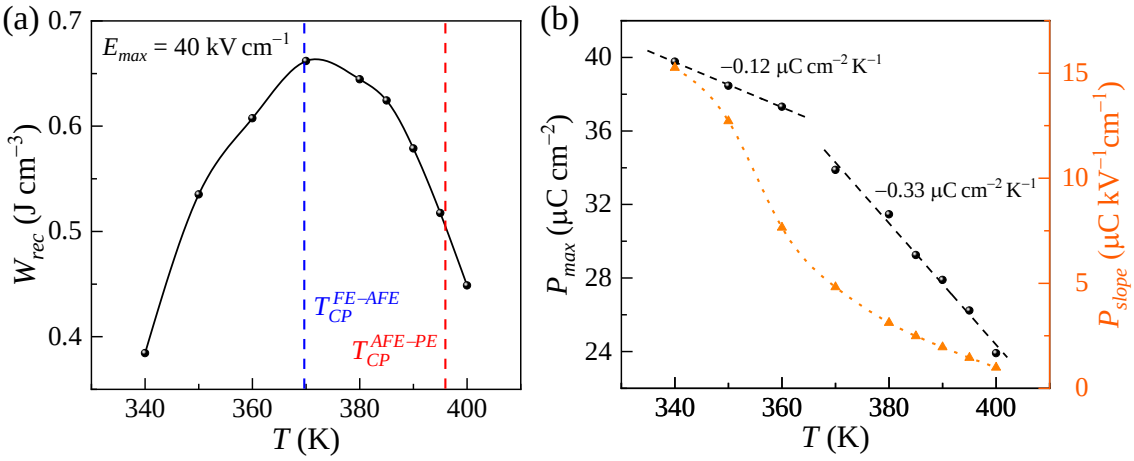

Figure 45: (a) Temperature-dependent recoverable energy storage density of PNZST ceramics obtained at 40 kV cm^{-1}. Blue and red dashed lines indicate the temperatures of the FE–AFE and AFE–PE critical end points, respectively. (b) Temperature evolution of the maximum polarization and the slope of the P–E curve determined around the AFE–FE phase transition of PNZST ceramics.

Another critical parameter that influences the integrated area used to calculate W_{rec} is the shape of the P–E curve, which is determined by the slope of the P–E curve around the AFE–FE phase transition. P_{slope} at 340 K is steep, which indicates the first-order nature of the field-induced phase transition (see Figure 45b). With increasing temperature, P_{slope} decreases, which indicates the transition from the first to second-order phase transition. In addition, the decrease in P_{slope} changes the shape of the polarization curve, which becomes more slanted above the FE–AFE critical end point. Hence, the enhancement of W_{rec} in the vicinity of the critical end point is a result of the interplay between the maximum polarization, reverse critical electric field, and the shape of the polarization curve. In the vicinity of the FE–AFE critical end point temperature, the maximum polarization is reduced by ≈15 % compared to 340 K, while the reverse critical electric field increases by almost 53 %. Although the slope of the P–E curve is also reduced in the vicinity of the FE–AFE critical end point, it does not result in a strongly slanted polarization curve. The enhancement at the FE–AFE critical end point can be attributed to the relatively small reduction of the maximum polarization and a strong increase of the reverse critical electric field. Furthermore, the decrease in W_{rec} above the FE–AFE critical

end point is related to the stronger decrease in the maximum polarization due to the slanted shape of the polarization curve and only a small change in the reverse critical electric field.

8.5 Dielectric Tunability

Figure 46a–c depict the dielectric response as a function of the DC bias electric field at 343, 373, and 395 K, respectively, measured using a 1 V AC signal at 1 kHz. The selected temperatures represent the dielectric hysteresis response at the first-order AFE–FE phase transition, in the vicinity of the FE–AFE critical end point, and in the vicinity of the AFE–PE critical end point, respectively. At 343 K, the evolution of the dielectric permittivity as a function of the electric field exhibits a sluggish increase with an increasing electric field, which becomes steeper upon approaching the first-order AFE–FE phase transition (see Figure 46a). After the FE phase is induced, a sharp decrease in dielectric permittivity is observed, caused by polarization saturation and attributed to the poled FE state, in which domains reorient and domain walls become pinned in the direction of the applied field [42,44,45]. Moreover, hardening of the soft phonon mode further reduces the intrinsic lattice contribution to the dielectric permittivity with increasing field in the FE phase [46]. In the vicinity of the FE–AFE critical end point temperature, the increase in dielectric permittivity at low electric fields becomes faster, and its enhancement at the field-induced AFE–FE phase transition temperature is larger (see Figure 46b). Moreover, in the vicinity of the AFE–PE critical end point temperature, the increase in dielectric permittivity becomes even more pronounced and exhibits the largest enhancement (see Figure 46c).

To understand the role of both critical end points on the dielectric enhancement with an applied electric field, the dielectric tunability was calculated at various temperatures. The dielectric tunability (η) was calculated via Eq. (5). The data for the calculations were extracted from the second ε'–E measurement loop (see Figure 46a–c). The temperature-dependent dielectric tunability is depicted in Figure 46d. In the temperature range of the first-order AFE–FE phase transition, i.e., between 343 and 370 K, the dielectric tunability is between 15 and 60 %. However, a strong enhancement of the tunability for a factor larger than 2 (221 %) is obtained at 395 K. Such an enhancement of the dielectric permittivity by far exceeds the tunability values (88 %) reported for ferroelectric and relaxor systems [54]. The temperature of the maximum dielectric tunability lies in the proximity of the AFE–PE critical end point (396 K), which demonstrates that the AFE–PE critical end point plays a crucial role in the enhancement of the dielectric response under an applied electric field. This observation supports the assumption that the increased dielectric response at the temperature of a critical end point is due to the flattening of the free energy potential, which allows easy polarization extension under small perturbation fields. Furthermore, since the critical end point terminates the line of the first-order phase transition above which the transition becomes supercritical, it is expected that the free energy surface also becomes spherically degenerate. Consequently, polarization can easily rotate between the degenerated phases, which is a well-known mechanism responsible for enhanced functional properties of ferroelectrics [163,164]. It should be stressed that the flattening of the free energy is also expected at the FE–AFE critical end point; however, the polarization change during rotation between the FE and AFE phases is expected to be smaller than that between the AFE and PE phases.

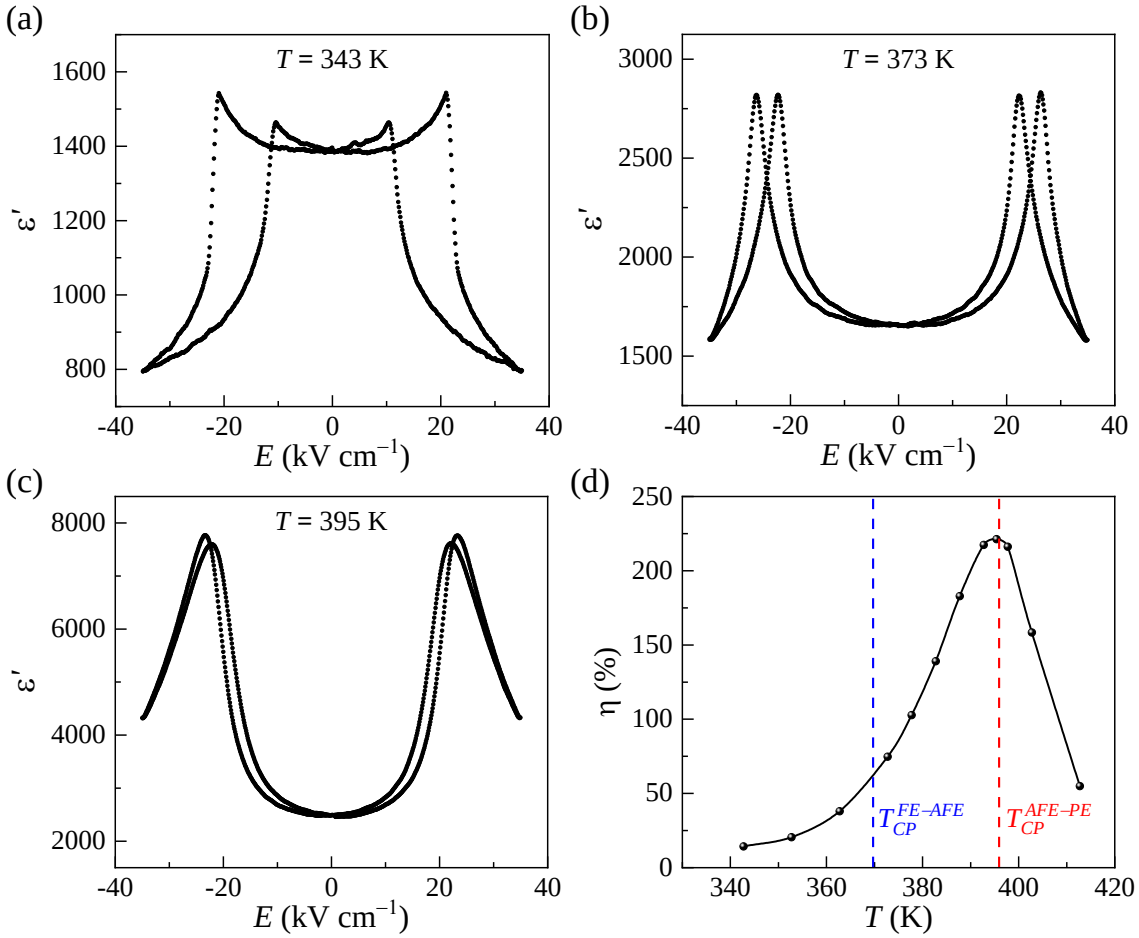

Figure 46: (a–c) Evolution of the dielectric permittivity as a function of DC electric field during the second measurement loop in PNZST ceramics at representative temperatures corresponding to a first-order AFE–FE phase transition, the FE–AFE critical end point, and the AFE–PE critical end point, respectively. (d) Tunability of the dielectric response as a function of temperature. Blue and red dashed lines represent the temperatures of the FE–AFE and AFE–PE critical end points, respectively.

8.6 Origin of Enhanced Dielectric Tunability

To determine whether the increase in dielectric permittivity under the electric bias field originates from free energy instability at the field-induced phase transition or is a result of domain rearrangement in the AFE phase, additional measurements were conducted. By simultaneously measuring the dielectric hysteresis loops and the sample temperature with a miniaturized 500 kΩ NTC thermistor attached to the sample, the sample temperature change in correlation to different excitation electric fields was studied.

Figure 47a shows the dielectric response and the sample temperature change (ΔT_{sample}) as a function of the externally applied DC bias electric field. At 343 K, the sample exhibits an antiferroelectric behavior with zero macroscopic polarization. The electric field evolution of the dielectric permittivity depicts the expected antiferroelectric-like response with increasing dielectric permittivity at lower electric fields. At and above the field-induced

AFE–FE phase transition, an expected ferroelectric response is observed with a sharp reduction in dielectric permittivity. The four peaks in the dielectric response reveal the reversibility of the field-induced AFE–FE phase transition. Moreover, the sample temperature response shows two positive and two negative temperature changes, which are associated with the release and absorption of the latent heat at the first-order field-induced phase transitions [98]. The high-resolution temperature measurement shows a small temperature difference of ≈33 mK between the positive and negative temperature changes of the sample. The difference could be attributed to the additional heating at the AFE–FE phase transition, originating from the domain wall switching of the FE phase [165–167].

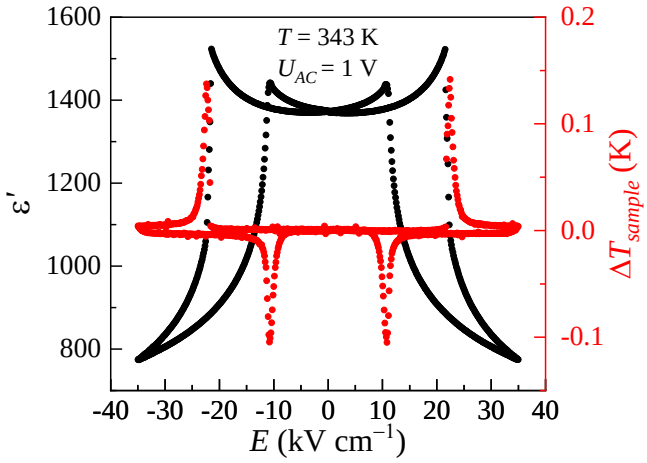

Figure 47: Dielectric and temperature measurements as a function of DC electric field during the second measurement loop at 343 K, with a 1 V AC signal at 10 kHz.

A more detailed insight into the dielectric and temperature response under the applied DC electric field is shown in Figure 48a,b. Figure 48a depicts the response of the dielectric permittivity and the sample temperature change obtained in the first quarter of the electric field cycle. The dielectric permittivity remains nearly constant at electric fields up to ≈10 kV cm^{-1}. However, above 10 kV cm^{-1}, the dielectric response nonlinearly increases and reaches the maximum value at the critical electric field at which the FE phase is induced. The increase in dielectric permittivity in the antiferroelectric phase could be attributed to the transition instability and divergent nature of the dielectric permittivity at the field-induced first-order phase transition. On the other hand, the sample temperature remains constant up to the critical field of the phase transition, which indicates no release of latent heat due to pretransition effects of the field-induced phase transition. The imaginary part of the complex dielectric constant determines the energy loss per unit volume in the material, which in ferroelectric materials is partly attributed to domain switching [165,166]. The electric field evolution of ε'' exhibits similar behavior to that of the dielectric permittivity (see Figure 48b). Low ε'' values (5 at zero electric field and 25 just before the AFE–FE transition, corresponding to low dielectric losses ($\tan\delta = \varepsilon''/\varepsilon'$) of ≈0.004 and ≈0.018, respectively) indicate minimized domain activity and negligible heat losses in the antiferroelectric phase.

In order to verify the responsibility of domain wall movement, the dielectric and thermal responses were investigated under various AC signals between 1–20 V superimposed on a DC bias electric field, which was cycled with 1 mHz. The influence of different AC signals on the dielectric permittivity in the first quarter of the second ε'–E measurement loop at ≈343, ≈370, ≈388, and ≈395 K is presented in Figure 49. Figure 49(a) shows a sluggish

increase in dielectric permittivity, followed by a sharp decrease, which is typical for a first-order AFE–FE phase transition at all measured AC signals. By increasing the magnitude of the superimposed AC voltage from 1 to 20 V, the dielectric permittivity increases from ≈1370 to ≈1630 at ≈343 K and zero DC electric field. The superimposed AC signal disturbs a nearly homogeneous DC electric field and is the cause of domain activity [43,168]. At higher temperatures, the increase in dielectric permittivity at lower electric fields becomes faster, and the first-order phase transition changes to second-order in the proximity of the FE–AFE critical end point temperature (see Figure 49b). By applying a 20 V AC signal instead of a 1 V signal, the maximum dielectric permittivity increases for approximately 500, 3000, 5400, and 4100 at ≈343, ≈370, ≈388, and ≈395 K, respectively. This indicates that domain contribution is the highest at ≈388 K. While the maximum value of the dielectric permittivity, measured with a 1 V AC signal, is obtained at ≈395 K, i.e., near the temperature of the AFE–PE critical end point (see Figure 49d), the highest dielectric permittivity ($\varepsilon' = 10365$) is measured at ≈388 K, i.e., at the temperature of the triple point, with a 20 V AC signal (see Figure 49c). Peaks of the dielectric permittivity are shifted toward lower electric fields at higher AC signals at all measured temperatures (see Figure 49). The AC signal contributes to the applied DC electric field; therefore, the critical electric field is achieved at a lower electric field. Moreover, the field range over which ε' remains constant decreases with increasing AC signal, as the nonlinear contribution to the dielectric response becomes more pronounced (see Figure 49). At 1 V AC signal, ε' remains constant up to ≈10 kV cm^{-1}, while at 20 V AC signal it begins to increase at ≈4 kV cm^{-1} at 343 K. ε'' shows the same dependence on AC signal as ε' (see Figure 50a). Furthermore, higher ε' and ε'' values under stronger AC signals indicate increased domain activity [42,168,169]. This is corroborated by thermometry, which exhibits a similar behavior. Figure 50 shows ε'' and the sample temperature change at different amplitudes of the AC field at 343 K. At 1 and 5 V AC signals, the sample temperature remains constant up to the critical field of the phase transition, indicating weak domain activity. However, at higher AC signals, the sample temperature starts to increase at lower electric fields due to enhanced domain mobility and, consequently, increased heat production. A similar response was observed at all measured temperatures.

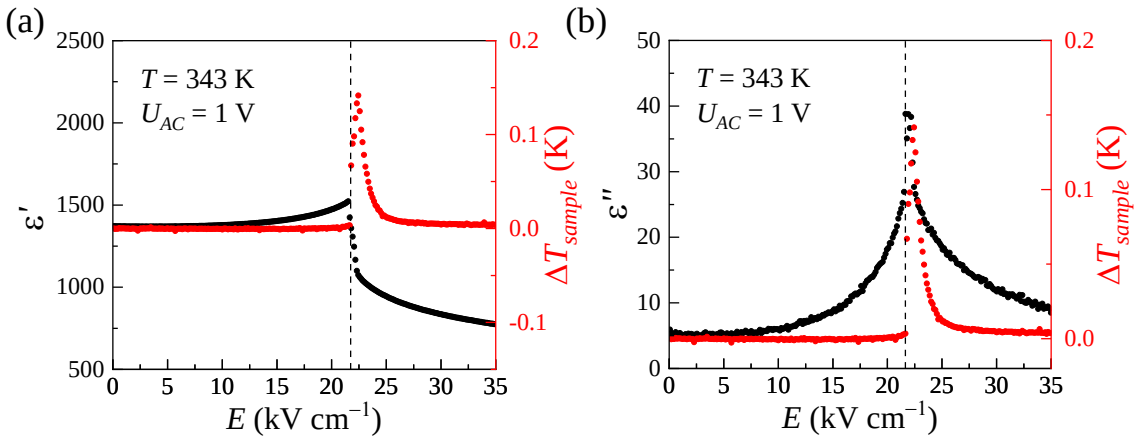

Figure 48: A detailed view of (a) the dielectric permittivity and (b) the imaginary part of the complex dielectric constant plotted alongside the temperature change obtained in the first quarter of the electric field cycle with a 1 V AC signal.

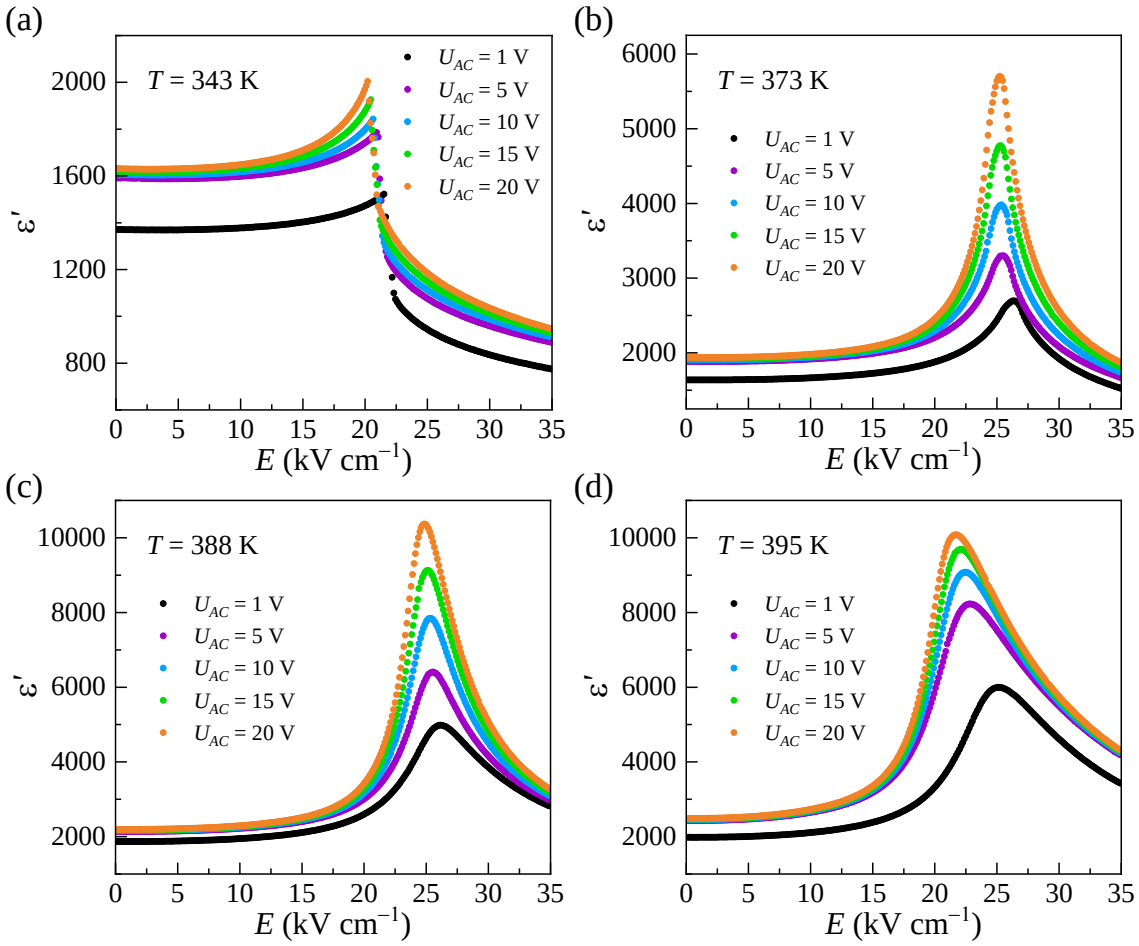

Figure 49: Comparison of the dielectric permittivity as a function of DC electric field during the first quarter of the second measurement loop, measured with different AC signals at 10 kHz, at temperatures corresponding to (a) a first-order AFE–FE phase transition, (b) the FE–AFE critical end point, (c) the triple point, and (d) the AFE–PE critical end point.

The increase of the ε' magnitude and nonlinearity of the system, as well as the increase of ε'' indicate the increase of the extrinsic contributions, which, according to the basic Rayleigh relations, should be irreversible. This is corroborated by the sample temperature change as a function of the electric bias field obtained at various AC signals. The sample temperature change increases with increasing AC signal in the antiferroelectric phase, which could be due to the irreversible domain wall contribution and the generated heat associated with it. Figure 50b shows the sample's temperature response at different amplitudes of the AC fields at 343 K. At 1 and 5 V AC signal, the sample temperature remains constant up to the critical field of the phase transition, indicating weak domain activity. However, at higher AC signals, the sample temperature starts to increase at lower electric fields due to the enhanced domain mobility and, consequently, increased heat production. Hence, the in-situ dielectric and thermometry results demonstrated that the increase in dielectric permittivity in the antiferroelectric phase under an external electric field is related to hysteretic nonlinear processes, most likely to the irreversible domain wall contribution. Therefore, to identify the influence of domain wall contributions on dielectric tunability, it was calculated at different temperatures and AC signals.

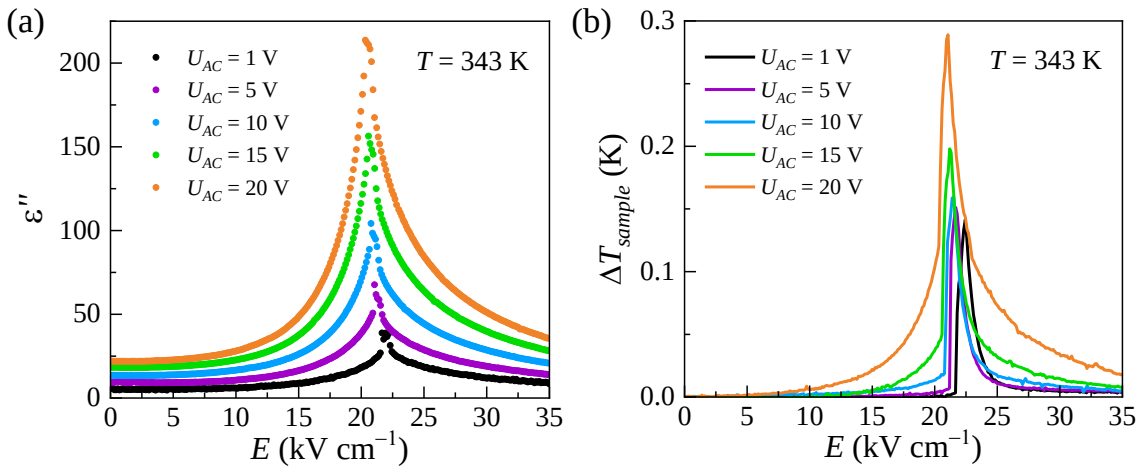

Figure 50: Comparison of (a) the imaginary part of the complex dielectric constant and (b) the sample temperature change as functions of DC electric field, measured with different AC signals at 10 kHz and 343 K.

Figure 51a–c show the dielectric permittivity as a function of the DC electric field at 388 K for three different AC signals: 1, 10, and 20 V, respectively. At 388 K and 1 V AC signal, the dielectric permittivity changes by ≈3140 when the bias electric field is increased from zero to the critical electric field, which is much larger compared to a change of ≈150 in ε' at 343 K. The dielectric permittivity change is further enhanced by increasing the AC signal. At 20 V AC signal, ε' changes by ≈8180 at 388 K and only by ≈370 at 343 K. The comparison reveals a strong impact of temperature on the dielectric permittivity change under bias electric field and AC signal. Thus, the dielectric tunability was calculated as a function of temperature from the temperature-dependent dielectric hysteresis loops and is shown in Figure 51d for different AC signals. An increase in dielectric tunability is clearly visible, especially between FE–AFE and AFE–PE phase transition temperatures. The dielectric tunability increases from 206 % to an extraordinarily high value of 373 % as the AC signal is increased from 1 to 20 V. Besides the strong enhancement of the dielectric tunability, the temperature at which it reaches its maximum shifts from 395 to 388 K as the AC signal increases from 1 to 20 V.

The maximum dielectric tunability obtained at 1 V AC signal is associated with the proximity of the field-induced AFE–PE critical end point and the flattening of the free energy potential minimum, while the overall maximum dielectric tunability was achieved at a 20 V AC signal near the triple point temperature. The coexistence of different phases requires the degeneration of their free energy [164]. Phenomenological Landau theory predicts a strong reduction of the anisotropic free energy in ferroelectrics at the triple point, where the anisotropic part of the free energy is reduced to zero. According to the classical domain theory, the domain size (D) is proportional to the anisotropic free energy (G_{aniso}): $D \sim \sqrt{|G_{aniso}|}/P$. Thus, the reduction of the anisotropic free energy manifests itself as a decrease in domain size [56,164]. In the vicinity of the triple point, the anisotropic energy approaches zero, reducing the domain size to sub-nanometer dimensions, which has also been experimentally observed in ferroelectrics [170,171]. Hence, a reduction of the anisotropic energy and minimization of the domain structure are also expected at the field-induced triple point in antiferroelectric PNZST ceramics. In addition, minimization of domain size leads to an increase in domain density and, consequently, may result in

increased non-linear or extrinsic contributions to dielectric tunability. The proposed enhancement mechanism is schematically illustrated in Figure 51e.

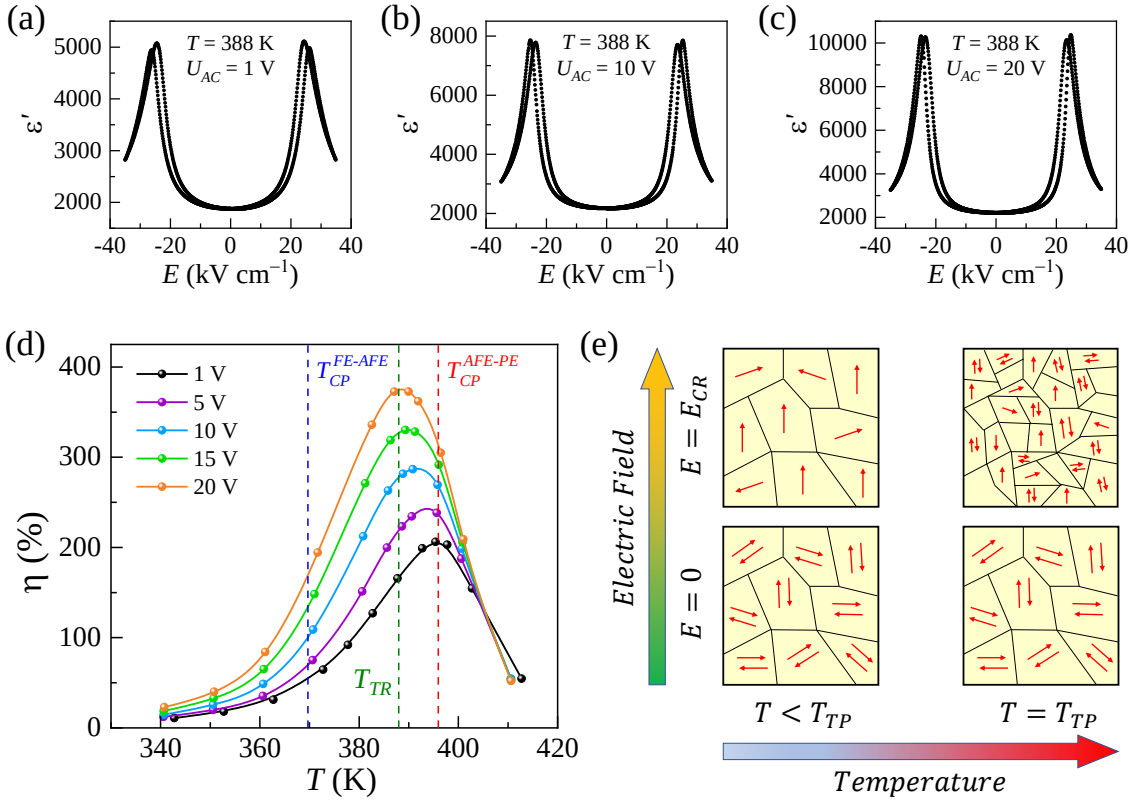

Figure 51: (a-c) Dielectric permittivity as a function of DC electric field for AC signals of 1, 10, and 20 V at 10 kHz during the second measurement loop. d) Dielectric tunability as a function of temperature measured at different AC signals. Vertical lines from left to right represent temperatures of the FE–AFE critical end point, triple point, and AFE–PE critical end point, respectively. e) Illustration of the field-induced evolution of the domain structure below and at the triple point.

To further confirm the role of domain contribution in the enhancement of dielectric tunability in antiferroelectric PNZST ceramics, Rayleigh analysis of the dielectric response as a function of the AC signal was conducted. Rayleigh law is typically used in ferroelectrics to determine the reversible and irreversible contribution of the interface motion to the piezoelectric and dielectric properties [42,43,172,173], but it has also been successfully employed in an antiferroelectric La-doped $PbZrO_3$ [174] and $(Pb,La)(Zr,Ti)O_3$ thin film [175]. The Rayleigh analysis of the dielectric response as a function of the AC signal provides information on the non-linear contribution to the dielectric response, based on relation: $\varepsilon' = \varepsilon'_{int} + \alpha E_0$, which is described in more detail in Section 5.4. The irreversible Rayleigh coefficient (α) is typically used to quantify the contribution of irreversible domain wall or, more generally, interface displacements [175].

Figure 52 shows the dependence of dielectric permittivity on the AC voltage signal at 340, 370, 388, 395, and 405 K, measured under various external DC electric fields. Below 395 K, a similar trend is observed: for DC bias fields below 15 kV cm^{-1}, the AC voltage signal has a nearly negligible impact on dielectric permittivity; however, above 15 kV cm^{-1}, a significant increase in ε' with the applied AC signal is observed. The most significant

change in dielectric permittivity occurs at 24 kV cm^{-1}, just below the critical electric field associated with the field-induced AFE–FE phase transition at these temperatures. At 30 kV cm^{-1}, i.e., above the field-induced AFE–FE phase transition, the effect of the AC signal diminishes, indicating reduced dielectric nonlinearity. This decrease can be attributed to the stabilization of the FE phase and alignment of the FE domains with the electric field. As the FE phase stabilizes more easily at higher temperatures, the largest nonlinear response occurs at lower electric fields: 20 kV cm^{-1} at 395 K and 10 kV cm^{-1} at 405 K. The slopes represent the nonlinear Rayleigh coefficient, which clearly depends on both temperature and applied DC field.

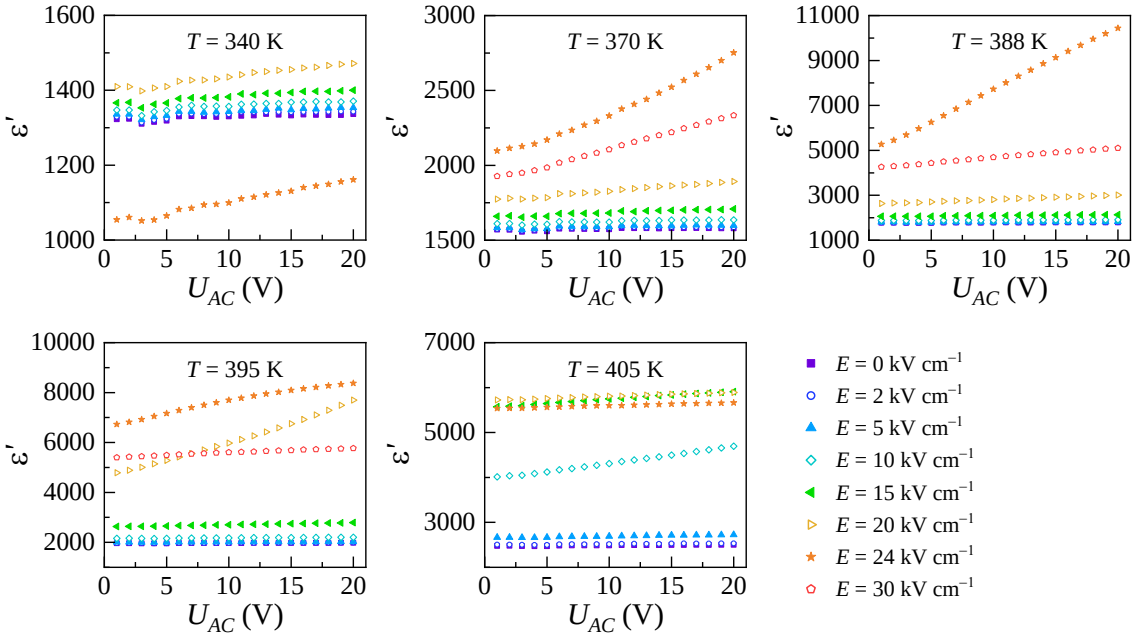

Figure 52: Dielectric permittivity as a function of the AC signal amplitude, measured at 340, 370, 388, 395, and 405 K under different DC electric fields.

Figure 53a depicts the irreversible Rayleigh coefficient as a function of electric field at several temperatures, determined from the slopes in Figure 52. The Rayleigh coefficient exhibits nearly the same behavior for all temperatures. At low electric fields, the Rayleigh coefficient is small, which implies low irreversible domain dynamics. With increasing electric field, the coefficient increases and reaches a maximum value in the vicinity of the critical electric field that induces the AFE–FE phase transition. Concomitantly with the phase transition, alignment of FE domains occurs, which decreases the irreversible coefficient and thus the domain contribution to the dielectric response in the FE phase. The increase of the irreversible Rayleigh coefficient with electric field suggests an increased irreversible domain wall contribution [176] to the dielectric response in the antiferroelectric phase. Rayleigh analysis was undertaken at various temperatures, and for each temperature, the maximum non-linear Rayleigh coefficient (α_{max}) was found close to the critical electric field of the AFE–FE phase transition. Figure 53b shows the maximum Rayleigh coefficient as a function of temperature. The highest Rayleigh coefficient was obtained at 388 K, which coincides with the temperature of the triple point found in antiferroelectric PNZST ceramics. This can be explained by the minimization of domain size and the increase in domain density, resulting in the largest domain contribution near the electric field-induced triple point.

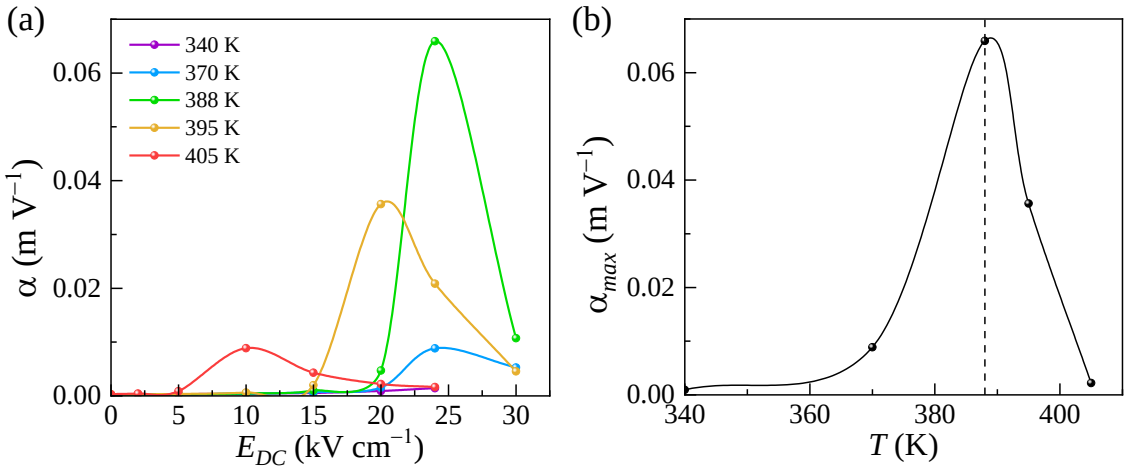

Figure 53: (a) Irreversible Rayleigh coefficient as a function of DC electric field at several temperatures. (b) Temperature dependence of the maximum irreversible Rayleigh coefficient.

Furthermore, PFM measurements were performed at 333 K and 388 K and are depicted in Figure 54. At 333 K, a classical AFE−FE first-order phase transition occurs. Ferroelectric domain structures emerge in the region where a DC voltage of 70 V was applied locally to the sample surface. The micrometer-sized lamellar domains are highlighted in the insets of the panel (a) in Figure 54 (blue arrows). On the other hand, 388 K corresponds to the triple point temperature. The amplitude and phase of the PFM response exhibit a nanodomain pattern. Despite the application of a 140 V DC voltage, twice the previously applied value, micro-sized domains are not formed. The sub-micro-sized irregularly shaped domain pattern (marked by white arrows in Figure 54b) resembles a relaxor-like nanodomain response previously observed in relaxor materials by PFM [177,178]. While some rare lamellar domains were visible, they were small, sub-micron in size. The decrease in domain size from 333 to 388 K is apparent, indicating domain fragmentation. Consequently, the PFM findings align with the results from the Rayleigh analysis and additionally confirm the presence of the electric field-induced nanodomains at the triple point in the antiferroelectric PNZST ceramics.

The presence of a critical end point significantly increased recoverable energy storage density and dielectric tunability under a low AC measurement signal. Studying the dielectric response under higher AC signals gave further insight into the origin of the enhanced dielectric tunability, which is attributed to the minimization of domains near the field-induced triple point, as shown by Rayleigh analysis and PFM imaging. This confirms that criticality is an effective route to enhance both the dielectric response of an antiferroelectric material and its functional properties.

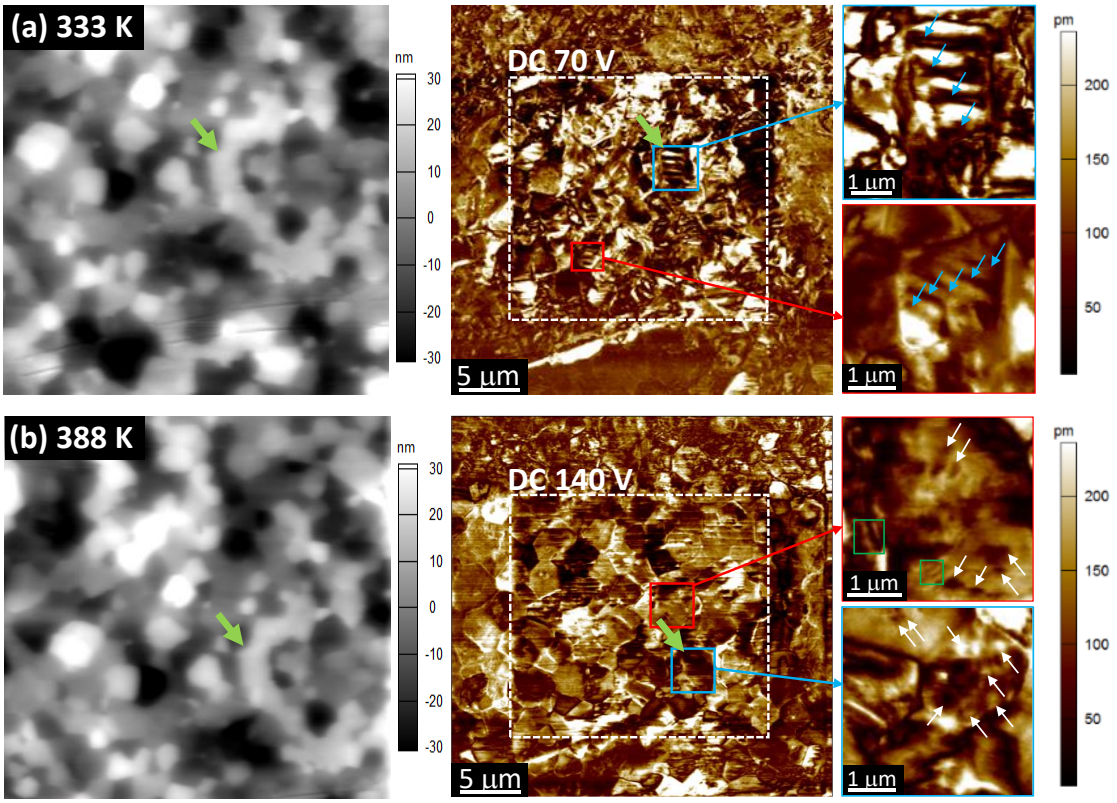

Figure 54: AFM topography and PFM out-of-plane amplitude images were scanned at (a) 333 K and (b) 388 K. The green arrow in the AFM and PFM images points to the same area. White dashed squares indicate regions where DC electric fields were previously applied. Insets within (a) and (b) display PFM amplitude images of smaller areas denoted by blue and red solid squares. The blue solid square represents the same measurement area. Micrometer-large lamellar domains are highlighted by blue arrows in the insets of panel (a). Sub-micron-sized irregularly shaped domains and sub-micron-sized lamellar domains are marked by white arrows and green squares, respectively, in the insets of panel (b).

Chapter 9

Conclusions

Accurate control of material properties through various procedures and modifications, as well as an understanding of the processes that govern dielectric response, enables tailoring material properties and constructing more reliable, high-performance materials. Thus, the separation and characterization of the various contributions to the dielectric response are of great importance in the development of novel, highly responsive dielectric materials.

This dissertation presents three different approaches to enhance the dielectric response of novel materials and, consequently, improve their dielectric and electromechanical properties. This chapter summarizes the data obtained through dielectric measurements for each of the investigated systems.

Composite approach: Cellulose/MXene composites
The first investigated system was developed using a composite approach: flexible cellulose nanofibrils/MXene composite films were prepared by vacuum filtration or solvent casting, using either native or carboxylated cellulose nanofibrils and highly electrically and thermally conductive two-dimensional titanium carbide MXenes ($Ti_3C_2T_x$). Dielectric measurements over broad frequency and temperature ranges revealed the influence of the preparation method and type of nanofibrils on the overall dielectric response. While the intrinsic data at the highest frequencies were almost identical, the increase in both ε' and σ' at low frequencies and high temperatures was much more pronounced in solvent-casted than in vacuum-filtered samples, which suggests that solvent-casted samples contain a higher number of free space charges or other impurities. Since these charges increase dielectric losses and lower the threshold for dielectric breakdown, further investigation of the dielectric response was done on vacuum-filtered CNF/$Ti_3C_2T_x$ composite films. The number of space charges in the TEMPO-oxidized CNF-based samples was higher since many hydroxyl groups on the surface of CNF were replaced by highly hydrophilic and polar carboxylate groups after TEMPO-mediated oxidation of cellulose.

In all as-prepared samples, absorbed water strongly enhanced the dielectric permittivity and electrical conductivity at low frequencies. After drying at 375 K, low-frequency ε' and σ' decreased by orders of magnitude; however, they increased again when the sample was exposed to air moisture. The effect was less pronounced in composite samples: MXene sheets not only reduced the space for trapped water within the fibrils network but also lowered the amount of bound water due to $Ti_3C_2T_x$–CNF interactions. Moreover, water molecules that were absorbed into the free volume of the system and attached to cellulose polar groups via weak physical or stronger hydrogen bonds were involved in the molecular motions associated with two secondary dielectric relaxations, particularly in the noncooperative rotation of lateral groups that corresponded to the γ relaxation.

Although the large, two-dimensional MXene sheets formed hydrogen bonds with CNF surface groups in addition to electrostatic interactions, the dielectric response of the vacuum-filtered CNF/$Ti_3C_2T_x$ films resembled that of a percolative composite with randomly distributed metallic regions within a dielectric matrix. The effective AC electrical conductivity increased with frequency, rising from the low-frequency plateau, corresponding to the conductivity of the matrix, toward the high-frequency plateau, which reflects the conductivity of the MXene. The dependence of σ' on MXene content follows the predictions of percolation theory reasonably well. Accordingly, the dielectric permittivity increased strongly with increasing MXene content, demonstrating that the properties of the CNF/$Ti_3C_2T_x$ composite can be tuned via percolation. These results indicate the potential of MXene/cellulose composites for eco-friendly dielectric and piezoelectric applications, where enhanced dielectric permittivity enables stronger electromechanical coupling at lower electric fields.

Operation at high electric fields: Poly(ether imide)/polyimide

For the second investigated system, blends of poly(ether imide) (PEI) and polyimide (PI) were synthesized by the solution casting method. The dielectric response was measured over broad frequency and temperature ranges and was compared with that of the pristine polymers. Although the intrinsic dielectric permittivity decreased only slightly, the electrical conductivity of the blends was approximately half the value of both PEI and PI. Since the phenyl groups in PI have a stronger positive charge compared to the negatively charged groups in PEI, the minimum values were observed not in the PEI/50PI blend but in the PEI/80PI blend. The dependence of both ε' and σ' on PI content was identical across the 180–360 K temperature range. At higher frequencies, the dielectric response was governed mainly by intrinsic dipole moments, whereas at lower frequencies, it was dictated predominantly by mobile space charges, whose contribution became more pronounced at elevated temperatures. Comparison of the temperature-dependent low-frequency data in the blends and pristine polymers, as well as their frequency-dependent response at the highest measurement temperatures, revealed a significant reduction in accumulated space charges in the blend systems.

Additional dielectric contributions were detected during the investigation. The aging process, often associated with the drift of free charge carriers, reduced the permittivity by less than 1.5 %. The activation energy of the γ relaxation, which originated from localized motions of rigid segments along the polymer backbone, was almost identical in the pristine and blend samples, indicating that electrostatic interactions between the charged PEI and PI phenyl groups did not significantly influence the molecular motions underlying this relaxation. However, since these molecular motions involved water molecules, the γ relaxation was not observed in samples that had been heated to 400 K prior to measurement. Due to the notable influence of absorbed water on the overall dielectric response, the impact of high-temperature annealing on the dielectric breakdown strength was also examined. Unannealed blends exhibited approximately 2.5 times higher E_b values than pristine PEI and PI. Annealing at 400 K for 1 hour before measurement significantly increased the breakdown strength of the pristine polymers, whereas values in the blend systems remained almost unchanged. This outcome was attributed to a much higher chain packing density in the blend systems and, consequently, a lower amount of absorbed water molecules.

Strong electrostatic interactions between phenyl groups of different polymer chains indeed resulted in (i) fewer space charges and (ii) higher chain packing density in PEI/PI blends compared to the pristine polymers. Because dielectric breakdown is initiated by

charges accelerated by an applied electric field at weak points (i.e., voids in the system), both features contributed to the enhancement of E_b. Thus, blending appropriately matched polymers proved to be an effective strategy for improving dielectric properties of polymer systems, especially enhancing the dielectric breakdown strength.

Physical approach – induction of criticality: Antiferroelectric PNZST ceramics
The third approach employed existing knowledge on enhancing functional properties by inducing a critical end point in a ferroelectric (FE) system and applied it to an antiferroelectric (AFE) one. The FE–AFE and AFE–PE phase transitions in PNZST ceramics were investigated by measuring the dielectric response under different external DC electric fields. It was observed that the first-order transition lines of the FE–AFE and AFE–PE phase transitions terminate at two separate critical end points. The location of the FE–AFE critical end point was determined to be at 21 kV cm^{-1} and 370 K, while the AFE–PE critical end point was located at 21 kV cm^{-1} and 396 K. Above these critical end points, the dielectric response exhibited supercritical behavior, and at 25 kV cm^{-1} and 388 K, the transitions merged.

The recoverable energy storage density is defined by the relation between the maximum polarization and the electric field of the FE–AFE phase transition. The optimal ratio between these two parameters was achieved at the FE–AFE critical end point, resulting in the best material performance. Furthermore, the strong enhancement of dielectric tunability was attributed to the proximity of the AFE–PE critical end point at a 1 V AC probing signal. It was suggested that the combination of flattening of the free energy potential at the critical end point and the degeneracy of the AFE and PE phases was responsible for the enhanced dielectric response.

The mechanism behind the dielectric enhancement under a bias electric field in the antiferroelectric phase of PNZST ceramics was further investigated through in-situ dielectric and thermal measurements, Rayleigh-type analysis, and piezoresponse force microscopy. The observed increase in dielectric permittivity with increasing electric field was attributed to enhanced nonlinear processes, most likely due to domain wall displacements. This was corroborated by the Rayleigh analysis, which revealed an increased irreversible contribution in the vicinity of the AFE–FE phase transition. The maximum dielectric tunability shifted from the temperature of the FE–AFE critical end point (measured with a 1 V AC signal) to the field-induced triple point temperature (measured with a 20 V AC signal), while the dielectric tunability increased from approximately 220 to 375 %. This exceptionally high tunability near the triple point was attributed to the minimization of domain size, as revealed by PFM imaging, and to a corresponding increase in irreversible domain wall contributions to the dielectric permittivity. These results suggest that tailoring domain structures is a successful strategy for tuning the functional properties of not only ferroelectric but also antiferroelectric ceramics. Moreover, it was demonstrated that criticality, i.e., the presence of a critical end point, can be extended to antiferroelectric systems and represents a promising approach for enhancing their functional properties.

Graphical Summary

Composite approach

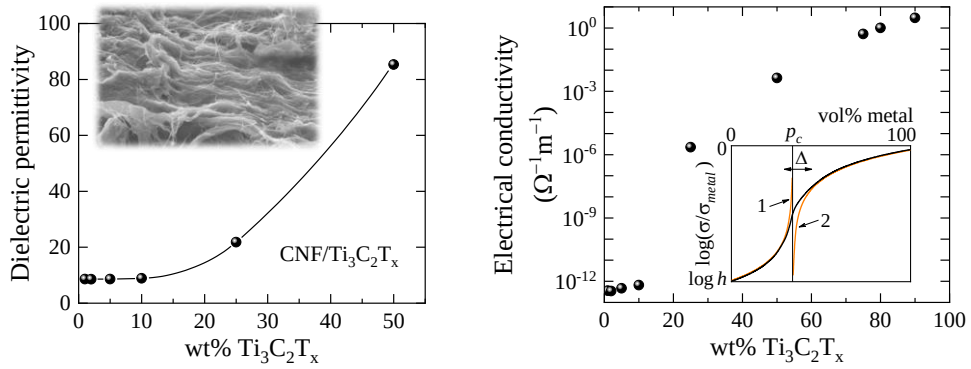

In composites made of cellulose nanofibrils and highly electrically conductive titanium carbide MXenes, the dielectric response follows the predictions of percolation theory, i.e., it increases strongly with increasing filler volume content. *(V. Jurečič et al., APL Materials (2024) 12(11): 111102)*

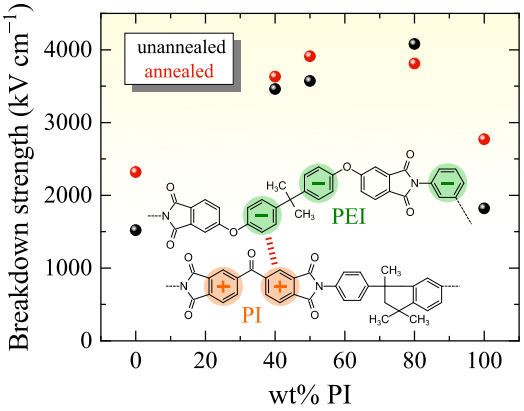

Operation at high electric fields

Electrostatic interactions between the oppositely charged phenyl groups of PEI and PI polymer chains reduce the number of space charges and lead to a much higher chain packing density, thereby significantly enhancing the dielectric breakdown strength in PEI/PI blends. *(V. Jurečič et al., Macromolecules (2023) 56(3): 1097–1104)*

Physical approach

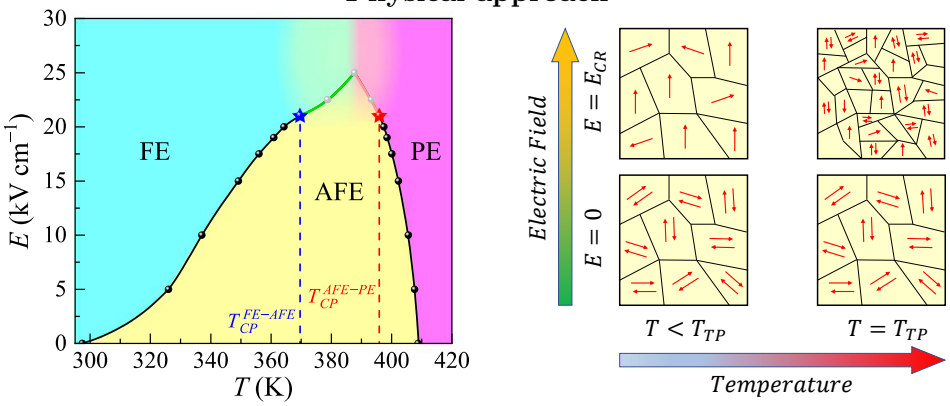

The electric field–temperature phase diagram of antiferroelectric PNZST ceramics exhibits first-order FE–AFE and AFE–PE transition lines, each terminating at a critical end point. The presence of a critical end point enhances functional properties such as energy storage density and dielectric tunability. *(V. Jurečič et al., Physical Review Materials (2023) 7(11): 114407)* Minimization of domain size was proposed as the mechanism responsible for the enhanced dielectric tunability (≈375 %) at the temperature of the field-induced triple point. *(V. Jurečič et al., Advanced Functional Materials (2025) 35(2): 2412739)*

References

[1] M. Rabuffi and G. Picci, "Status quo and future prospects for metallized polypropylene energy storage capacitors," *IEEE Trans. Plasma Sci.*, vol. 30, no. 5, pp. 1939–1942, Oct. 2002, doi: 10.1109/TPS.2002.805318.

[2] B. Chu *et al.*, "A dielectric polymer with high electric energy density and fast discharge speed," *Science*, vol. 313, no. 5785, pp. 334–336, Jul. 2006, doi: 10.1126/science.1127798.

[3] P. Kim *et al.*, "High energy density nanocomposites based on surface-modified $BaTiO_3$ and a ferroelectric polymer," *ACS Nano*, vol. 3, no. 9, pp. 2581–2592, Sep. 2009, doi: 10.1021/nn9006412.

[4] J. Lu and C. P. Wong, "Recent advances in high-k nanocomposite materials for embedded capacitor applications," *IEEE Trans. Dielectr. Electr. Insul.*, vol. 15, no. 5, pp. 1322–1328, Oct. 2008, doi: 10.1109/TDEI.2008.4656240.

[5] M. Mohiuddin, K. Kumar Sadasivuni, S. Mun, and J. Kim, "Flexible cellulose acetate/graphene blueprints for vibrotactile actuator," *RSC Adv.*, vol. 5, no. 43, pp. 34432–34438, 2015, doi: 10.1039/C5RA03043A.

[6] S. Wang *et al.*, "Polymer-based dielectrics with high permittivity and low dielectric loss for flexible electronics," *J. Mater. Chem. C*, vol. 10, no. 16, pp. 6196–6221, 2022, doi: 10.1039/D2TC00193D.

[7] S. Sun, Z. Wang, and Y. Wang, "Progress in microtopography optimization of polymers-based pressure/strain sensors," *Polymers*, vol. 15, no. 3, Art. no. 3, Jan. 2023, doi: 10.3390/polym15030764.

[8] C. Huang, Q. M. Zhang, and J. Su, "High-dielectric-constant all-polymer percolative composites," *Appl. Phys. Lett.*, vol. 82, no. 20, pp. 3502–3504, May 2003, doi: 10.1063/1.1575505.

[9] B. Chu and Y. Zhou, "Energy storage properties of PVDF terpolymer/PMMA blends," *High Volt.*, vol. 1, no. 4, pp. 171–174, 2016, doi: 10.1049/hve.2016.0062.

[10] X. Zhang, Y. Shen, Z. Shen, J. Jiang, L. Chen, and C.-W. Nan, "Achieving high energy density in PVDF-based polymer blends: suppression of early polarization saturation and enhancement of breakdown strength," *ACS Appl. Mater. Interfaces*, vol. 8, no. 40, pp. 27236–27242, Oct. 2016, doi: 10.1021/acsami.6b10016.

[11] Q. Chi *et al.*, "A blended binary composite of poly(vinylidene fluoride) and poly(methyl methacrylate) exhibiting excellent energy storage performances," *J. Mater. Chem. C*, vol. 7, no. 45, pp. 14148–14158, 2019, doi: 10.1039/C9TC04695J.

[12] Q. Zhang *et al.*, "High-temperature polymers with record-high breakdown strength enabled by rationally designed chain-packing behavior in blends," *Matter*, vol. 4, no. 7, pp. 2448–2459, Jul. 2021, doi: 10.1016/j.matt.2021.04.026.

[13] K. Liu *et al.*, "Realizing enhanced energy density in ternary polymer blends by intermolecular structure design," *Chem. Eng. J.*, vol. 446, p. 136980, Oct. 2022, doi: 10.1016/j.cej.2022.136980.

[14] M. Jian, Y. Zhang, and Z. Liu, "Natural biopolymers for flexible sensing and energy devices," *Chin. J. Polym. Sci.*, vol. 38, no. 5, pp. 459–490, May 2020, doi: 10.1007/s10118-020-2379-9.

[15] W. Li *et al.*, "Biodegradable materials and green processing for green electronics," *Adv. Mater.*, vol. 32, no. 33, p. 2001591, 2020, doi: 10.1002/adma.202001591.

[16] H. Xiang, Z. Li, H. Liu, T. Chen, H. Zhou, and W. Huang, "Green flexible electronics based on starch," *Npj Flex. Electron.*, vol. 6, Art. no. 15, Mar. 2022, doi: 10.1038/s41528-022-00147-x.

[17] J.-X. Feng, S.-H. Ye, A.-L. Wang, X.-F. Lu, Y.-X. Tong, and G.-R. Li, "Flexible cellulose paper-based asymmetrical thin film supercapacitors with high-performance for electrochemical energy storage," *Adv. Funct. Mater.*, vol. 24, no. 45, pp. 7093–7101, 2014, doi: 10.1002/adfm.201401876.

[18] A. Kafy, K. Kumar Sadasivuni, H.-C. Kim, A. Akther, and J. Kim, "Designing flexible energy and memory storage materials using cellulose modified graphene oxide nanocomposites," *Phys. Chem. Chem. Phys.*, vol. 17, no. 8, pp. 5923–5931, 2015, doi: 10.1039/C4CP05921B.

[19] P. T. Y. Beeran *et al.*, "Mechanically strong, flexible and thermally stable graphene oxide/nanocellulosic films with enhanced dielectric properties," *RSC Adv.*, vol. 6, no. 54, pp. 49138–49149, May 2016, doi: 10.1039/C6RA06744A.

[20] S. Pei and H.-M. Cheng, "The reduction of graphene oxide," *Carbon*, vol. 50, no. 9, pp. 3210–3228, Aug. 2012, doi: 10.1016/j.carbon.2011.11.010.

[21] N. Ning, Q. Ma, S. Liu, M. Tian, L. Zhang, and T. Nishi, "Tailoring dielectric and actuated properties of elastomer composites by bioinspired poly(dopamine) encapsulated graphene oxide," *ACS Appl. Mater. Interfaces*, vol. 7, no. 20, pp. 10755–10762, May 2015, doi: 10.1021/acsami.5b00808.

[22] K. Yuan *et al.*, "Nanofibrous and graphene-templated conjugated microporous polymer materials for flexible chemosensors and supercapacitors," *Chem. Mater.*, vol. 27, no. 21, pp. 7403–7411, Nov. 2015, doi: 10.1021/acs.chemmater.5b03290.

[23] Y. B. Pottathara *et al.*, "UV-induced reduction of graphene oxide in cellulose nanofibril composites," *New J. Chem.*, vol. 43, no. 2, pp. 681–688, 2019, doi: 10.1039/C8NJ03563F.

[24] W. Yu, L. Sisi, Y. Haiyan, and L. Jie, "Progress in the functional modification of graphene/graphene oxide: a review," *RSC Adv.*, vol. 10, no. 26, pp. 15328–15345, 2020, doi: 10.1039/D0RA01068E.

[25] Y. B. Pottathara, V. Bobnar, Y. Grohens, S. Thomas, R. Kargl, and V. Kokol, "High dielectric thin films based on UV-reduced graphene oxide and TEMPO-

oxidized cellulose nanofibres," *Cellulose*, vol. 28, no. 5, pp. 3069–3080, Mar. 2021, doi: 10.1007/s10570-021-03701-4.

[26] A. Razaq, F. Bibi, X. Zheng, R. Papadakis, S. H. M. Jafri, and H. Li, "Review on graphene-, graphene oxide-, reduced graphene oxide-based flexible composites: from fabrication to applications," *Materials*, vol. 15, no. 3, Art. no. 1012, Jan. 2022, doi: 10.3390/ma15031012.

[27] X. Jiang *et al.*, "Two-dimensional MXenes: From morphological to optical, electric, and magnetic properties and applications," *Phys. Rep.*, vol. 848, pp. 1–58, Mar. 2020, doi: 10.1016/j.physrep.2019.12.006.

[28] A. S. Zeraati, S. Alireza Mirkhani, P. Sun, M. Naguib, P. V. Braun, and U. Sundararaj, "Improved synthesis of $Ti_3C_2T_x$ MXenes resulting in exceptional electrical conductivity, high synthesis yield, and enhanced capacitance," *Nanoscale*, vol. 13, no. 6, pp. 3572–3580, 2021, doi: 10.1039/D0NR06671K.

[29] A. Eršte *et al.*, "Stable dielectric response of low-loss aromatic polythiourea thin films on Pt/SiO_2 substrate," *J. Adv. Dielectr.*, vol. 06, no. 1, Art. no. 1650003, Mar. 2016, doi: 10.1142/S2010135X1650003X.

[30] C. Wu, X. Huang, X. Wu, L. Xie, K. Yang, and P. Jiang, "Graphene oxide-encapsulated carbon nanotube hybrids for high dielectric performance nanocomposites with enhanced energy storage density," *Nanoscale*, vol. 5, no. 9, pp. 3847–3855, 2013, doi: 10.1039/C3NR00625E.

[31] D. Berlincourt, H. H. A. Krueger, and B. Jaffe, "Stability of phases in modified lead zirconate with variation in pressure, electric field, temperature and composition," *J. Phys. Chem. Solids*, vol. 25, no. 7, pp. 659–674, Jul. 1964, doi: 10.1016/0022-3697(64)90175-1.

[32] X. Hao, J. Zhai, L. B. Kong, and Z. Xu, "A comprehensive review on the progress of lead zirconate-based antiferroelectric materials," *Prog. Mater. Sci.*, vol. 63, pp. 1–57, Jun. 2014, doi: 10.1016/j.pmatsci.2014.01.002.

[33] K. Markowski, S.-E. Park, S. Yoshikawa, and L. E. Cross, "Effect of compositional variations in the lead lanthanum zirconate stannate titanate system on electrical properties," *J. Am. Ceram. Soc.*, vol. 79, no. 12, pp. 3297–3304, 1996, doi: 10.1111/j.1151-2916.1996.tb08108.x.

[34] B. Xu, Y. Ye, Q.-M. Wang, N. G. Pai, and L. E. Cross, "Effect of compositional variations on electrical properties in phase switching $(Pb,La)(Zr,Ti,Sn)O_3$ thin and thick films," *J. Mater. Sci.*, vol. 35, no. 23, pp. 6027–6033, Dec. 2000, doi: 10.1023/A:1026775701354.

[35] Y. J. Feng, Z. Xu, and X. Yao, "Effect of Sn doping on the phase transition behaviors of antiferroelectric lead zirconate titanate," *Mater. Sci. Eng. B*, vol. 99, no. 1, pp. 499–501, May 2003, doi: 10.1016/S0921-5107(02)00513-5.

[36] H. He and X. Tan, "Electric-field-induced transformation of incommensurate modulations in antiferroelectric $Pb_{0.99}Nb_{0.02}[(Zr_{1-x}Sn_x)_{1-y}Ti_y]_{0.98}O_3$," *Phys. Rev. B*, vol. 72, no. 2, Art. no. 024102, Jul. 2005, doi: 10.1103/PhysRevB.72.024102.

[37] J. Frederick, X. Tan, and W. Jo, "Strains and polarization during antiferroelectric–ferroelectric phase switching in $Pb_{0.99}Nb_{0.02}[(Zr_{0.57}Sn_{0.43})_{1-y}Ti_y]_{0.98}O_3$ ceramics," *J. Am.*

Ceram. Soc., vol. 94, no. 4, pp. 1149–1155, 2011, doi: 10.1111/j.1551-2916.2010.04194.x.

[38] S. Chen, X. Wang, T. Yang, and J. Wang, "Composition-dependent dielectric properties and energy storage performance of (Pb,La)(Zr,Sn,Ti)O_3 antiferroelectric ceramics," *J. Electroceramics*, vol. 32, no. 4, pp. 307–310, Jun. 2014, doi: 10.1007/s10832-014-9900-x.

[39] D. Damjanovic, "Ferroelectric, dielectric and piezoelectric properties of ferroelectric thin films and ceramics," *Rep. Prog. Phys.*, vol. 61, no. 9, pp. 1267–1324, Sep. 1998, doi: 10.1088/0034-4885/61/9/002.

[40] S. Hoffmann-Eifert, D. Richter, and S. Trolier-McKinstry, "Dielectric, ferroelectric, and optical properties," in *Nanoelectronics and Information Technology: Advanced Electronic Materials and Novel Devices*, 3rd ed., R. Waser, Ed. Weinheim, Wiley-VCH, 2012, pp. 33–62.

[41] C. A. Randall, Z. Fan, I. Reaney, L.-Q. Chen, and S. Trolier-McKinstry, "Antiferroelectrics: History, fundamentals, crystal chemistry, crystal structures, size effects, and applications," *J. Am. Ceram. Soc.*, vol. 104, no. 8, pp. 3775–3810, 2021, doi: 10.1111/jace.17834.

[42] N. Bassiri-Gharb, I. Fujii, E. Hong, S. Trolier-McKinstry, D. V. Taylor, and D. Damjanovic, "Domain wall contributions to the properties of piezoelectric thin films," *J. Electroceramics*, vol. 19, no. 1, pp. 49–67, Sep. 2007, doi: 10.1007/s10832-007-9001-1.

[43] D. A. Hall, "Review Nonlinearity in piezoelectric ceramics," *J. Mater. Sci.*, vol. 36, no. 19, pp. 4575–4601, Oct. 2001, doi: 10.1023/A:1017959111402.

[44] H. Dederichs and G. Arlt, "Aging of Fe-doped PZT ceramics and the domain wall contribution to the dielectric constant," *Ferroelectrics*, vol. 68, no. 1, pp. 281–292, Jan. 1986, doi: 10.1080/00150198608238758.

[45] D. A. Hall and M. M. Ben-Omran, "Ageing of high field dielectric properties in $BaTiO_3$-based piezoceramics," *J. Phys. Condens. Matter*, vol. 10, no. 40, Art. no. 9129, Oct. 1998, doi: 10.1088/0953-8984/10/40/016.

[46] J. M. Worlock and P. A. Fleury, "Electric field dependence of optical-phonon frequencies," *Phys. Rev. Lett.*, vol. 19, no. 20, pp. 1176–1179, Nov. 1967, doi: 10.1103/PhysRevLett.19.1176.

[47] W. D. Callister and D. G. Rethwisch, *Materials Science and Engineering: An Introduction*, 8th ed. Hoboken, NJ, USA: John Wiley & Sons, 2010.

[48] N. Novak, R. Pirc, and Z. Kutnjak, "Impact of critical point on piezoelectric and electrocaloric response in barium titanate," *Phys. Rev. B*, vol. 87, no. 10, Art. no. 104102, Mar. 2013, doi: 10.1103/PhysRevB.87.104102.

[49] Z. Kutnjak, J. Petzelt, and R. Blinc, "The giant electromechanical response in ferroelectric relaxors as a critical phenomenon," *Nature*, vol. 441, no. 7096, Art. no. 7096, Jun. 2006, doi: 10.1038/nature04854.

[50] M. Porta, T. Lookman, and A. Saxena, "Effects of criticality and disorder on piezoelectric properties of ferroelectrics," *J. Phys. Condens. Matter*, vol. 22, no. 34, Art. no. 345902, Aug. 2010, doi: 10.1088/0953-8984/22/34/345902.

[51] F. Weyland, M. Acosta, J. Koruza, P. Breckner, J. Rödel, and N. Novak, "Criticality: Concept to enhance the piezoelectric and electrocaloric properties of ferroelectrics," *Adv. Funct. Mater.*, vol. 26, no. 40, pp. 7326–7333, Sep. 2016, doi: 10.1002/adfm.201602368.

[52] L. Zhao, Q. Liu, J. Gao, S. Zhang, and J.-F. Li, "Lead-free antiferroelectric silver niobate tantalate with high energy storage performance," *Adv. Mater.*, vol. 29, no. 31, Art. no. 1701824, 2017, doi: 10.1002/adma.201701824.

[53] G. A. Samara and E. L. and Venturini, "Ferroelectric/relaxor crossover in compositionally disordered perovskites," *Phase Transit.*, vol. 79, no. 1–2, pp. 21–40, Jan. 2006, doi: 10.1080/01411590500418331.

[54] L. B. Kong, S. Li, T. S. Zhang, J. W. Zhai, F. Y. C. Boey, and J. Ma, "Electrically tunable dielectric materials and strategies to improve their performances," *Prog. Mater. Sci.*, vol. 55, no. 8, pp. 840–893, Nov. 2010, doi: 10.1016/j.pmatsci.2010.04.004.

[55] B. Su and T. W. Button, "The processing and properties of barium strontium titanate thick films for use in frequency agile microwave circuit applications," *J. Eur. Ceram. Soc.*, vol. 21, no. 15, pp. 2641–2645, Jan. 2001, doi: 10.1016/S0955-2219(01)00330-2.

[56] M. E. Lines and A. M. Glass, *Principles and Applications of Ferroelectrics and Related Materials*. Oxford, U.K.: Oxford. Univ. Press, 2001.

[57] R. Whatmore, "Ferroelectric Materials," in *Springer Handbook of Electronic and Photonic Materials*, S. Kasap and P. Capper, Eds. Cham: Springer International Publishing, 2017, pp. 597–623. doi: 10.1007/978-3-319-48933-9_26.

[58] F. Li *et al.*, "Giant piezoelectricity of Sm-doped $Pb(Mg_{1/3}Nb_{2/3})O_3$-$PbTiO_3$ single crystals," *Science*, vol. 364, no. 6437, pp. 264–268, Apr. 2019, doi: 10.1126/science.aaw2781.

[59] B. Jaffe, R. S. Roth, and S. Marzullo, "Piezoelectric properties of lead zirconate-lead titanate solid-solution ceramics," *J. Appl. Phys.*, vol. 25, no. 6, pp. 809–810, 1954, doi: 10.1063/1.1721741.

[60] M. Ahart *et al.*, "Origin of morphotropic phase boundaries in ferroelectrics," *Nature*, vol. 451, no. 7178, Art. no. 7178, Jan. 2008, doi: 10.1038/nature06459.

[61] C. Zhao *et al.*, "Precipitation hardening in ferroelectric ceramics," *Adv. Mater.*, vol. 33, no. 36, Art. no. 2102421, 2021, doi: 10.1002/adma.202102421.

[62] L. M. Riemer *et al.*, "Stress-induced phase transition in lead-free relaxor ferroelectric composites," *Acta Mater.*, vol. 136, pp. 271–280, Sep. 2017, doi: 10.1016/j.actamat.2017.07.008.

[63] B. Jaffe, W. R. Cook, and H. Jaffe, *Piezoelectric Ceramics*. London, U.K.: Academic Press, 1971.

[64] S. Trolier-McKinstry, S. Zhang, A. J. Bell, and X. Tan, "High-performance piezoelectric crystals, ceramics, and films," *Annu. Rev. Mater. Res.*, vol. 48, pp. 191–217, Jul. 2018, doi: 10.1146/annurev-matsci-070616-124023.

[65] E. V. Colla, N. K. Yushin, and D. Viehland, "Dielectric properties of $(PMN)_{(1-x)}(PT)_x$ single crystals for various electrical and thermal histories," *J. Appl. Phys.*, vol. 83, no. 6, pp. 3298–3304, Mar. 1998, doi: 10.1063/1.367098.

[66] M. Iwata, K. Tanaka, M. Maeda, and Y. Ishibashi, "Dielectric tunability near critical end point in $Pb(Zn_{1/3}Nb_{2/3})O_3$–$PbTiO_3$," *Jpn. J. Appl. Phys.*, vol. 53, no. 3, Art. no. 038004, Feb. 2014, doi: 10.7567/JJAP.53.038004.

[67] E. Sawaguchi, H. Maniwa, and S. Hoshino, "Antiferroelectric structure of lead zirconate," *Phys. Rev.*, vol. 83, no. 5, Art. no. 1078, Sep. 1951, doi: 10.1103/PhysRev.83.1078.

[68] K. M. Rabe, "Antiferroelectricity in oxides: A reexamination," in *Functional Metal Oxides: New Science and Novel Applications*, 1st ed., S. B. Ogale, T. V. Venkatesan, and M. G. Blamire, Eds. Weinheim, Germany: Wiley-VCH, 2013, pp. 221–244. doi: 10.1002/9783527654864.ch7.

[69] C. Kittel, "Theory of antiferroelectric crystals," *Phys. Rev.*, vol. 82, no. 5, pp. 729–732, Jun. 1951, doi: 10.1103/PhysRev.82.729.

[70] I. MacLaren, R. Villaurrutia, B. Schaffer, L. Houben, and A. Peláiz-Barranco, "Atomic-scale imaging and quantification of electrical polarisation in incommensurate antiferroelectric lanthanum-doped lead zirconate titanate," *Adv. Funct. Mater.*, vol. 22, no. 2, pp. 261–266, 2012, doi: 10.1002/adfm.201101220.

[71] H. Liu *et al.*, "Electric-field-induced structure and domain texture evolution in $PbZrO_3$-based antiferroelectric by in-situ high-energy synchrotron X-ray diffraction," *Acta Mater.*, vol. 184, pp. 41–49, Feb. 2020, doi: 10.1016/j.actamat.2019.11.050.

[72] M. Hoffmann *et al.*, "Antiferroelectric negative capacitance from a structural phase transition in zirconia," *Nat. Commun.*, vol. 13, no. 1, Art. no. 1, Mar. 2022, doi: 10.1038/s41467-022-28860-1.

[73] L. Li, M. Spreitzer, D. Suvorov, and X. M. Chen, "Unique dielectric tunability of $Pb_{0.99}[(Zr_{0.6}Sn_{0.4})_{0.94}Ti_{0.06}]_{0.98}Nb_{0.02}O_3$ antiferroelectric ceramics," *J. Appl. Phys.*, vol. 120, no. 7, Art. no. 074109, Aug. 2016, doi: 10.1063/1.4961424.

[74] R. Pirc, B. Rožič, J. Koruza, B. Malič, and Z. Kutnjak, "Negative electrocaloric effect in antiferroelectric $PbZrO_3$," *Europhys. Lett.*, vol. 107, no. 1, Art. no. 17002, Jul. 2014, doi: 10.1209/0295-5075/107/17002.

[75] P. D. Thacher, "Electrocaloric effects in some ferroelectric and antiferroelectric Pb(Zr, Ti)O_3 compounds," *J. Appl. Phys.*, vol. 39, no. 4, pp. 1996–2002, 1968, doi: 10.1063/1.1656478.

[76] R. Pirc, B. Rožič, J. Koruza, G. Cordoyiannis, B. Malič, and Z. Kutnjak, "Anomalous dielectric and thermal properties of Ba-doped $PbZrO_3$ ceramics," *J. Phys. Condens. Matter*, vol. 27, no. 45, Art. no. 455902, Oct. 2015, doi: 10.1088/0953-8984/27/45/455902.

[77] W. Geng *et al.*, "Giant negative electrocaloric effect in antiferroelectric La-doped $Pb(ZrTi)O_3$ thin films near room temperature," *Adv. Mater.*, vol. 27, no. 20, pp. 3165–3169, 2015, doi: 10.1002/adma.201501100.

[78] B. Jaffe, "Antiferroelectric ceramics with field-enforced transitions: A new nonlinear circuit element," *Proc. IRE*, vol. 49, no. 8, pp. 1264–1267, Aug. 1961, doi: 10.1109/JRPROC.1961.287917.

[79] J. Wang, T. Yang, S. Chen, X. Yao, and A. Peláiz-Barranco, "DC electric field dependence for the dielectric permittivity in antiferroelectric and ferroelectric states," *J. Alloys Compd.*, vol. 587, pp. 827–829, Feb. 2014, doi: 10.1016/j.jallcom.2013.10.251.

[80] Y. Feng, X. Wei, D. Wang, Z. Xu, and X. Yao, "Dielectric behaviors of antiferroelectric–ferroelectric transition under electric field," *Ceram. Int.*, vol. 30, no. 7, pp. 1389–1392, Jan. 2004, doi: 10.1016/j.ceramint.2003.12.090.

[81] X. Tan, C. Ma, J. Frederick, S. Beckman, and K. G. Webber, "The antiferroelectric ↔ ferroelectric phase transition in lead-containing and lead-free perovskite ceramics," *J. Am. Ceram. Soc.*, vol. 94, no. 12, pp. 4091–4107, 2011, doi: 10.1111/j.1551-2916.2011.04917.x.

[82] J. P. Dougherty, "Cardiac defibrillator with high energy storage antiferroelectric capacitor," US5545184A, Aug. 13, 1996 Accessed: May 12, 2023. [Online]. Available: https://patents.google.com/patent/US5545184A/en

[83] K. Reichmann and T. Kainz, "Antiferroelectrics: Materials for new ceramic power devices," in *50th International Conference on Microelectronics, Materials and Devices*, M. Topič, I. Šorli, and P. Šorli, Eds. Ljubljana, Slovenia: MIDEM - Society for Microelectronics, Electronic Components and Materials, 2014.

[84] K. Uchino, "Antiferroelectric shape memory ceramics," *Actuators*, vol. 5, no. 2, Art. no. 2, Jun. 2016, doi: 10.3390/act5020011.

[85] M. M. Vopson and X. Tan, "Four-state anti-ferroelectric random access memory," *IEEE Electron Device Lett.*, vol. 37, no. 12, pp. 1551–1554, Dec. 2016, doi: 10.1109/LED.2016.2614841.

[86] D. H. Morris, U. E. Avci, and I. A. Young, "Anti-ferroelectric capacitor memory cell," EP3576092B1, Dec. 23, 2020 Accessed: May 12, 2023. [Online]. Available: https://patents.google.com/patent/EP3576092B1/en?q=(Anti-ferroelectric+capacitor+memory+cell)

[87] G. Shirane, E. Sawaguchi, and Y. Takagi, "Dielectric properties of lead zirconate," *Phys. Rev.*, vol. 84, no. 3, pp. 476–481, Nov. 1951, doi: 10.1103/PhysRev.84.476.

[88] K. H. Yoon, S. C. Hwang, and D. H. Kang, "Dielectric and field-induced strain behaviour of $(Pb_{1-x}Ba_x)$ ZrO_3 ceramics," *J. Mater. Sci.*, vol. 32, no. 1, pp. 17–21, Jan. 1997, doi: 10.1023/A:1018654423330.

[89] V. M. Ishchuk, S. V. Matveev, and V. L. Sobolev, "Two-phase (ferroelectric and antiferroelectric) nuclei and diffuse phase transition in the vicinity of the ferroelectric–antiferroelectric–paraelectric triple point," *Appl. Phys. Lett.*, vol. 79, no. 18, pp. 2949–2951, Oct. 2001, doi: 10.1063/1.1414300.

[90] P. Liu and X. Yao, "Dielectric properties and phase transitions of $(Pb_{0.87}La_{0.02}Ba_{0.1})(Zr_{0.6}Sn_{0.4-x}Ti_x)O_3$ ceramics with compositions near AFE/RFE phase boundary," *Solid State Commun.*, vol. 132, no. 12, pp. 809–813, Dec. 2004, doi: 10.1016/j.ssc.2004.09.046.

[91] Z. Lu *et al.*, "Mechanism of enhanced energy storage density in $AgNbO_3$-based lead-free antiferroelectrics," *Nano Energy*, vol. 79, Art. no. 105423, Jan. 2021, doi: 10.1016/j.nanoen.2020.105423.

[92] M.-H. Zhang *et al.*, "Tailoring high-energy storage $NaNbO_3$-based materials from antiferroelectric to relaxor states," *Nat. Commun.*, vol. 14, no. 1, Art. no. 1, Mar. 2023, doi: 10.1038/s41467-023-37060-4.

[93] N. Luo *et al.*, "Silver stoichiometry engineering: an alternative way to improve energy storage density of $AgNbO_3$-based antiferroelectric ceramics," *J. Mater. Res.*, vol. 36, no. 5, pp. 1067–1075, Mar. 2021, doi: 10.1557/s43578-020-00018-z.

[94] M.-H. Zhang, L. Fulanović, C. Zhao, and J. Koruza, "Review on field-induced phase transitions in lead-free $NaNbO_3$-based antiferroelectric perovskite oxides for energy storage," *J. Materiomics*, vol. 9, no. 1, pp. 1–18, Jan. 2023, doi: 10.1016/j.jmat.2022.09.008.

[95] H. Shimizu, H. Guo, S. E. Reyes-Lillo, Y. Mizuno, K. M. Rabe, and C. A. Randall, "Lead-free antiferroelectric: $xCaZrO_3$-$(1-x)NaNbO_3$ system ($0 \leq x \leq 0.10$)," *Dalton Trans.*, vol. 44, no. 23, pp. 10763–10772, Jun. 2015, doi: 10.1039/C4DT03919J.

[96] M.-H. Zhang *et al.*, "Design of lead-free antiferroelectric $(1-x)NaNbO_3$–$xSrSnO_3$ compositions guided by first-principles calculations," *Chem. Mater.*, vol. 33, no. 1, pp. 266–274, Jan. 2021, doi: 10.1021/acs.chemmater.0c03685.

[97] N. Novak, R. Pirc, and Z. Kutnjak, "Diffuse critical point in PLZT ceramics," *Europhys. Lett.*, vol. 102, no. 1, Art. no. 17003, Apr. 2013, doi: 10.1209/0295-5075/102/17003.

[98] N. Novak *et al.*, "Interplay of conventional with inverse electrocaloric response in $(Pb,Nb)(Zr,Sn,Ti)O_3$ antiferroelectric materials," *Phys. Rev. B*, vol. 97, no. 9, Art. no. 094113, Mar. 2018, doi: 10.1103/PhysRevB.97.094113.

[99] H. He and X. Tan, "Electric-field-induced transformation of incommensurate modulations in antiferroelectric $Pb_{0.99}\,Nb_{0.02}\,[(Zr_{1-x}Sn_x)_{1-y}Ti_y]_{0.98}O_3$," *Phys. Rev. B*, vol. 72, no. 2, Art. no. 024102, Jul. 2005, doi: 10.1103/PhysRevB.72.024102.

[100] K. Uchino, L. E. Cross, R. E. Newnham, and S. Nomura, "Electrostrictive effects in antiferroelectric perovskites," *J. Appl. Phys.*, vol. 52, no. 3, pp. 1455–1459, Mar. 1981, doi: 10.1063/1.329780.

[101] S. Feng, B. I. Halperin, and P. N. Sen, "Transport properties of continuum systems near the percolation threshold," *Phys. Rev. B*, vol. 35, no. 1, pp. 197–214, Jan. 1987, doi: 10.1103/PhysRevB.35.197.

[102] A. L. Efros and B. I. Shklovskii, "Critical behaviour of conductivity and dielectric constant near the metal-non-metal transition threshold," *Phys. Status Solidi B*, vol. 76, no. 2, pp. 475–485, 1976, doi: 10.1002/pssb.2220760205.

[103] S. Kirkpatrick, "Percolation and conduction," *Rev. Mod. Phys.*, vol. 45, no. 4, pp. 574–588, Oct. 1973, doi: 10.1103/RevModPhys.45.574.

[104] D. J. Bergman and Y. Imry, "Critical behavior of the complex dielectric constant near the percolation threshold of a heterogeneous material," *Phys. Rev. Lett.*, vol. 39, no. 19, pp. 1222–1225, Nov. 1977, doi: 10.1103/PhysRevLett.39.1222.

[105] C. Pecharromán, F. Esteban-Betegón, J. F. Bartolomé, S. López-Esteban, and J. S. Moya, "New percolative $BaTiO_3$–Ni composites with a high and frequency-independent dielectric constant ($\varepsilon_r \approx 80\ 000$)," *Adv. Mater.*, vol. 13, no. 20, pp.

1541–1544, 2001, doi: 10.1002/1521-4095(200110)13:20<1541::AID-ADMA1541>3.0.CO;2-X.

[106] V. Bobnar, M. Hrovat, J. Holc, and M. Kosec, "Giant dielectric response in $Pb(Zr,Ti)O_3$–$Pb_2Ru_2O_{6.5}$ all-ceramic percolative composite," *Appl. Phys. Lett.*, vol. 92, no. 18, Art. no. 182911, May 2008, doi: 10.1063/1.2924287.

[107] V. Bobnar, M. Hrovat, J. Holc, and M. Kosec, "All-ceramic lead-free percolative composite with a colossal dielectric response," *J. Eur. Ceram. Soc.*, vol. 29, no. 4, pp. 725–729, Mar. 2009, doi: 10.1016/j.jeurceramsoc.2008.07.023.

[108] Q. M. Zhang, V. Bharti, and X. Zhao, "Giant electrostriction and relaxor ferroelectric behavior in electron-irradiated poly(vinylidene fluoride-trifluoroethylene) copolymer," *Science*, vol. 280, no. 5372, pp. 2101–2104, Jun. 1998, doi: 10.1126/science.280.5372.2101.

[109] H. Xu, Z.-Y. Cheng, D. Olson, T. Mai, Q. M. Zhang, and G. Kavarnos, "Ferroelectric and electromechanical properties of poly(vinylidene-fluoride–trifluoroethylene–chlorotrifluoroethylene) terpolymer," *Appl. Phys. Lett.*, vol. 78, no. 16, pp. 2360–2362, Apr. 2001, doi: 10.1063/1.1358847.

[110] C. Huang and Q. Zhang, "Enhanced dielectric and electromechanical responses in high dielectric constant all-polymer percolative composites," *Adv. Funct. Mater.*, vol. 14, no. 5, pp. 501–506, 2004, doi: 10.1002/adfm.200305021.

[111] V. Bobnar, A. Levstik, C. Huang, and Q. M. Zhang, "Enhanced dielectric response in all-organic polyaniline–poly(vinylidene fluoride-trifluoroethylene-chlorotrifluoroethylene) composite," *J. Non-Cryst. Solids*, vol. 353, no. 2, pp. 205–209, Feb. 2007, doi: 10.1016/j.jnoncrysol.2006.10.003.

[112] D. Klemm *et al.*, "Nanocelluloses: A new family of nature-based materials," *Angew. Chem. Int. Ed.*, vol. 50, no. 24, pp. 5438–5466, 2011, doi: 10.1002/anie.201001273.

[113] T. Nishino, K. Takano, and K. Nakamae, "Elastic modulus of the crystalline regions of cellulose polymorphs," *J. Polym. Sci. Part B Polym. Phys.*, vol. 33, no. 11, pp. 1647–1651, 1995, doi: 10.1002/polb.1995.090331110.

[114] T. Nishino, I. Matsuda, and K. Hirao, "All-cellulose composite," *Macromolecules*, vol. 37, no. 20, pp. 7683–7687, Oct. 2004, doi: 10.1021/ma049300h.

[115] S. Iwamoto, W. Kai, A. Isogai, and T. Iwata, "Elastic modulus of single cellulose microfibrils from tunicate measured by atomic force microscopy," *Biomacromolecules*, vol. 10, no. 9, pp. 2571–2576, Sep. 2009, doi: 10.1021/bm900520n.

[116] H. Fukuzumi, T. Saito, T. Iwata, Y. Kumamoto, and A. Isogai, "Transparent and high gas barrier films of cellulose nanofibers prepared by TEMPO-mediated oxidation," *Biomacromolecules*, vol. 10, no. 1, pp. 162–165, Jan. 2009, doi: 10.1021/bm801065u.

[117] A. Isogai, T. Saito, and H. Fukuzumi, "TEMPO-oxidized cellulose nanofibers," *Nanoscale*, vol. 3, no. 1, pp. 71–85, Jan. 2011, doi: 10.1039/C0NR00583E.

[118] L. Valentini, M. Cardinali, E. Fortunati, and J. M. Kenny, "Nonvolatile memory behavior of nanocrystalline cellulose/graphene oxide composite films," *Appl. Phys. Lett.*, vol. 105, no. 15, Art. no. 153111, Oct. 2014, doi: 10.1063/1.4898601.

[119] Y. B. Pottathara, V. Bobnar, M. Finšgar, Y. Grohens, S. Thomas, and V. Kokol, "Cellulose nanofibrils-reduced graphene oxide xerogels and cryogels for dielectric and electrochemical storage applications," *Polymer*, vol. 147, pp. 260–270, Jul. 2018, doi: 10.1016/j.polymer.2018.06.005.

[120] Q. Chen, Y. Wang, X. Zhou, Q. M. Zhang, and S. Zhang, "High field tunneling as a limiting factor of maximum energy density in dielectric energy storage capacitors," *Appl. Phys. Lett.*, vol. 92, no. 14, Art. no. 142909, Apr. 2008, doi: 10.1063/1.2903115.

[121] L. A. Dissado and J. C. Fothergill, *Electrical Degradation and Breakdown in Polymers*. London, U.K.: Institution of Engineering and Technology, 1992.

[122] W. F. Yong and T.-S. Chung, "Mechanically strong and flexible hydrolyzed polymers of intrinsic microporosity (PIM-1) membranes," *J. Polym. Sci. Part B Polym. Phys.*, vol. 55, no. 4, pp. 344–354, 2017, doi: 10.1002/polb.24279.

[123] R. P. White and J. E. G. Lipson, "Polymer free volume and its connection to the glass transition," *Macromolecules*, vol. 49, no. 11, pp. 3987–4007, Jun. 2016, doi: 10.1021/acs.macromol.6b00215.

[124] X. Tan, S. E. Young, Y. H. Seo, J. Y. Zhang, W. Hong, and K. G. Webber, "Transformation toughening in an antiferroelectric ceramic," *Acta Mater.*, vol. 62, pp. 114–121, Jan. 2014, doi: 10.1016/j.actamat.2013.09.038.

[125] M. Alhabeb *et al.*, "Guidelines for synthesis and processing of two-dimensional titanium carbide ($Ti_3C_2T_x$ MXene)," *Chem. Mater.*, vol. 29, no. 18, pp. 7633–7644, Sep. 2017, doi: 10.1021/acs.chemmater.7b02847.

[126] V. Jurečič, S. Lakshmanan, N. Novak, V. Kokol, and V. Bobnar, "Percolative dielectric behavior of titanium carbide MXene/cellulose nanofibrils composite films," *APL Mater.*, vol. 12, no. 11, Art. no. 111102, Nov. 2024, doi: 10.1063/5.0232250.

[127] V. Jurečič, N. Novak, L. Fulanović, and V. Bobnar, "Space charge contributions to the dielectric response and breakdown strength of high-temperature poly(ether imide)/polyimide blends," *Macromolecules*, vol. 56, no. 3, pp. 1097–1104, Feb. 2023, doi: 10.1021/acs.macromol.2c02220.

[128] X. Chen *et al.*, "Two-dimensional Ti_3C_2 MXene-based nanostructures for emerging optoelectronic applications," *Mater. Horiz.*, vol. 8, no. 11, pp. 2929–2963, Nov. 2021, doi: 10.1039/D1MH00986A.

[129] K. Kulasinski, "Free energy landscape of cellulose as a driving factor in the mobility of adsorbed water," *Langmuir*, vol. 33, no. 22, pp. 5362–5370, Jun. 2017, doi: 10.1021/acs.langmuir.7b00914.

[130] D.-L. Li *et al.*, "Enhanced dielectric properties of all-cellulose composite film via modulating hydroxymethyl conformation and hydrogen bonding network," *ACS Macro Lett.*, vol. 12, no. 7, pp. 880–887, Jul. 2023, doi: 10.1021/acsmacrolett.3c00224.

[131] H. Montès, K. Mazeau, and J. Y. Cavaillé, "The mechanical β relaxation in amorphous cellulose," *J. Non-Cryst. Solids*, vol. 235–237, pp. 416–421, Aug. 1998, doi: 10.1016/S0022-3093(98)00600-0.

[132] A. Jonas and R. Legras, "Relation between PEEK semicrystalline morphology and its subglass relaxations and glass transition," *Macromolecules*, vol. 26, no. 4, pp. 813–824, Feb. 1993, doi: 10.1021/ma00056a036.

[133] J. P. Habas, J. Peyrelasse, and M. F. Grenier-Loustalot, "Rheological study of a high-performance polyimide. interpretation of the secondary mechanical relaxations of a nadimide crosslinked system," *High Perform. Polym.*, vol. 8, no. 4, pp. 515–532, Dec. 1996, doi: 10.1088/0954-0083/8/4/004.

[134] Y. Zhang, S. Ke, H. Huang, L. Zhao, L. Yu, and H. L. W. Chan, "Dielectric relaxation in polyimide nanofoamed films with low dielectric constant," *Appl. Phys. Lett.*, vol. 92, no. 5, Art. no. 052910, Feb. 2008, doi: 10.1063/1.2840715.

[135] P. Lunkenheimer, V. Bobnar, A. V. Pronin, A. I. Ritus, A. A. Volkov, and A. Loidl, "Origin of apparent colossal dielectric constants," *Phys. Rev. B*, vol. 66, no. 5, Art. no. 052105, Aug. 2002, doi: 10.1103/PhysRevB.66.052105.

[136] S. Rajala *et al.*, "Cellulose nanofibril film as a piezoelectric sensor material," *ACS Appl. Mater. Interfaces*, vol. 8, no. 24, pp. 15607–15614, Jun. 2016, doi: 10.1021/acsami.6b03597.

[137] A. Eršte, "Investigations and separation of various contributions to dielectric response of advanced ceramic and polymeric materials," Ph.D. dissertation, Jožef Stefan International Postgraduate School, Ljubljana, Slovenia, 2012.

[138] G.-H. Kim *et al.*, "High thermal conductivity in amorphous polymer blends by engineered interchain interactions," *Nat. Mater.*, vol. 14, no. 3, Art. no. 3, Mar. 2015, doi: 10.1038/nmat4141.

[139] J. Xu *et al.*, "Highly stretchable polymer semiconductor films through the nanoconfinement effect," *Science*, vol. 355, no. 6320, pp. 59–64, Jan. 2017, doi: 10.1126/science.aah4496.

[140] A. Shanker, C. Li, G.-H. Kim, D. Gidley, K. P. Pipe, and J. Kim, "High thermal conductivity in electrostatically engineered amorphous polymers," *Sci. Adv.*, vol. 3, no. 7, Art. no. e1700342, Jul. 2017, doi: 10.1126/sciadv.1700342.

[141] A. Gumyusenge *et al.*, "Semiconducting polymer blends that exhibit stable charge transport at high temperatures," *Science*, vol. 362, no. 6419, pp. 1131–1134, Dec. 2018, doi: 10.1126/science.aau0759.

[142] W. A. Schulze and K. Ogino, "Review of literature on aging of dielectrics," *Ferroelectrics*, vol. 87, no. 1, pp. 361–377, Nov. 1988, doi: 10.1080/00150198808201399.

[143] Y. A. Genenko and D. C. Lupascu, "Drift of charged defects in local fields as aging mechanism in ferroelectrics," *Phys. Rev. B*, vol. 75, no. 18, Art. no. 184107, May 2007, doi: 10.1103/PhysRevB.75.184107.

[144] J. Melcher, Y. Deben, and G. Arlt, "Dielectric effects of moisture in polyimide," *IEEE Trans. Electr. Insul.*, vol. 24, no. 1, pp. 31–38, Feb. 1989, doi: 10.1109/14.19863.

[145] R. Subramanian, M. T. Potriger, J. H. Morris, and J. P. Curilla, "Effect of moisture on the physical properties of polyimide films," *MRS Online Proc. Libr.*, vol. 227, no. 1, pp. 147–154, Dec. 1991, doi: 10.1557/PROC-227-147.

[146] B. X. Du, Z. Y. He, Q. Du, and Y. G. Guo, "Effects of water absorption on surface charge and dielectric breakdown of polyimide/Al_2O_3 nanocomposite films," *IEEE Trans. Dielectr. Electr. Insul.*, vol. 23, no. 1, pp. 134–141, Feb. 2016, doi: 10.1109/TDEI.2015.005203.

[147] H. W. Starkweather, "Aspects of simple, non-cooperative relaxations," *Polymer*, vol. 32, no. 13, pp. 2443–2448, Jan. 1991, doi: 10.1016/0032-3861(91)90087-Y.

[148] P. Musto, M. Abbate, M. Lavorgna, G. Ragosta, and G. Scarinzi, "Microstructural features, diffusion and molecular relaxations in polyimide/silica hybrids," *Polymer*, vol. 47, no. 17, pp. 6172–6186, Aug. 2006, doi: 10.1016/j.polymer.2006.05.074.

[149] S. Diaham, S. Zelmat, M.-L. Locatelli, S. Dinculescu, M. Decup, and T. Lebey, "Dielectric breakdown of polyimide films: Area, thickness and temperature dependence," *IEEE Trans. Dielectr. Electr. Insul.*, vol. 17, no. 1, pp. 18–27, Feb. 2010, doi: 10.1109/TDEI.2010.5411997.

[150] D. Min *et al.*, "Thickness-dependent DC electrical breakdown of polyimide modulated by charge transport and molecular displacement," *Polymers*, vol. 10, no. 9, Art. no. 9, Sep. 2018, doi: 10.3390/polym10091012.

[151] Y. Liu *et al.*, "Tunable electric properties of $PbZrO_3$ films related to the coexistence of ferroelectricity and antiferroelectricity at room temperature," *Appl. Phys. Lett.*, vol. 100, no. 21, Art. no. 212902, May 2012, doi: 10.1063/1.4720146.

[152] B. Peng, H. Fan, and Q. Zhang, "High tunability in (111)-oriented relaxor $Pb_{0.8}Ba_{0.2}ZrO_3$ thin film with antiferroelectric and ferroelectric two-phase coexistence," *J. Am. Ceram. Soc.*, vol. 96, no. 6, pp. 1852–1856, 2013, doi: 10.1111/jace.12269.

[153] J. Wang, T. Yang, K. Wei, G. Li, and S. Chen, "Bi-tunable dielectric constant of antiferroelectric PZT ceramics under DC electric field," *J. Am. Ceram. Soc.*, vol. 95, no. 5, pp. 1483–1485, 2012, doi: 10.1111/j.1551-2916.2012.05129.x.

[154] T. Sa, N. Qin, G. Yang, and D. Bao, "W-doping induced antiferroelectric to ferroelectric phase transition in $PbZrO_3$ thin films prepared by chemical solution deposition," *Appl. Phys. Lett.*, vol. 102, no. 17, Art. no. 172906, May 2013, doi: 10.1063/1.4803941.

[155] L. Li, M. Spreitzer, and D. Suvorov, "Unique dielectric tunability of $Ag(Nb_{1-x}Ta_x)O_3$ ($x = 0$–0.5) ceramics with ferrielectric polar order," *Appl. Phys. Lett.*, vol. 104, no. 18, Art. no. 182902, May 2014, doi: 10.1063/1.4875581.

[156] H. Pan *et al.*, "Defect-induced, ferroelectric-like switching and adjustable dielectric tunability in antiferroelectrics," *Adv. Mater.*, vol. 35, no. 24, Art. no. 2300257, 2023, doi: 10.1002/adma.202300257.

[157] V. Jurečič, L. Fulanović, J. Koruza, V. Bobnar, and N. Novak, "Synergetic boost of functional properties near critical end points in antiferroelectric systems," *Phys. Rev. Mater.*, vol. 7, no. 11, Art. no. 114407, Nov. 2023, doi: 10.1103/PhysRevMaterials.7.114407.

[158] H. Liu *et al.*, "An intriguing intermediate state as a bridge between antiferroelectric and ferroelectric perovskites," *Mater. Horiz.*, vol. 7, no. 7, pp. 1912–1918, Jul. 2020, doi: 10.1039/D0MH00253D.

[159] P. Tolédano and M. Guennou, "Theory of antiferroelectric phase transitions," *Phys. Rev. B*, vol. 94, no. 1, Art. no. 014107, Jul. 2016, doi: 10.1103/PhysRevB.94.014107.

[160] Z. Fu *et al.*, "Unveiling the ferrielectric nature of $PbZrO_3$-based antiferroelectric materials," *Nat. Commun.*, vol. 11, no. 1, Art. no. 1, Jul. 2020, doi: 10.1038/s41467-020-17664-w.

[161] S. Miga and J. Dec, "Non-linear dielectric response of ferroelectric and relaxor materials," *Ferroelectrics*, vol. 367, no. 1, pp. 223–228, Oct. 2008, doi: 10.1080/00150190802377553.

[162] S. E. Young, H. Z. Guo, C. Ma, M. R. Kessler, and X. Tan, "Thermal analysis of phase transitions in perovskite electroceramics," *J. Therm. Anal. Calorim.*, vol. 115, no. 1, pp. 587–593, Jan. 2014, doi: 10.1007/s10973-013-3363-1.

[163] H. Fu and R. E. Cohen, "Polarization rotation mechanism for ultrahigh electromechanical response in single-crystal piezoelectrics," *Nature*, vol. 403, no. 6767, Art. no. 6767, Jan. 2000, doi: 10.1038/35002022.

[164] A. A. Heitmann and G. A. Rossetti Jr., "Thermodynamics of ferroelectric solid solutions with morphotropic phase boundaries," *J. Am. Ceram. Soc.*, vol. 97, no. 6, pp. 1661–1685, 2014, doi: 10.1111/jace.12979.

[165] S. Kwon, W. Hackenberger, E. Alberta, E. Furman, and M. Lanagan, "Nonlinear dielectric ceramics and their applications to capacitors and tunable dielectrics," *IEEE Electr. Insul. Mag.*, vol. 27, no. 2, pp. 43–55, Mar. 2011, doi: 10.1109/MEI.2011.5739422.

[166] B. Lewis, "Energy loss processes in ferroelectric ceramics," *Proc. Phys. Soc.*, vol. 73, no. 1, pp. 17–24, Jan. 1959, doi: 10.1088/0370-1328/73/1/304.

[167] A. Bradeško, A. Hedl, L. Fulanović, N. Novak, and T. Rojac, "Self-heating of relaxor and ferroelectric ceramics during electrocaloric field cycling," *APL Mater.*, vol. 7, no. 7, Art. no. 071111, Jul. 2019, doi: 10.1063/1.5109028.

[168] C. M. Fancher *et al.*, "The contribution of 180° domain wall motion to dielectric properties quantified from in situ X-ray diffraction," *Acta Mater.*, vol. 126, pp. 36–43, Mar. 2017, doi: 10.1016/j.actamat.2016.12.037.

[169] F. Xu, S. Trolier-McKinstry, W. Ren, B. Xu, Z.-L. Xie, and K. J. Hemker, "Domain wall motion and its contribution to the dielectric and piezoelectric properties of lead zirconate titanate films," *J. Appl. Phys.*, vol. 89, no. 2, pp. 1336–1348, Jan. 2001, doi: 10.1063/1.1325005.

[170] D. I. Woodward, J. Knudsen, and I. M. Reaney, "Review of crystal and domain structures in the $PbZr_xTi_{1-x}O_3$ solid solution," *Phys. Rev. B*, vol. 72, no. 10, Art. no. 104110, Sep. 2005, doi: 10.1103/PhysRevB.72.104110.

[171] J. Gao *et al.*, "Microstructure basis for strong piezoelectricity in Pb-free $Ba(Zr_{0.2}Ti_{0.8})O_3$-$(Ba_{0.7}Ca_{0.3})TiO_3$ ceramics," *Appl. Phys. Lett.*, vol. 99, no. 9, Art. no. 092901, Aug. 2011, doi: 10.1063/1.3629784.

[172] L. M. Riemer, L. Jin, H. Uršič, M. Otonicar, T. Rojac, and D. Damjanovic, "Dielectric and electro-mechanic nonlinearities in perovskite oxide ferroelectrics, relaxors, and relaxor ferroelectrics," *J. Appl. Phys.*, vol. 129, no. 5, Art. no. 054101, Feb. 2021, doi: 10.1063/5.0035859.

[173] D. V. Taylor and D. Damjanovic, "Evidence of domain wall contribution to the dielectric permittivity in PZT thin films at sub-switching fields," *J. Appl. Phys.*, vol. 82, no. 4, pp. 1973–1975, Aug. 1997, doi: 10.1063/1.366006.

[174] S. S. N. Bharadwaja, A. Laha, S. Halder, and S. B. Krupanidhi, "Reversible and irreversible switching processes in pure and lanthanum modified lead zirconate thin films," *Mater. Sci. Eng. B*, vol. 94, no. 2, pp. 218–222, Jun. 2002, doi: 10.1016/S0921-5107(02)00091-0.

[175] Z. Luo *et al.*, "Rayleigh-like nonlinear dielectric response and its evolution during electrical fatigue in antiferroelectric (Pb,La)(Zr,Ti)O_3 thin film," *Appl. Phys. Lett.*, vol. 104, no. 14, Art. no. 142904, Apr. 2014, doi: 10.1063/1.4870992.

[176] D. Damjanovic and M. Demartin, "Contribution of the irreversible displacement of domain walls to the piezoelectric effect in barium titanate and lead zirconate titanate ceramics," *J. Phys. Condens. Matter*, vol. 9, no. 23, Art. no. 4943, Jun. 1997, doi: 10.1088/0953-8984/9/23/018.

[177] V. V. Shvartsman, A. L. Kholkin, A. Orlova, D. Kiselev, A. A. Bogomolov, and A. Sternberg, "Polar nanodomains and local ferroelectric phenomena in relaxor lead lanthanum zirconate titanate ceramics," *Appl. Phys. Lett.*, vol. 86, no. 20, Art. no. 202907, May 2005, doi: 10.1063/1.1923756.

[178] H. Ursic, S. Drnovsek, and B. Malic, "Complex domain structure in polycrystalline $Pb(Sc_{0.5}Nb_{0.5})O_3$," *J. Phys. Appl. Phys.*, vol. 49, no. 11, Art. no. 115304, Feb. 2016, doi: 10.1088/0022-3727/49/11/115304.

Bibliography

Publications Related to the Thesis

Journal Articles

V. Jurečič, T. Rojac, V. Bobnar, and N. Novak, "Origin of enhanced dielectric tunability in antiferroelectric ceramic systems," *Adv. Funct. Mater.*, vol. 35, no. 2, Art. no. 2412739, 2025, doi: 10.1002/adfm.202412739.

V. Jurečič, S. Lakshmanan, N. Novak, V. Kokol, and V. Bobnar, "Percolative dielectric behavior of titanium carbide MXene/cellulose nanofibrils composite films," *APL Mater.*, vol. 12, no. 11, Art. no. 111102, 2024, doi: 10.1063/5.0232250.

V. Jurečič, L. Fulanović, J. Koruza, V. Bobnar, and N. Novak, "Synergetic boost of functional properties near critical end points in antiferroelectric systems," *Phys. Rev. Mater.*, vol. 7, no. 11, Art. no. 114407, 2023, doi: 10.1103/PhysRevMaterials.7.114407.

V. Jurečič, N. Novak, L. Fulanović, and V. Bobnar, space charge contributions to the dielectric response and breakdown strength of high-temperature poly(ether imide)/polyimide blends," *Macromolecules*, vol. 56, no. 3, pp. 1097–1104, 2023, doi: 10.1021/acs.macromol.2c02220.

Published Scientific Conference Contribution Abstract (Invited Lecture)

V. Jurečič, N. Novak, and V. Bobnar, "Designing polymer systems with enhanced dielectric response," in *Proceedings of the 8th International Symposium on Dielectric Materials and Applications (ISyDMA'8)*, Orlando, Florida, USA, May 12–16, 2024.

V. Bobnar, A. Matavž, V. Jurečič, Y. B. P. Thara, V. Kokol, S. Thomas, K. Geirhos, P. Lunkenheimer, Q. M. Zhang, *et al.*, "Designing novel inorganic and polymer systems with enhanced dielectric and electromechanical response," in *Book of Abstracts of the 7th International Symposium on Dielectric Materials and Applications*, Poznań (online), December 6–8, 2022.

Published Scientific Conference Contribution Abstract

V. Jurečič, L. Fulanović, J. Koruza, V. Bobnar, and N. Novak, "Synergetic boost of functional properties near critical end points in antiferroelectric systems," in *European Conference on Applications of Polar Dielectrics (ECAPD 2024)*, online, 2024.

N. Novak, V. Jurečič, H. U. Nemevšek, T. Rojac, and V. Bobnar, "Origin of the enhanced dielectric tunability in antiferroelectric PNZST ceramics," in *Electroceramics XIX Conference*, online, 2024.

V. Jurečič, T. Rojac, V. Bobnar, and N. Novak, "Izvor ojačitve dielektrične nastavljivosti v antiferoelektrični PNZST keramiki," in *Zbornik povzetkov 13. konference fizikov v osnovnih raziskavah*, Brdo pri Kranju, Slovenia, November 18, 2024.

V. Kokol, S. Lakshmanan, V. Jurečič, and V. Bobnar, "Dielectric and thermal conductive properties of $Ti_3C_2T_x$ MXene/nanocellulose based substrates for flexible organic electronics," in *Abstracts of NANOCON 2024: 16th International Conference on Nanomaterials – Research & Application*, Brno, Czech Republic, October 16–18, 2024.

V. Jurečič, N. Novak, L. Fulanović, X. Chen, Q. M. Zhang, and V. Bobnar, "Vpliv prostih nabojev na električno prebojno trdnost visokotemperaturnih polimernih zmesi," in *Zbornik povzetkov 12. konference fizikov v osnovnih raziskavah*, Terme Čatež, Slovenia, November 11, 2022.

V. Jurečič, N. Novak, X. Chen, Q. M. Zhang, and V. Bobnar, "Space charge contributions to the dielectric response and breakdown strength of high-temperature polyetherimide/polyimide blends," in *Book of Abstracts of the 14th Jožef Stefan International Postgraduate School Students' Conference*, Kamnik, Slovenia, June 1–3, 2022.

V. Jurečič, N. Novak, L. Fulanović, X. Chen, Q. M. Zhang, and V. Bobnar, "Space charge contributions to the dielectric response and breakdown strength of high-temperature polyetherimide/polyimide blends," in *Proceedings of the 57th International Conference on Microelectronics, Devices and Materials & The Workshop on Energy Harvesting: Materials and Applications*, Maribor, Slovenia, September 14–16, 2022.

Published Professional Conference Contribution Abstract

V. Jurečič, N. Novak, L. Fulanović, and V. Bobnar, "Space charge contributions to the dielectric response and breakdown strength of high-temperature polyetherimide/polyimide blends," in *Abstracts of the 8th International Conference on Women in Physics (ICWIP2023)*, online, July 10–14, 2023.

Other Publications

Journal Articles

S. Lakshmanan, V. Jurečič, V. Bobnar, and V. Kokol, "Dielectric and thermal conductive properties of differently structured $Ti_3C_2T_x$ MXene-integrated nanofibrillated cellulose films," *Cellulose*, vol. 31, no. 13, pp. 8149–8168, 2024, doi: 10.1007/s10570-024-06105-2.

Published Professional Conference Contribution Abstract

M. Remškar, V. Jurečič, U. Tkalec, B. Šetina, and M. Conradi, "Women in physics in Slovenia," in *Abstracts of the 8th International Conference on Women in Physics (ICWIP2023)*, online, July 10–14, 2023.

Biography

Vida Jurečič was born on 4th October 1995 in Trbovlje, Slovenia. After attending Primary School Leskovec pri Krškem and the Technical Gymnasium at the School Centre Krško-Sevnica, she enrolled at the Faculty of Education, University of Ljubljana, where she obtained her bachelor's degree in 2019 in the Two-Subject Teacher (Physics and Mathematics) program. She continued her studies by enrolling in a master's degree program in Teacher Education – Subject Teacher Education at the same faculty. In 2020, she received her master's degree after defending her thesis titled "*Didactic Instrument to Teach and Assess the Understanding of the Concept of Energy.*" In the same year, she became a PhD student in the Nanosciences and Nanotechnologies program at the Jožef Stefan International Postgraduate School in Ljubljana, Slovenia, and began working as a young researcher at the Condensed Matter Physics Department of the Jožef Stefan Institute. In 2024, she started working at the Faculty of Education, University of Ljubljana, as a teaching assistant in Physics Education.